

**STUDIES ON THE DEFORMATION MICROSTRUCTURE IN  
SOME COARSE-GRAIN HIGH-Mn STEELS USING X-RAY  
AND ELECTRON DIFFRACTION**

**THESIS SUBMITTED FOR THE DEGREE OF  
DOCTOR OF PHILOSOPHY (SCIENCE)  
OF  
JADAVPUR UNIVERSITY  
2023**

**By**

**Tousif Riaz**

Index No.: 122/18/Phys./26

Department of Physics

Jadavpur University

Kolkata-700 032

INDIA



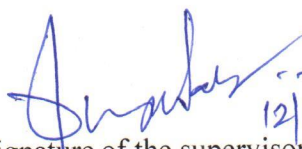
Dedicated  
to  
my parents





**CERTIFICATE FROM THE SUPERVISOR**

This is to certify that the thesis entitled "*Studies on the deformation microstructure in some coarse-grain high-Mn steels using x-ray and electron diffraction*" submitted by Tousif Riaz, who got his name registered on 29<sup>th</sup> March 2018 for the award of Ph.D. (Science) degree of Jadavpur University, is absolutely based upon his own work under the supervision of Prof. Puspendu Sahu and that neither this thesis nor any part of it has been submitted for any degree/diploma or any other academic award anywhere before.

  
Signature of the supervisor

and date with official seal



Dr. Puspendu Sahu  
Professor  
Department of Physics  
Jadavpur University  
Kolkata - 700 032



## ACKNOWLEDGEMENTS

I would like to take this opportunity to convey my sincere gratitude towards all those people who have extended their valuable assistance, encouragement and contribution indispensably to this PhD work in one way or the other.

First and foremost, I would like to thank my supervisor Prof. Puspendu Sahu for his kindness, constant enthusiasm and guidance. I am extremely grateful for his continuous streams of ideas, which opened many avenues for study and for his intensive proof reading of this thesis. I have been fortunate enough in unflinching support and encouragement from him.

I extend my thanks to my lab mates who have assisted me immensely during this tenure. From the core of my heart, I would like to specially thank Dr. Bhupeshwar Mahato (CSIR NML, Jamshedpur) for his contribution related to TEM investigation. I would like to thank of my Lab mate Dr. Soma Rani Das, Mr. Saikat Shyamal, Mr. Dhananjay Das and Ms. Debjani Niyogi for all contribution and support.

In my PhD tenure, I got the opportunity to work in collaboration with Dr. Swapan Kumar Shee (Midnapore College), Prof. Pravash Chandra Chakraborti (Jadavpur University), Prof. Jukka Komi (University of Oulu), Prof. L. Pentti Karjalainen (University of Oulu), Prof. David Porter (University of Oulu) Matias Jaskari (University of Oulu). I want to express my deep gratitude to all of them.

I extend special acknowledgement to all the office staff for their help in regards to all officials activities related directly or indirectly to my research work during these years.

I don't have any idea how to acknowledge my family. I must say that I would not have been able to come to this stage without their constant encouragement, support, love and prayers. Words cannot express how grateful I am to my parents for all of the sacrifices that they have made on my behalf.

I would like to thank my special friend Dr. Hasina Khatun for her immense and continuous support.



To conclude this, I would like to acknowledge the “DST INSPIRE Fellowship, Government of India” for providing me the financial support. So, again thanks to all.

Date: 12/12/23

*Tousif Riaz*  
Tousif Riaz



## PREFACE

The present dissertation reports the deformation microstructure in some coarse-grain high-Mn steels using X-ray and electron diffraction. The thesis is divided into two parts i.e., Part A and Part B. Part A contains two Chapters and four Chapters are in Part B. Chapter 1 briefly describes strain hardening in metals/alloys, stages of strain hardening, the fundamentals of plastic deformation and short literature review on the grain size strengthening in high-Mn steel. Chapter 2 concerns the description of underlying X-ray and electron diffraction theories used towards assessment of deformation microstructure. Chapters 3, 4, and 5 contain the findings of the present investigation, where three different studies of some coarse-grain high-Mn steels are described and finally, Chapter 6 gives the conclusion of the study.

The entire study involved with the investigations of mechanical properties in terms of different deformation microstructures in different high-Mn steels with & without Al alloying and the chemical composition of the working alloys are Fe-25Mn-2Al-0.1C, Fe-25Mn-xAl-0.1C-0.4Si (where  $x=0, 1, 3$ ), Fe-30Mn-3Si-3Al. Unless otherwise stated, the compositions mentioned throughout this dissertation are in weight percentage. All of the steels were made by melting them in induction furnaces and then through the proper thermomechanical processes to generate grains that were in the range of  $\sim(30-50)$   $\mu\text{m}$  in size. Uniaxial tensile tests and in some cases axisymmetrical compression tests with quasi-static strain rate: ( $10^{-3}$ - $10^{-4}$   $\text{s}^{-1}$ ) were performed at room temperature (RT), and the tests were interrupted at different true strains as per requirement, and somewhere they were continued till fracture. X-ray diffraction (XRD), transmission electron microscope (TEM) and electron backscattered diffraction (EBSD) were used to investigate the deformed microstructures of the steels. The obtained deformation microstructure was interpreted in terms of quantitative estimates for various microstructural parameters, including dislocation density, stacking fault probability, stacking fault energy, etc., as determined from X-ray line profile analysis and the findings were also substantiated with TEM observations. An effort has been made to interpret deformation mechanism(s) and to correlate with the strain hardening behavior of the steel.



# CONTENTS

## Part A

### General Introduction & Methodologies

#### Chapter 1: General Introduction

1.1	Background of the work	5
1.2	Mechanical response and strain hardening in metals/alloys and the associated stages	8
1.2.1	Tensile and compressive response	9
1.2.2	The Hall-Petch theory	10
1.2.3	The stages of strain hardening	12
1.3	The factors influencing the deformation behaviour of high-Mn steels	14
1.3.1	SFE of austenite	14
1.3.2	Grain size of austenite	16
1.3.3	Grain orientation of austenite	18
1.3.4	Deformation temperature	22
1.3.5	Alloying elements	24
1.4	Critical twinning stress of high-Mn steel	26
1.5	A review on the grain size strengthening in high-Mn steels	28
1.6	Aims and scopes of the dissertation	31

#### References

#### Chapter 2: Methodologies adopted for microstructure characterization

2.1	Determination of extended defects and the underlying principles	45
2.2	X-ray diffraction	45

2.2.1	Fourier analysis: determination of coherent domain sizes and r.m.s. strains	48
2.2.2	Conventional Warren-Averbach analysis	48
2.2.3	Modified Williamson-Hall and Warren-Averbach analyses	50
2.2.4	Consideration of planar faults	52
2.3	Transmission electron microscopy	54
2.3.1	Contrast formation in transmission electron microscope	54
2.3.2	Weak Beam Transmission Electron Microscopy	57
2.4	Electron Backscatter Diffraction	59
2.5	Estimation of experimental stacking fault energy	62
2.5.1	X-ray diffraction approach	62
2.5.2	Transmission electron microscopy approach	64

References

## **Part B**

### **Case study of some coarse-grain high-Mn steels**

#### **Chapter 3: Dislocation substructure study of Fe-25Mn-2Al-0.1C Steel**

3.1	Material processing & flow stress behavior	73
3.1.1	Material and experimental	73
3.1.2	Flow stress and strain hardening behavior	73
3.2	TEM investigations of deformation microstructure & their influence on the strain hardening behaviour	74
3.2.1	TEM investigation at different stage of deformation	74
3.2.2	Interpretation of strain hardening behavior	77

References

## **Chapter 4: Deformation behavior study of Fe-25Mn-0.1C-0.4Si-xAl (x=0,1,3) Steel**

4.1	Material, its processing and the flow stress behavior	81
4.1.1	Material and experimental	81
4.1.2	Flow stress behavior	82
4.2	Microstructural investigation using X-ray line profile analysis (XLPA)	83
4.2.1	Normalized intensity profiles and anisotropic strain broadening	84
4.2.2	Effect of strain anisotropy on Williamson-Hall plots	85
4.2.3	Conventional and modified Warren-Averbach analysis	87
4.3	Effect of Al on different microstructural parameters	88
4.3.1	Evolution of dislocation parameters with Al content	88
4.3.2	Effect of Al concentration on planar fault densities	91
4.3.3	Effect of Al concentration on SFE	92
4.4	TEM investigations & its implications on the deformation mechanism	94
4.4.1	TEM investigations of the deformation microstructure	94
4.4.2	The effect of $\gamma \rightarrow \epsilon$ transformation on strain hardening	96
4.5	Critical shear stress for twinning & prediction of deformation map	98
4.5.1	SFE-dependent critical shear stress of twinning and stacking fault width	98
4.5.2	The critical shear stress for twinning-based deformation regime	100

References

## **Chapter 5: Deformation microstructure study of Fe-30Mn-3Si-3Al Steel under tensile and compressive loading**

5.1	Material processing & the flow stress behavior	107
5.1.1	Material and experimental	107
5.1.2	Tensile and compressive behavior	108

5.2	X-ray diffraction studies of the deformation microstructure	110
5.2.1	Influence of strain anisotropy on the Williamson-Hall plots	110
5.2.2	Conventional and modified Warren-Averbach analysis	113
5.2.3	Evolution of dislocation density and its characteristics during tension and compression	114
5.2.4	Evolution of fault density during tension and compression	118
5.2.5	Stacking fault energy analysis	119
5.3	TEM & EBSD investigations on deformation microstructures	120

References

## **Chapter 6: Summary and Conclusions**

6.1	General conclusion	127
6.2	Scope for future work	129



## **List of Publications**

### **Journal Publications**

- 1 Dislocation substructures in tensile deformed Fe-Mn-Al-C steel.

**T. Riaz**, S.R. Das, T. Sahu, P.C. Chakraborti and P. Sahu\*, *Materials Letters*, 282 (2021) 128691.

- 2 X-ray line profile analysis on the deformation microstructure of Al-bearing high-Mn steels.

**T. Riaz**, S. Shyamal, S.K. Shee, L.P. Karjalainen and P. Sahu\*, *Materials Characterization*, 196 (2023) 112567.

- 3 Influence of Al Variation on the Mechanical Properties and Critical Shear Stress of Twinning in Fe-Mn-Al-C Steels.

**T. Riaz**, S.R. Das and P. Sahu\*, *Journal of Material Engineering and Performance* 16 (2022) 1636-1644.

- 4 A quantitative assessment on the contribution of various dislocation substructures to flow stress in a fine-grain high-Mn steel.

S.R. Das, **T. Riaz**, S. Shyamal, P.C. Chakraborti and P. Sahu\*, *Materials Letters*, 300 (2021) 130216.

### **List of Communicated Paper:**

- 1 X-ray line profile analysis of the deformation microstructure in a Fe-Mn-Si-Al steel under tensile and compressive loading. (communicated)

**T. Riaz**, P. Sahu\*.

- 2 Tension/compression asymmetry in a Fe-Mn-Si-Al steel. (communicated)

**T. Riaz**, P. Sahu\*.

## **List of Presentation/Participation in conferences**

- 1 Oral presentation of a paper entitled “Dislocation substructures of tensile deformed Fe-25Mn-2Al-0.1C steel” in “**International Conference of Multidisciplinary Aspects of Materials in Engineering (IC-MAME 2021)**” October 8-9, 2021, Panjab University, Chandigarh, India.
2. Oral presentation of a paper entitled “Influence of critical shear stress of twinning on the deformation behavior of twinning induced plasticity steels” in “**International Conference on Future Trends in Materials and Mechanical Engineering (IC-FTMME 2022)**” August 19-20, 2022, SRM IST, Delhi-NCR campus, Ghaziabad, India.

## List of symbols\*

$\alpha''$	Angle between the perfect dislocation line and its Burgers vector
$n$	Any integer
$D$	Apparent crystallite size
$\sigma_A$	Applied tensile stress
$\gamma_{fcc}$	Austenite (fcc)
$\bar{C}_{hkl}$	Average contrast factor for (hkl) planes
$L_0$	Average length of the twinning source
$\rho_{loop}$	Average prismatic loop density
$\theta_{hkl}$	Bragg angle
$\vec{b}_p$	Burgers vector of partial dislocations (Shockley/Frank)
$\beta'$	Character angle between the diffraction vector and dislocation line
$E_{str}$	Coherency strain energy
$\rho(D)$	Column length (size) distribution function
$\tau_{crss}$	Critical resolved shear stress
$(\tau_c)_{twin}$	Critical twinning stress
$\Delta K$	Deviation from diffraction vector
$s$	Deviation from exact Bragg angle condition in TEM
$\Delta L$	Deviation from L
$\vec{g}$	Diffraction vector
$K$	Diffraction vector for X-ray analysis
$E_{dil}$	Dilatation energy due to volumetric stress
$r$	Dislocation core radius
$\rho$	Dislocation density
$\alpha_i$	Dislocation interaction strength parameter
$R_e$	Effective outer cut-off radius of dislocations
$\gamma_{eff}$	Effective stacking fault energy
$B$	Electron beam direction

$\varepsilon_{hcp}$	Epsilon martensite (hcp)
$x_{eq}$	Equilibrium separation distance of the partial dislocation pairs
$w_{tw}$	Equilibrium twin width
$\sigma$	Flow stress
$L$	Fourier variable
$f_{\gamma(edge)}$	Fraction of edge dislocation
$f_{\gamma(screw)}$	Fraction of screw dislocation
$d$	Grain size
$\gamma_{\infty}$	Ideal stacking fault energy
$d_{hkl}$	Interplanar spacing for $(hkl)$ planes
$\gamma_{isf}$	Intrinsic stacking fault energy
$\vec{R}$	Lattice distortion vector
$\sigma_{YS}^0$	Lattice friction stress
$a$	Lattice parameter
$\beta$	Line breadth
$\vec{u}$	Line direction of dislocations
$\langle \varepsilon_L^2 \rangle$	Mean square microstrain
$\varepsilon_L$	Mean squared strain
$A^d(L, K_i)$	Order dependent Fourier strain coefficient
$A^s(L)$	Order independent Fourier size coefficients
$\vec{b}$	Perfect dislocations' Burgers vector
$\nu$	Poisson's ratio
$w$	Prismatic loop diameter
$K_s$	Scherrer constant
$q$	Screw or edge character of dislocation
$E_{sh}$	Shear energy
$m_T$	Shear for partial dislocation
$m_G$	Shear for perfect dislocation
$G$	Shear modulus
$\tau$	Shear stress
$\beta_s$	Size broadening integral breadth

$\gamma$	Stacking fault energy
$P_{sf}$	Stacking fault probability
$w_{sf}$	Stacking fault width
$\beta_D$	Strain broadening integral breadth
$\rho(\varepsilon_L)$	Strain distribution function
$\sigma_{forest}$	Stress due to forest dislocations
$\sigma_{loop}$	Stress due to prismatic dislocation loop
$T$	Taylor factor
$P_{tw}$	Twin fault probability
$e$	Vector normal to the dislocation line
$\lambda$	Wavelength of X-rays
$\sigma_{YS}$	Yield stress
$w_{ov}$	Equilibrium width of overlapping stacking faults

\* Symbols appearing in several equations/figures obtained from literatures are not described here. This list primarily describes the symbols considered in the present work.





## Abbreviations

BSE	Backscatter electron
BF	Bright field
CCD	Charge-coupled device
CST	Cross-slip truncation
DF	Dark filed
DRV	Dynamic recovery
DSA	Dynamic strain ageing
EBSD	Electron backscatter diffraction
ECCI	Electron channelling contrast imaging
ECAP	Equal channel angular pressing
ESF	Extrinsic stacking fault
fcc	Face-centered cubic
FESEM	Field emission scanning electron microscope
FWHM	Full width half maximum
HRTEM	High resolution transmission electron microscopy
High-Mn	High-Manganese
ICDD	International centre for diffraction data
ISF	Intrinsic stacking fault
IPF	Inverse pole figure
KAM	Kernel average misorientation
LEDs	Low-energy dislocation structures
MBIP	Microband induced plasticity
RT	Room temperature
SEM	Scanning electron microscope
SAD	Selected area diffraction
SPD	Shockley partial dislocation
SRC	Short-range clustering
SRO	Short-range order
SF	Stacking fault
SFE	Stacking fault energy

SHR	Strain hardening rate
TRIP	Transformation induced plasticity
TEM	Transmission electron microscope
TWIP	Twinning induced plasticity
UTS	Ultimate tensile strength
UFG	Ultrafine grained
WA	Warren-Averbach
WB	Weak beam
WBDF	Weak beam dark field
XRD	X-ray diffraction
YS	Yield strength

# *Part A*

## *General Introduction & Methodologies*



# *Chapter 1*

## *General introduction*





## 1.1 Background of the work

For several decades, it has been a challenging matter for material scientists to process and develop metals and alloys with superior mechanical properties, i.e., a combination of high strength, ductility, and toughness. However, research in this field has been fruitful, and scientists have developed sophisticated high-strength steels for automotive applications, including dual-phase steels, transformation-induced plasticity (TRIP) steels, and high-manganese austenitic steels. But, in recent years, due to the huge demand for electric vehicles (EV), enhancement of fuel efficiency has become a major target in this field by reducing the vehicle weight, maintaining the safety of the passengers, and mainly enhancing the strength of the steel. A high degree of specific strength is often attained primarily through improving the strength of advanced steels (Grassel *et al.*, 2000; Fan *et al.*, 2009; Bhadeshia, 2010; Jang *et al.*, 2012). However, alternative way to improve the strength is to alloy lighter elements such as Al (and/or Si) in Fe-Mn-C alloy system. Al-based Fe-Mn-C has been researched for numerous applications, including (i) cryogenic applications, (ii) high-temperature oxidation resistance, and (iii) corrosion resistance. Along with this interesting application, this alloy system can be considered a suitable replacement for more expensive Fe-Cr-Ni base stainless steels (Lee *et al.*, 1992; Shih *et al.*, 1993; Saxena *et al.*, 1994; Zhu & Zhang, 1998; Herrmann, 2003; Hamada & Karjalainen, 2006; Morris *et al.*, 2006). Consequently, during the past 20 years, a lot of work has gone into creating ductile and lightweight steels that nevertheless have high strength and low density for structural purposes. However, Europeans and Japanese have studied this Fe-Mn-Al-C system since the early 2000s for automotive applications.

In 2006, Frommeyer and Brux (Frommeyer & Brux, 2006) researched the Fe-Al-Mn-C light weight alloys and reported an excellent high-strength and ductility combination, as well as further sketching out the TRIPLEX steels, which are regarded multiphase steels having three primary phases. They reported that microstructure of such TRIPLEX steels is composed of 5-15 vol.% of ferrite and nano-sized  $\kappa$ -carbides with less than 10 vol.%, which are finely distributed throughout the austenite matrix. The composition range of these types of steels is Fe-(18-28)Mn-(9-12)Al-(0.7-1.2)C (in wt%), where a typical alloy with the chemical composition Fe-28Mn-12Al-1C was formed, which exhibited a higher strength and ductility combination of 730 MPa of yield strength (YS), 1000 MPa of ultimate tensile strength (UTS) and 55% of elongation during room temperature (RT) under uniaxial tensile test with a very low strain rate of  $10^{-4} \text{ s}^{-1}$ . Lightweight high-Mn (>13 wt%) steels are widely recognized for

their superior strength-ductility combination and ability to satisfy the fundamental requirements of the automobile industry. Although the idea of lightweight steel appears to be quite straightforward, due to the presence of austenitic, ferritic, or even a multiphase structure depending on the content of primary alloying elements like C, Mn, or Al, the underlying metallurgical issues related to the material processing techniques are very complex, further complicating the deformation mechanism.

The mechanical behavior and corresponding deformation microstructure of face-centered cubic (fcc) metals/alloys are affected by several microstructural parameters such as stacking fault energy (SFE), grain size, local deformation microstructure, etc. Among them, one of the most important parameters that significantly influences the deformation behavior is the SFE of the concerned materials. Depending on the SFE value of the steel, a wide range of deformation mechanisms, ranging from transformation-induced plasticity (TRIP) (Grassel *et al.*, 2000), twinning-induced plasticity (TWIP) (Grassel *et al.*, 2000; Curtze & Kuokkala, 2012; Idrissi *et al.*, 2010), microband-induced plasticity (MBIP) (Yoo & Park, 2008), dynamic slip band refinement (Welsch *et al.*, 2016), dislocation plasticity (Riaz *et al.*, 2021), etc., are seen to operate either individually or collectively (De Cooman *et al.*, 2018). Strain-induced martensitic formation is seen to occur when the SFE of austenite is less than about 20 mJ/m<sup>2</sup>, whereas for SFE values greater than 20 mJ/m<sup>2</sup>, mechanical twinning mainly controls the deformation mechanism in high manganese (high-Mn) austenitic steels, which is known to be a twinning-induced plasticity (TWIP) effect (Olson & Cohen, 1976a, 1976b). Kim and De Cooman (2016) proposed a SFE-dependent deformation map for high-Mn steels, wherein they predict simultaneous incidence of twinning and transformation until the SFE limit  $\sim 13$  mJ/m<sup>2</sup>, while reckoning about intense twinning taking place in the SFE range: 13-40 mJ/m<sup>2</sup> and dislocation plasticity should predominate when SFE is above  $\sim 40$  mJ/m<sup>2</sup>. Transition of deformation microstructure from TRIP to TWIP in Fe-Mn-3Si-3Al alloys containing 15 to 25% Mn is reported by Frommeyer *et al.* (2000). They showed that the strain-induced martensitic transformation  $\gamma_{fcc} \rightarrow \epsilon_{hcp} \rightarrow \alpha'$ , i.e., the TRIP effect, dominates at 15-20% Mn concentrations, while any further increase in Mn content elevates the SFE of the system and changes the deformation mode to mechanical twinning, which means the TWIP effect predominates. However, De Cooman *et al.* (2018) also indicated several deviations from this SFE map, which led them to further propose that although SFE is required for the TWIP effect to occur, it is far from a sufficient characteristic..

In High-Mn steels, during deformation, dislocation cell formation takes place when the SFE is higher than 30-40 mJ/m<sup>2</sup> (Remy & Pineau, 1977). It is well known that dislocations must cross-slip in order to form dislocation cells, and it has also been observed that cross-slip occurs most frequently in high SFE alloys, whereas planar glide of dislocations is frequently observed during deformation of fcc metals/alloys with low SFE (Kuhlmann, 2001). However, some unusual behavior may be seen in this context: while having a high SFE, many Fe-Al-Mn-C austenitic steels prefer planar dislocation glide over wavy glide during deformation (Frommeyer & Brux, 2006; Yoo & Park, 2008; Choi *et al.*, 2010; Park *et al.*, 2010). Shear band formation could also be observed even at SFE  $\sim$  110 mJ/m<sup>2</sup> for Fe-28Mn-12Al-1C alloy by the planar glide of dislocation when the alloy was subjected to aging for 16h at 550°C (Frommeyer & Brux, 2006). Additionally, Park *et al.* noted that solution-treated Fe-28Mn-9Al-0.8C with SFE 85 mJ/m<sup>2</sup> underwent planar dislocation glide deformation (Yoo & Park, 2008). Planar dislocation glide in high-Mn steels was linked by Park *et al.* (2010) and Park (2013) to the glide softening phenomenon connected to short-range ordering (SRO) in the solid solution state.

Grain refinement is one of the important elements in the complex deformation mechanisms of high-Mn steels. The grain size of the austenite influences the mechanical twinning behavior of a given high-Mn steel, which further changes the deformation microstructure of that steel (Uejii *et al.*, 2007; Gutierrez *et al.*, 2008; Dini *et al.*, 2010; Gutierrez & Raabe., 2012a; Lee, 2012). Uejii *et al.* (2007) showed that mechanical twinning density is significantly decreased by refining the grain size from 49.6  $\mu$ m to 1.8  $\mu$ m for Fe-31Mn-3Al-3Si high-Mn steel when strain remains fixed, and this phenomenon is explained by Dini & Uejii (2012) through the development of a non-planar dislocation structure in the microstructure, while according to Gutierrez-Urrutia *et al.* (2008), grain refinement increases the critical twinning stress and retards mechanical twinning in Fe-22Mn-0.6C steel. Whereas an opposite scenario was observed by Gwon *et al.* (2020). They demonstrated that the coarse-grained TWIP steel exhibits a larger deformation twin percentage than the fine-grained TWIP steel. Rahman *et al.* (2015) discovered a significant proportion of stacking defects and very simple twin development in coarse-grained TWIP steel. According to Zan *et al.* (2015), coarse-grained TWIP steel exhibits early twin deformation nucleation, strong twinning activity, and high stress concentration at twin-twin intersections. According to Dini *et al.* (2010), as grain size increases, the critical strain for the formation of deformation twins decreases. This suggests that coarse-grained TWIP steel is more prone to twinning and deformation under stress compared to fine-grained TWIP steel. Furthermore, dislocation slip, Taylor lattice development, dislocation cell,

dislocation-twin interaction, and twin-twin intersections rendered the deformation mechanisms in coarse-grained high-Mn steel exceedingly complex. It is well known that different heterogeneous twin nucleation mechanisms in fcc materials follow the classical twinning models, which essentially comprise of numerous dislocation-based mechanisms (Venables 1974, Christian *et al.*, 1995; Niewczas *et al.*, 2002). However, Christian *et al.* (1995) propose that the deformation twin nucleates not just at areas with significant local stress concentrations, but is also influenced by a number of interconnected local variables such as grain size, grain orientation, precipitates, local SEF, and so on. Extensive study and numerous research paper already enriched this area of research field, but the relationship between high-Mn steel's microstructural features and mechanical properties is still not well established, and the present dissertation aims to provide newer insights in the deformation mechanisms of various high-Mn steel in terms of their tensile/compressive response behavior and corresponding deformation microstructures.

## **1.2 Mechanical response and strain hardening in metals/alloys and the associated stages**

It is well acknowledged that a material's associated microstructural data substantially correlates with the material's mechanical response. When examining the work-hardened Hadfield steels using thermo-magnetometry at room temperature in 1935, Chévenard made the first observation of the microstructural development with plastic strain as well as the emergence of a hard phase in the deformation microstructure (Chévenard, 1935). Later, Troiano and McGuire (1943) came to the conclusion that any hard phase evolution during plastic deformation results from the plastic strain imposed on the material. They also predicted that the mechanically induced phase transformation in Fe-Mn binary alloys can only happen in two mode of phase transformations:  $\epsilon$ -martensite and  $\alpha'$ -martensite. However, Schmidt was the first to identify the occurrence of the hexagonal  $\epsilon$ -martensite phase when analysing the deformation microstructure of Fe-Mn alloys with manganese levels ranging from 12 to 29 wt% (Schmidt, 1930). Researchers used optical micrographs to discover planar fault in deformed Hadfield steels for the first time in the 1950s, along with the occurrence of mechanical twinning (Doepken, 1952; Otte, 1957). After several years, scientists have now used a direct observation technique like TEM to prove the existence of deformation twinning (Roberts, 1964; Raghavan et al., 1969). In this context, it is crucial to remember that the types of deformation that were

applied to the specimen and which will be briefly reviewed later had a significant impact on the evolution of deformation microstructures.

### 1.2.1 Tensile and compressive response

Because of their high strength and ductility combinations, the research into the tensile deformation behavior of different grades of advanced high strength steels (AHSS) were greatly increased, which is an essential need for any automotive application. Several studies on the stress-strain response and strain hardening behavior of various grades of AHSS were conducted, and it was discovered that the various grades exhibit various forms of hardening behavior (Grassel et al., 1997; Grassel et al., 2000; De Cooman et al., 2018). Figure 1.1 shows the flow stress curve and the associated strain hardening behavior of various grade steels, including TWIP, high strength interstitial free (IF), and TRIP steels. It should be noted that TWIP steels with a strength of 1 GPa are taken into consideration in Fig. 1.1 for comparison. The TWIP steel has an interestingly higher UTS and about double the uniform elongation of the TRIP steel, as seen in Fig. 1.1. It is well known that TWIP steels have large uniform elongations because of the presence of deformation twins in the microstructures, but the precise

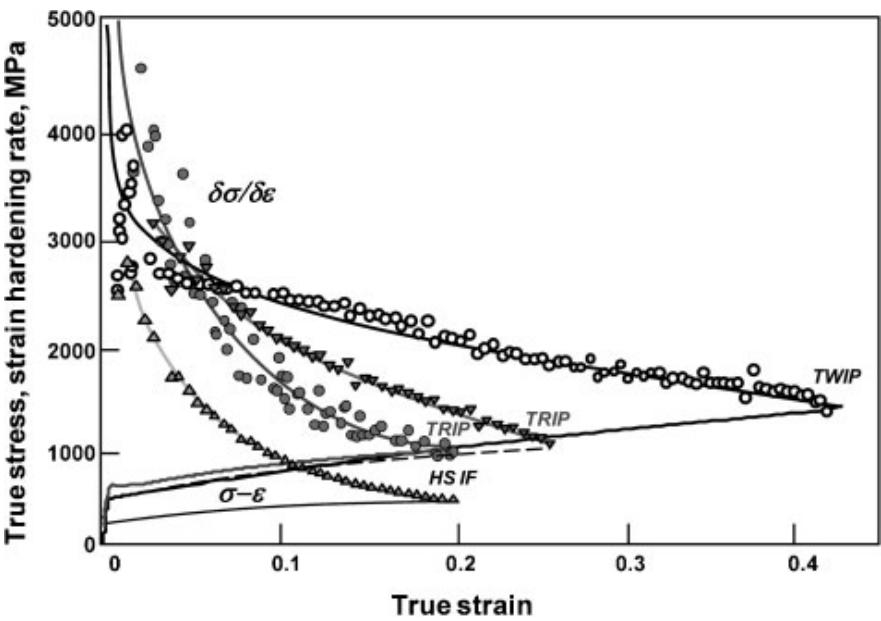


Fig. 1.1: Tensile response and strain hardening behaviour of different grade steels under monotonic deformation (De Cooman *et al.*, 2012).

reason why these twins appear and how they affect deformation behavior are still unclear (De Cooman *et al.*, 2018). In general, the imposed plastic strain in metals and alloys is used to produce various crystal imperfections which subsequently cause the substance to harden up to

a particular strain limit and ultimately fail. Although dislocation planar glide is the fundamental deformation for any metal or alloy during the early stage of deformation, the strain hardening process of various grades of steel differs depending on the types of defects formed in the deformation microstructure.

While analyzing large strain hardening responses, compression testing is preferred over tensile testing because the specimen can be smaller and simpler in size and shape without requiring specimen gripping. The majority of metallic materials behave symmetrically under uniaxial tension and compression. In other instances, however, tension and compression impose a different kind of strain route, resulting in a tension-compression asymmetry in a number of metallic materials, and the accompanying mechanical characteristics and microstructures become noticeably different (Yapici *et al.*, 2007; Chumlyakov *et al.*, 2008; Leidermark *et al.*, 2010). In a thorough analysis of the microstructural characteristics of high-Mn steel under compression stress, W. Pei *et al.* (2022) shown that the majority of the grains are deformed by twinning. However, other researchers found strong asymmetry while examining both tension and compression behavior. For sheet samples of TWIP steel tested in tension and compression in the rolling direction, Chung *et al.* (2011) found a little asymmetry that, after a strain of 0.03, the tension and compression curves quickly converged, showing the same strain hardening tendency in both directions but the circumstances is different when sample is strain in tension then compression. When a additively manufactured high entropy alloy made by is loaded through both tension and compression, Joseph *et al.* (2017) observed a considerable asymmetry in the mechanical behavior. They also demonstrated that the alloy exhibits persistent work hardening in compression, where twinning is the primary deformation mode, and limited work hardening in tension.

### **1.2.2 The Hall-Petch theory**

In the 1950s, Hall and Petch first demonstrated a revolutionary idea about the relation between yield stress ( $\sigma_{YS}$ ) and grain size which explained the grain boundary strengthening of a material i.e., strengthening of a material by changing the grain size according to the following relation that the yield stress ( $\sigma_{YS}$ ) and hence the hardness of any polycrystalline materials inversely varies with the square root of the grain size of that material. The variations of yield stress also further shown in Fig. 1.2 for a mild steel as a function of grain size, which clearly indicate the variation of yield stress with grain size according to the following relation (Hall, 1951; Petch, 1953):



$$\sigma_{YS}(MPa) = \sigma_{YS}^0 + \frac{k_{YS}^{HP}}{\sqrt{d}} \quad (1.1)$$

where the parameter  $\sigma_{YS}^0$  comprises of the lattice friction stress, the solid solution strengthening contribution of the alloying elements, and the strain hardening contribution of the initial dislocation density,  $k_{YS}^{HP}$  is a material parameter, and  $d$  is the average grain size (Armstrong, 2014).

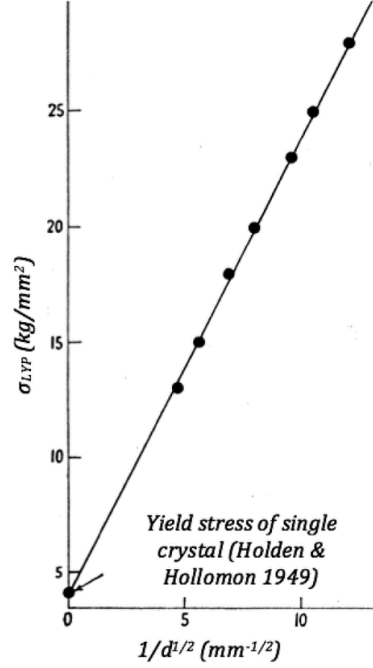


Fig. 1.2: The relationship between lower yield point ( $\sigma_{LYP}$ ) and grain size,  $d$ , in mild steel (Hall, 1951).

The Hall-Petch relation can be explained by a dislocation pile-up model where it is seen that due to disorderliness of grain boundary than the inside of the grain, dislocations cannot move in a continuous slip plane and pile up at the grain boundary and this impeding dislocation impede the onset of plasticity hence raising the yield strength of the material. Armstrong, 2014 and Cordero *et al.* (2016) explained the Hall-Petch effect considering the stress concentration at the tip of a slip band, however, the reliability of this relationship has lately come into doubt (Li, 2016). Prior to this, it was believed that because of the high-volume fraction of grain boundaries, materials with nanoscale grain sizes would be harder, more resistant to wear, and more fracture-resistant than materials with coarser grains because grain boundaries are known to be a major cause of metal deformation (Meyers *et al.*, 2006; Pande & Cooper, 2009), however in 1989, Gleiter (1989) pioneered his research work into polycrystalline materials,

and changed the concepts. Grain boundary weakening, also known as the "inverse Hall-Petch effect," has also been recorded for nanocrystalline materials with typical grain sizes of less than 30 nm, despite the fact that hardness measurements of some nanocrystalline samples were found to be in agreement with the Hall-Petch equation (Chokshi *et al.*, 1989; Koch & Narayan, 2000). Remarkably, the inverse Hall-Petch effect has been detected both experimentally (Chokshi *et al.*, 1989), as well as in molecular dynamics (MD) simulations (Schiotz & Jacobsen, 2003; Huang, 2018; Xu & Davila, 2018; Kuhr & Aifantis, 2019). Several scientists have attempted to interpret the grain boundary weakening, which is mainly due to (1) processing artifacts (Meyers *et al.*, 2006; Koch & Narayan, 2000), (2) disordered grain boundaries (Armstrong, 2016), and (3) an increased fraction of material within the grain boundaries (Carsley *et al.*, 1995; Carsley *et al.*, 1998). Another possible explanation made by Conrad (2004) considering effect of the transition of dislocation controlled to grain boundary and diffusion-dominated deformation (Pande & Cooper, 2009).

### 1.2.3 The stages of strain hardening

On the basis of mechanical response Diehl (1956) first divided the stress-strain curve of single crystals into three stages, which are clearly delineated in the flow-stress curve presented in Fig. 1.3. He also noted that stage I/A occurs only during the activation of a single slip system within a single crystal, whereas stage II/B is a linear hardening stage with relatively high work hardening rates, and it may occur in both the single and polycrystalline cases, this stage is also independent of stage I/A. However, this hardening behavior is considered to be the limiting case for small strains, as it becomes less effective with increasing temperature and SFE. Next coming to the stage III/C which actually a steady decrease stage in work hardening rate and this stage is quite sensitive to both, deformation temperature and strain rate. According to the theory of stage III/C when dynamic recovery of dislocation balances dislocation storage, saturation condition is reached and which is occurred at the end of stage III/C. For large deformations, another stage IV/D should be added to the work hardening curve. This stage exhibits a small amount of work hardening, possibly persisting to very large deformations. The hypothesis relating to stage III/C, which anticipates saturation of flow stress at the end of stage III/C, must be modified in order to account for the existence of a stage IV/D in work hardening rate plot. Some authors also mention the existence of a fourth stage, known as V/E, where additional dynamic recovery occurs and eventually causes the flow stress to really saturate.

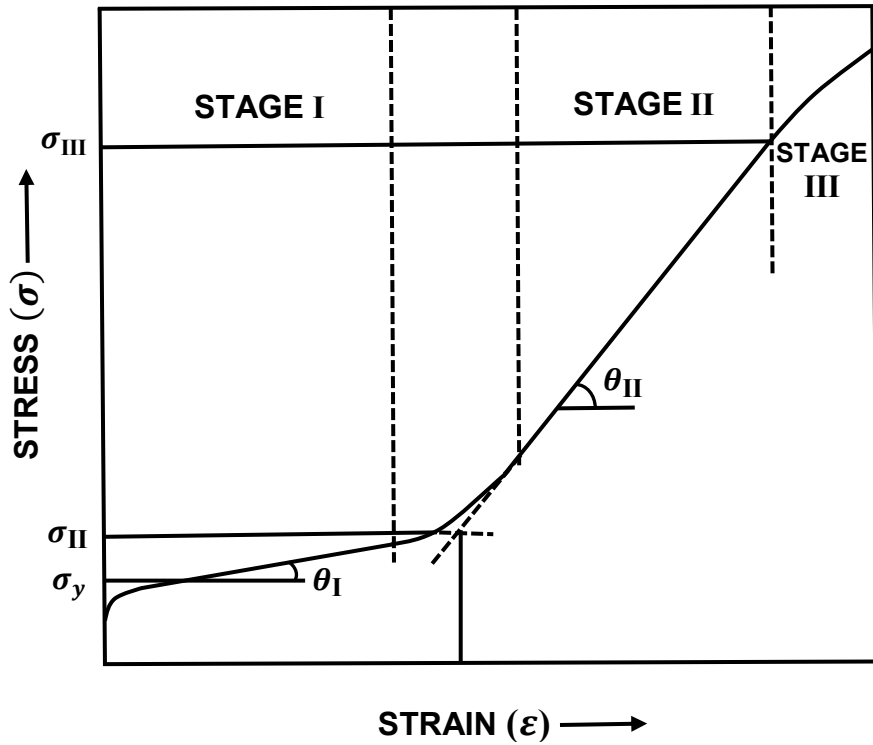


Fig. 1.3: The stages of work hardening, Stage I easy glide, Stage II athermal work hardening and Stage III dynamic recovery (Diehl,1956).

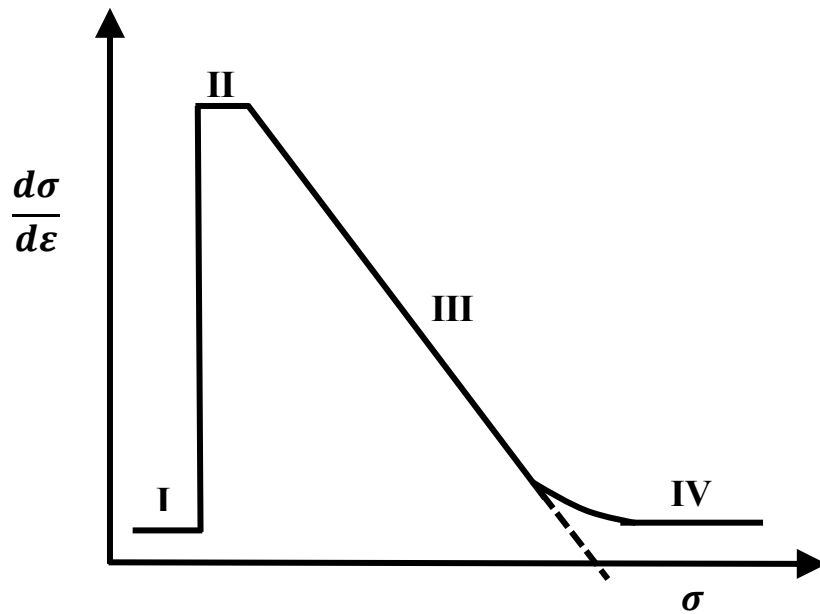


Fig. 1.4: Work hardening stages for a single crystal are depicted on a hardening rate vs flow stress diagram. A polycrystal would display stages III and IV, and maybe II as well (Rollt & Kocks, 1993)

The different stages of strain hardening can be more clearly distinguished using the variation of  $\theta$  with respect to  $\varepsilon$  where ( $\theta=d\sigma/d\varepsilon$ ) and the variation also graphically shown in

Fig. 1.4. It is important to note that stage II/B is common in low SFE materials and deforms only at low temperatures. The linear portion of the plot actually represented by the stage III/C defines the stage where the hardening rate decreases linearly with stress towards the 'saturation stress', wherein stages IV/D appears before the saturation stress is reached and commonly it is assumed as a constant or low hardening stage.

### 1.3 The factors influencing the deformation behavior of high-Mn steels

The aforementioned discussion (i.e. section 1.2) makes it abundantly clear that the evolution of various deformation microstructures as a result of applied plastic strain is substantially influenced by additional microstructural characteristics connected to metals and alloys in addition to the deformation process. This section will provide a quick overview of a number of microstructural factors and how they affect the corresponding deformation mechanism of various grades of steel, particularly high-Mn steels.

#### 1.3.1 SFE of austenite

The SFE of the material is one of many microstructural parameters that strongly affects the deformation behavior of metals or alloys, and it is fairly simple to predict the deformation microstructure by calculating the SFE of the material. The active deformation mechanisms of the steels, such as TRIP, TWIP, and MBIP, etc., which essentially regulate the mechanical properties of the metals/alloys, can be predicted based on the material's SFE value. Although the strain-induced twinning, or TWIP effect, appears to be connected to the inhibition of the athermal  $\gamma \rightarrow \epsilon$  martensitic transformation, it is still unknown why a threshold SFE value is necessary to activate distinct deformation mechanism. As a crucial parameter, scientists pay close attention to the experimental determination of SFE for various grades of steel and they discover that high-Mn steels with fully stable austenitic microstructures have an SFE value of 20-30 mJ/m<sup>2</sup> or more. (Schumann, 1972; Alder *et al.*, 1986; Mindownik, 1998; Yakubtsov *et al.*, 1999; Allain *et al.*, 2004a; Idrissi *et al.*, 2010; Pierce *et al.*, 2012; 2014;).

It is widely acknowledged that the critical SFE regime for observing TWIP effect in high-Mn steels is still a matter of debate, and there is a slight difference in the range of SFE value, which not only depends on the experimentally obtained scatter SFE value but is also strongly influenced by alloying compositions. Frommeyer *et al.* (2003) proposed that the TWIP effect in a stable austenite can be observed if the SFE value is greater than  $\sim 25$  mJ/m<sup>2</sup>, but Allain *et al.* (2004b) gave a smaller range for SFE mediated twinning. In addition, Dumay *et*

*al.* (2008) reported that they studied copper-containing Fe-Mn-C grade steels and found that deformation twinning tends to decrease below SFE  $\sim 18 \text{ mJ/m}^2$  and is replaced by the development of  $\epsilon$ -martensite platelets. However, the SFE values reported by Jin & Lee (2009) and De Cooman *et al.* (2011) for the Fe-18Mn-0.6C-1.5Al alloy were practically same, despite the fact that their indicated SFE values for activating deformation twinning were around  $\sim 3 \text{ mJ/m}^2$  apart.

Additionally, Pierce *et al.* (2015) investigated the impact of SFE on the evolution of the deformation microstructure and the strain-hardening behaviour of three (Fe-22/25/28Mn-3Al-3Si) TRIP/TWIP steels, and they proposed that the SFE of the alloy increased from 15 to 39  $\text{mJ/m}^2$  as the Mn content increased from 22 to 28 (in wt.%). They also stated that for the examined alloys, the optimal combination of UTS and total elongation could only be achieved when SFE values are between 15 and 39  $\text{mJ/m}^2$ , and that when SFE values are above  $\sim 39 \text{ mJ/m}^2$ , they drastically drop. It is possible to explain such inferior mechanical properties above the SFE value of  $\sim 39 \text{ mJ/m}^2$  by a decrease in the incidence of mechanical twinning in the deformation microstructure. Furthermore, it was also found that the deformation microstructure of Fe-25Mn-3Al-3Si steel having a SFE value of  $\sim 21 \text{ mJ/m}^2$  has a dislocation substructure that

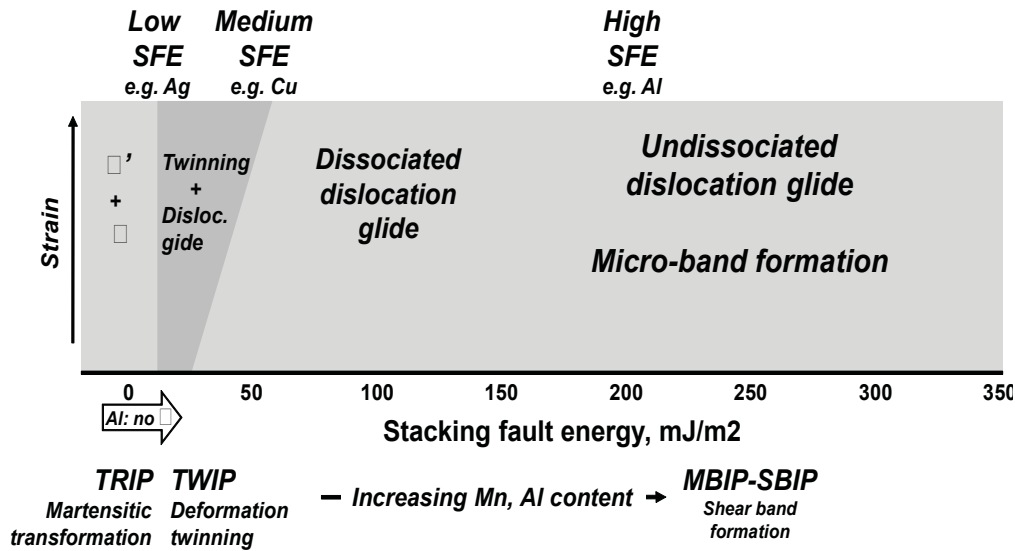


Fig. 1.5: Schematic showing the influence of SFE on the deformation mechanisms of f.c.c metals/alloys (De Cooman *et al.*, 2011).

exhibited both planar and wavy slip characteristics whereas the dislocation cross-slip increases in the case of Fe-28Mn-3Al-3Si having a higher SFE  $\sim 39 \text{ mJ/m}^2$ , which reduces the work-hardening rate in comparison to the lower SFE alloys. The effect of SFE on the deformation

mechanisms of various metals and alloys can be summarized in this context as shown in Fig. 1.5, which clearly shows that the activation of various deformation mechanisms in terms of the SFE of the materials. According to Fig. 1.5, as SFE rises from the low to the medium range, the deformation mechanism likewise changes from TRIP to TWIP. However, when SFE is extremely high, the material mostly deforms by the micro-band or shear band induced plasticity mechanism (MBIP or SBIP).

### 1.3.2 Grain size of austenite

It is well known that a material's grain size directly affects the mechanical behavior of the material, researchers recommend using the grain refinement technique to control the material's deformation microstructure and strength while maintaining its chemical composition (Ueji *et al.*, 2008). However, there is still little knowledge available regarding the grain size effect on both strength and ductility as well as the underlying deformation mechanism in fcc metals and alloys with low SFE, such as high-Mn steels. It is widely accepted that grain refining in high-Mn steels enhances the threshold stress while reducing ductility (Scott *et al.*, 2005; Ueji *et al.*, 2008). According to the Hall-Petch relationship, changes in grain size between 1 and 18  $\mu\text{m}$  predominantly affect the threshold (or initial yield) stress, as illustrated in Fig. 1.6 (Scott *et al.*, 2005).

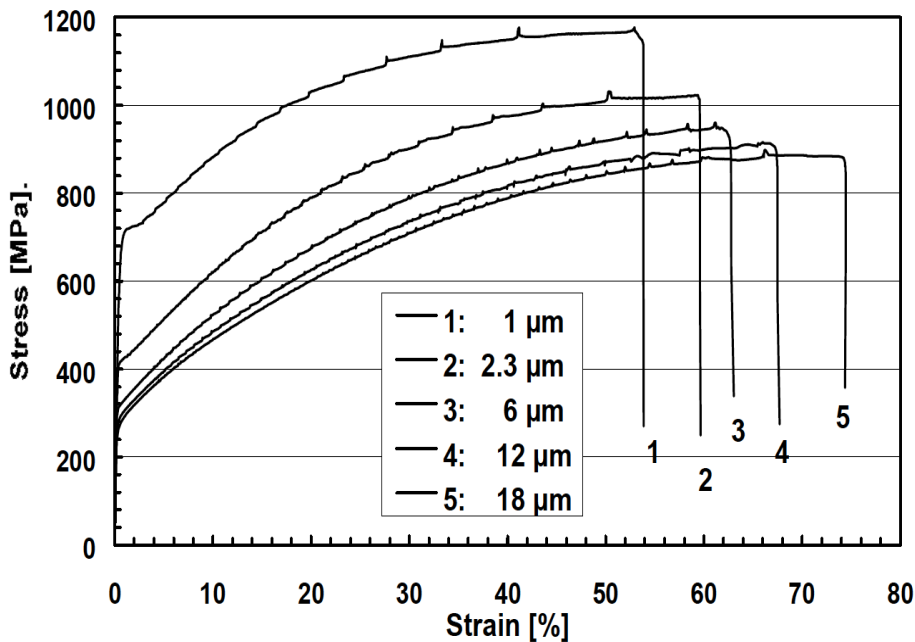


Fig. 1.6: Impact of grain size on the tensile response of Fe-22Mn-0.6C (Scott *et al.*, 2005).

The size of the grain determines the formation of the dislocation substructures, which in turn affects the twinning tendency in high-Mn steels (Gutierrez-Urrutia & Raabe, 2012a). According to Gutierrez-Urrutia *et al.* (2010), grain refinement in the  $\mu\text{m}$  range does not appear to prevent deformation twinning in Fe-22Mn-0.6C. As grain size is increased, according to Hall-Petch relationship both the YS and UTS decreases according to Hall-Petch relationship, while ductility increases while at the same time ductility increases (De Cooman *et al.*, 2009). Furthermore, it is demonstrated that the Hall-Petch parameter is independent of the high-Mn steel's mode of deformation; as a result, it has about the same value for both deformation twins and dislocation glide-dominated deformation microstructures (Gutierrez-Urrutia *et al.*, 2010). According to Ueji *et al.* (2008), fine-grained Fe-31Mn-3Al-3Si high-Mn steel exhibits high strength with appropriate ductility, as demonstrated in Fig. 1.7, unlike alloys with modest to high SFE. This finding shows that the significant ductility is attributable to both the suppressed dynamic recovery caused by low SFE and the twinning. Additionally, it has been found that in low SFE materials, the formation of twin and martensite may be fully inhibited by fine grains. (El-Danaf *et al.*, 1999; Asgari, 2004; Mohammed *et al.*, 2007). While examining the effects of grain size on the occurrence of deformation twins in high-Mn steels, prior research on several

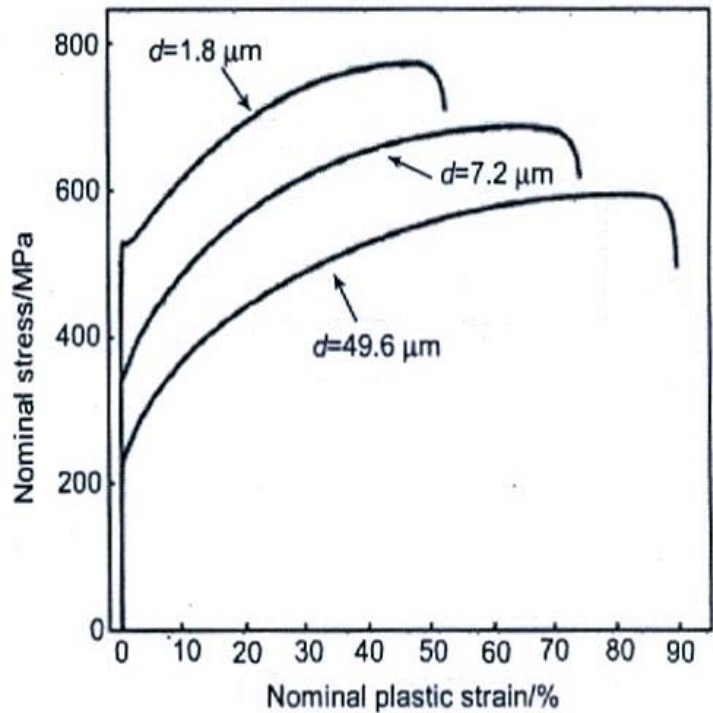


Fig. 1.7: Nominal stress strain curves of the Fe-31Mn-3Al-3Si high-Mn steel following 88% cold rolling and 700°C annealing ( $d = 1.8\mu\text{m}$ ), 800°C ( $d = 7.2\mu\text{m}$ ), or 1000°C ( $d = 49.6\mu\text{m}$ ) for 1800s (Ueji, *et al.*, 2008).

face-centered cubic metals and alloys suggested that a certain dislocation density is necessary for the twin to initiate; in other words, the twin forms following a specific plastic strain but prior to the dislocation structure.

**Table: 1.1:** RT tensile properties of Fe-28Mn-9Al-0.8C with three different grain sizes (Yoo *et al.*, 2009)

$d_A(d_{AT})/\mu\text{m}$	YS/ MPa	UTS/ MPa	Uniform elongation/%	Elongation /%	UTS*Elongation/MPa.%
5(3.5)	633	955	59.8	70.9	$6.7710 \times 10^4$
8(6.7)	539	903	69.8	82.3	$7.4317 \times 10^4$
38(14)	440	843	89.3	100.3	$8.4553 \times 10^4$

Yoo *et al.* (2009) investigated the variables influencing the tensile characteristics of high Fe-Mn-Al-C high-Mn steels using Fe-28Mn-9Al-0.8C steel. They noticed that when grain size decreased, strength increased and elongation decreased. As Table 1.1 illustrates, the coarse-grained steel's SHR continuously rose to a high strain level, producing very remarkable ductility, whereas that of the fine-grained steel stayed unchanged until the medium strain level. With decreasing grain size, YS and UTS increased but elongation showed the opposite trend. Despite the rise in strength, the product of UTS and total elongation also fell with decreasing grain size, demonstrating the steel's elongation dominant tensile properties.

Yoo & Park (2008) proposed that continuous increase of the SHR in high Mn austenitic resulting exceptionally high elongation of 100% which attribute the formation and intersection of the microbands composed of geometrically required dislocations, or what they refer to as "microband induced plasticity" (MBIP). Usually, microbands observed in the high-Mn Fe-Mn-Al-C austenitic steel run across the grain and also, they become crystallographic in nature. As a result, their scale of length corresponds to the order of grain size (Wilsdorf, 1989; Hughes, 1993) and therefore it is plausible that strain hardening via MBIP is saturated earlier in the fine-grained steel than the coarse-grained steel.

### 1.3.3 Grain orientation of austenite

It is well understood that when a bulk material is deformed under monotonic deformation i.e. the material undergoes through tensile or compressive loading, the influence of the imposed plastic strain does not apply to all of the material's grains equally; rather, it varies from grain



to grain and this variation depends on the Schmid factor assigned to the grains. It's interesting to note Schmid factor of a grain is closely connected with the grain's orientation with respect to the direction of the applied plastic strain therefore grain orientation should be taken care into consideration to understand the deformation mechanism of any material or alloy. According to several research (Kuprekova *et al.*, 2008; Gutierrez-Urrutia *et al.*, 2010; Sato *et al.*, 2011), the initial grain orientation has a significant impact on the nucleation of deformation twinning and the evolution of crystallographic texture. The impact of grain orientation on deformation twinning has also been the subject of numerous research, each of which offers a distinct explanation. Three of these hypotheses are roughly summarised in Fig. 1.8.

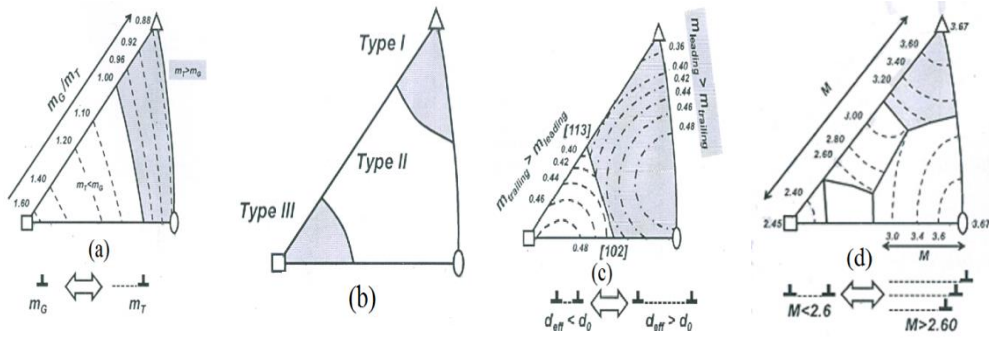


Fig. 1.8: (a) Schematic diagram demonstrating the impact of grain orientation on deformation twinning based on (Gutierrez-Urrutia & Raabe, 2011; Sato *et al.*, 2011). (b) The orientation range of type I and type II grains exhibit predicted behaviour based on their Schmid factor. (c) Diagram showing the impact of grain orientation on twinning deformation, as reported by Kireeva and Chemlyakov (Kuprekova *et al.*, 2008; Kireeva & Chemlyakov, 2009;) (d) diagram showing how grain direction affects deformation twinning as per (Beladi *et al.*, 2011).

According to Gutierrez-Urrutia *et al.* (2010) and Sato *et al.* (2011), relative value of the Schmid factor controls the impact of the grain orientation effect at low strain and they also suggested that twinning happens when the resolved shear stress for twinning is lower than the critical resolved shear stress for dislocation glide i.e:

$$(\tau_c)_{twin} = \tau_{crss} = m_T \sigma_A < \tau_G = m_G \sigma_A \rightarrow m_T < m_G \quad (1.2)$$

Where the product of the cosines of the angles between the direction of the applied tensile stress ( $\sigma_A$ ) and the slip plane normal and the direction of shear for a perfect dislocation ( $m_G$ ) or a partial dislocation ( $m_T$ ) is regarded as Schmid factor. This method is primarily based on the fact strong  $\langle 111 \rangle // t_d$  and a weak  $\langle 100 \rangle // t_d$  fiber orientations emerged during uniaxial

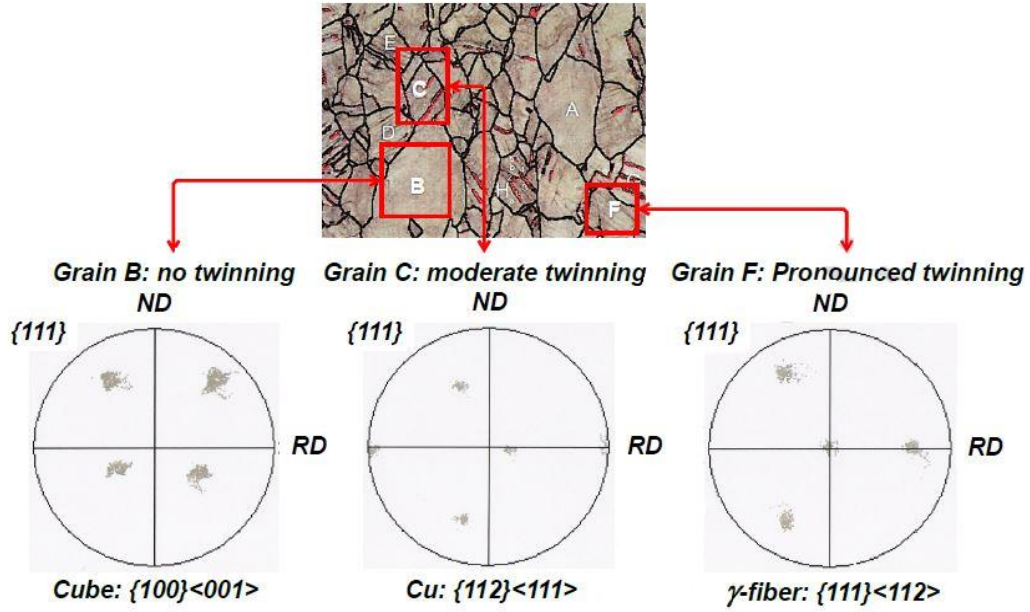


Fig. 1.9: An example of the effect of grain orientation on twinning in a tensile sample of high-Mn steel under 59% engineering strain. The C-grain, with its cube  $\{100\}\langle 011 \rangle$  orientation, does not have deformation twins, according to the pole figures of the individual grains. The B-grain, with its Cu  $\{112\}\langle 111 \rangle$  orientation, shows an intermediate twinning behaviour, and the f-grain, with its  $\{111\}\langle 112 \rangle$  (gamma fibre) orientation, is considerably twinned. The rolling and normal directions are shown by RD and ND, respectively, in this instance (Gutierrez-Urrutia & Raabe, 2012b).

tensile deformation of high-Mn steels. According to Fig. 1.9, grains that are  $\langle 111 \rangle // t_d$  oriented exhibit extensive twinning, whereas grains that are  $\langle 100 \rangle // t_d$  oriented have a significant absence of twins. Gutierrez-Urrutia and Raabe (2012b) examined Fe-22Mn-0.6C high-Mn steel ( $\text{SFE}=22 \text{ mJ/m}^2$ ) using the electron channelling contrast imaging (ECCI) technique, evaluated the grain orientation dependence mechanism experimentally, and shown that in real-world applications, the stringent Schmid law orientation dependency of slip and twinning in a tensile test is not valid. The only grains that behaved as expected based only on their Schmid factor were type I grains, which were favourably oriented for twinning because of their orientation extremely near to  $\langle 111 \rangle // t_d$ , and type III grains, which were favourably oriented for dislocation glide with an orientation extremely near to  $\langle 100 \rangle // t_d$ . Additionally, deformation twins were also discovered in type II grains, which, according to their Schmid factor, cover a wide range of orientations that are unfavourable for twinning. The deformation twinning in these unfavourably orientated grains was linked by Gutierrez-Urrutia & Raabe (2012b) to stress concentrations and strain gradients at grain borders.

According to Beladi *et al.* (2011), grains with orientations near to the Goss and Cube orientations were devoid of mechanical twins, whereas grains with orientations close to the Brass or Cu orientations were twinned. Beladi *et al.* (2011) also claim that the formation and development of twins require the activation of multiple slip system as well as the presence of high stress caused by dislocation pile-ups. According to Yang *et al.* (2006), texture development during uniaxial tensile deformation in a Fe-33Mn-3Al-3Si high-Mn steel confirms the theory that multiple slip occurs before twinning. The incredibly tiny deformation twins that formed had no impact on the evolution of texture. The twinned volume was reoriented to the slip-favoring CuT- $\{552\}\langle 115 \rangle$  orientation shown in Fig. 1.10. Uniaxial tensile deformation produced fibre orientations with a strong  $\langle 111 \rangle // t_d$  and a weak  $\langle 100 \rangle // t_d$ , according to Yang *et al.* (2006). Grain rotated towards the line as a result of slip. Additionally, they observed that stress along a direction of the kind  $\langle 111 \rangle // t_d$  promoted twinning as opposed to tension along  $\langle 100 \rangle // t_d$ , which did not.

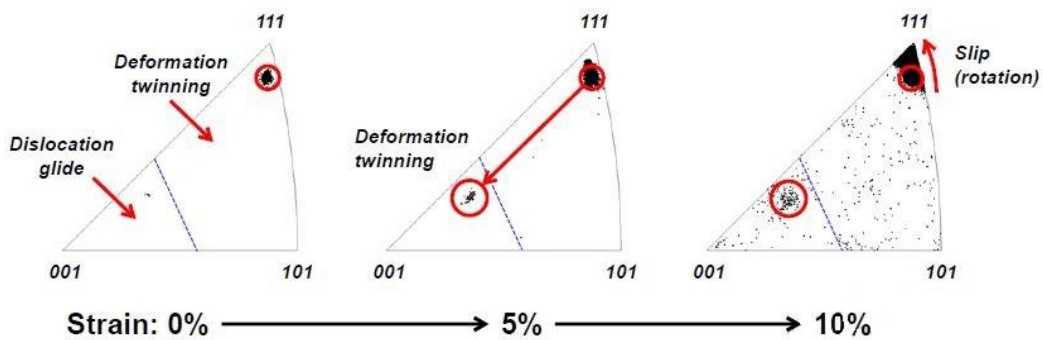


Fig. 1.10: Orientation shifts within a single grain, resulting in an orientation near to  $\langle 111 \rangle // t_d$ . Twinning definitely causes volume reorientation. Grain twins that were originally Cu  $\{112\}\langle 111 \rangle$  orientated readily to a CuT- $\{552\}\langle 115 \rangle$  orientation. Compared to deformation twinning, slip is preferable in this new orientation. Grain gradually rotates towards the  $\{001\}\langle 111 \rangle$  line in the fundamental stereographic triangle as a result of  $\{111\}\langle 100 \rangle$  dislocation slip. Under uniaxial stress, the dotted line distinguishes the orientations for which twinning and dislocation glide are the favoured deformation modes. Yang *et al.* (2006).

According to their findings, no twins were found in orientations close to those with the highest Schmid factor. Despite their high Schmid factors for twinning, twins were rarely found in grains with  $\langle 110 \rangle // t_d$  orientations even after an engineering strain as high as 20%. According to Yang *et al.* (2006), there are two ways in which the TWIP effect contributes to strain hardening: (a) by interactions between twin variations in  $\langle 111 \rangle$  oriented grains, and (b) through interactions between dislocations within deformation twins, whose orientation encourages dislocation glide.

### 1.3.4 Deformation temperature

It is seen that the strength and elongation of metals and alloys generally decrease as the deformation temperature rises therefore deformation temperature is expected to have a substantial impact on the evolution of the deformation microstructures. Wang *et al.* (2009) estimated the SFE of Fe-25Mn-3Si-3Al steel while focusing on the mechanical characteristics and the microstructure evolution between 25 – 400°C., taking into account Allain's (2004b) treatment. They found that at  $25^{\circ}\text{C} \leq T \leq 100^{\circ}\text{C}$ , deformation twinning is the dominating deformation process for  $21 \leq \text{SFE} \leq 34 \text{ mJ/m}^2$ , whereas slip predominates at high

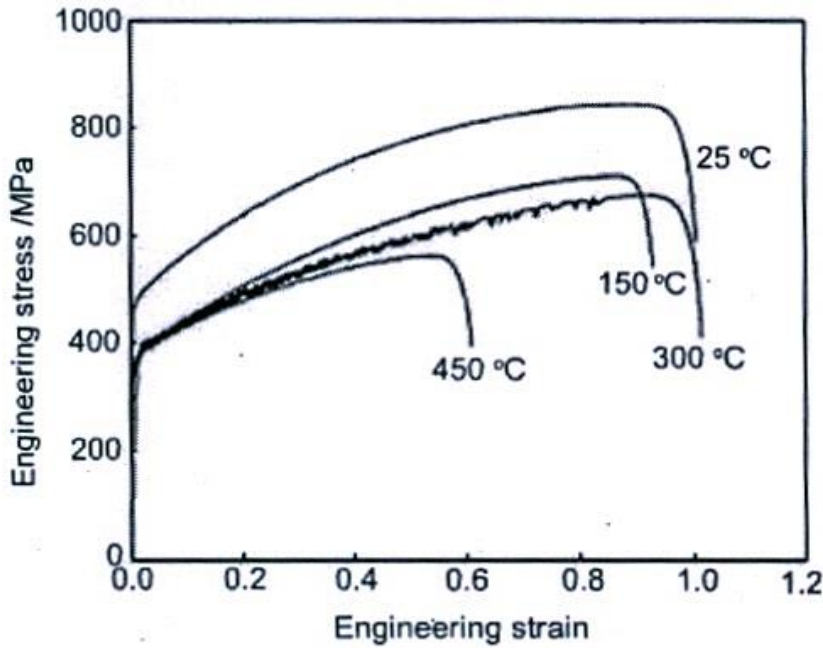


Fig. 1.11: The representative engineering stress-strain curves of the coarse-grained Fe-28Mn-9Al-0.8C tested at various temperatures with the initial strain rate of  $10^{-3}\text{s}^{-1}$  (Yoo *et al.*, 2009).

temperatures ( $T \geq 400^{\circ}\text{C}$ ) for  $\text{SFE} \geq 76 \text{ mJ/m}^2$ . With a low SFE, deformation twinning was favored because slip was inhibited, and the SFE value was predicted to decrease with decreasing temperature. A strong strain hardening effect occurs from deformation twins formed during plastic deformation, which function as barriers to dislocation migration, allowing substantial elongation and UTS to be observed at relatively low temperatures. Similar findings were also made by Tang *et al.* (2018) when they looked into how cold-rolled Fe-18Mn-3Al-3Si-0.03C high-Mn steel's microstructure evolved and its mechanical characteristics were affected by deformation temperatures. The investigated steel has a UTS of 905 MPa and a TEL

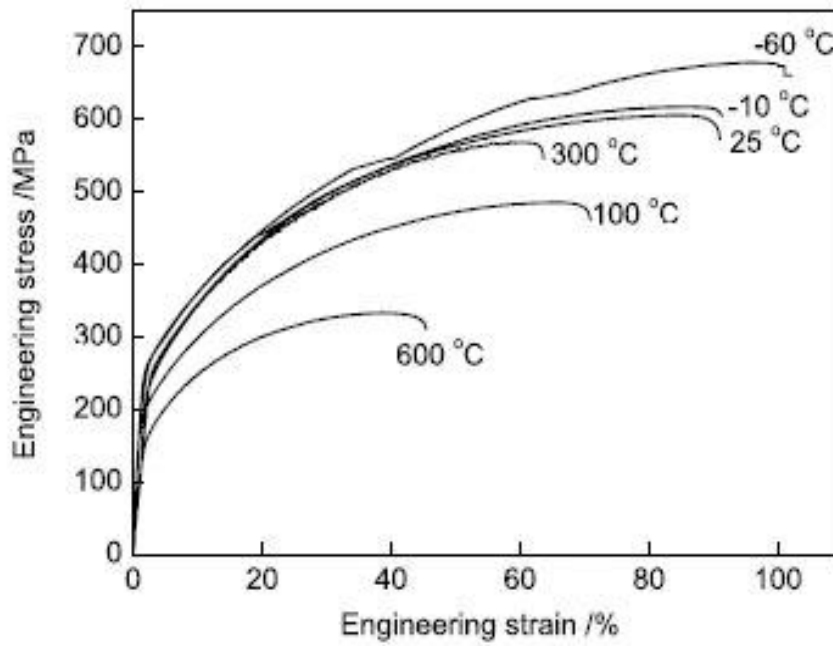


Fig. 1.12: Engineering stress-strain curves of Fe-23Mn-2Al-0.2C steel at various deformation temperature (Qin *et al.*, 2011).

of 55% at room temperature (RT), but these values monotonically decline to 325 MPa and 36%, respectively, when the deformation temperature rises to 400 °C. Additionally, they asserted that the TRIP and TWIP effects together control the majority of the high-Mn steel's deformation mechanism at room temperature (RT) whereas both of these effects were inhibited at a higher temperature and only dislocation glide remained active as a deformation mechanism during plastic deformation.

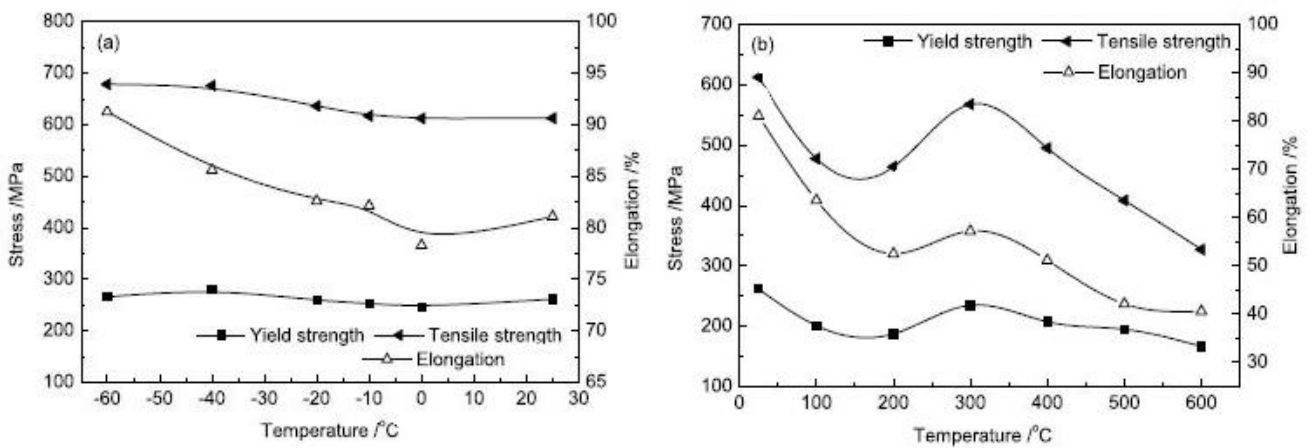


Fig. 1.13: Variations of the YS, tensile strength and elongation of Fe-23Mn-2Al-0.2C high-Mn steel with lower (a) and higher (b) deformation temperatures (Qin *et al.*, 2011).

High-Mn steels with high Al and C contents, however, show a unique circumstance in which elongation does not decrease with rising deformation temperature. When examining the flow curves of coarse-grained Fe-28Mn-9Al-0.8C steel tensile-tested with a strain rate of  $10^{-3}\text{s}^{-1}$ , Yoo et al. (2009) found that the UTS dropped with rising temperatures but the YS, which has a value lower than that at 25°C, was temperature-sensitive between 150 and 450°C. Their findings are shown in Fig. 1.11, which demonstrates that, with the exception of 300°C, total elongation reduced as temperature increased. Yoo *et al.* (2009) verified that the serrated flow at 300°C is predominantly caused by interactions between dislocations and interstitial atoms, rather than interactions between dislocations and substitutional atoms. The tensile deformation behavior of Fe-23Mn-2Al-0.2C high-Mn steel was investigated by Qin *et al.* (2011) throughout a broad range of temperature, from -60°C to 600°C (Fig. 1.12). According to Fig. 1.13, as the deformation temperature is raised, the steel's strength and elongation to failure first fall, then increase, and ultimately decrease, with the highest values occurring at 300°C. Additionally, they demonstrated that the SFE of the steel increases as the deformation temperature rises from -60°C to 600°C, changing the deformation mechanism from twinning to slipping. Through the use of electron microscopy, they also showed that, at 600°C, the microstructure is mostly composed of dislocations and dislocation cells, with high-density deformation twins that first emerge at lower deformation temperatures gradually disappearing with growing temperature.

### 1.3.5 Alloying elements

The primary purpose of Schumann's (1972) first investigation into the mechanical properties of Fe-Mn-C alloys was to determine how to achieve phase stability for the fcc crystal structure at room temperature through compositional analysis. Additionally, the author was able to clearly demarcate two zones in the Mn-C composition plane: one representing stable compositions deformed by twinning and dislocation gliding, and the other representing unstable compositions, or those that result in the phase formation triggered by deformation. It should be noted that the alloy composition has also a significant impact on the magnitude of SFE. As a result, the impact of the most essential alloying components on the characteristics of high-Mn TWIP steels is thoroughly examined.

### Manganese

It serves as the primary alloying element in TWIP steel. Its primary function is to enlarge the austenite phase area and stabilise the steel's austenite microstructure, as well as to enhance

hardenability. When the C content of steel remains constant, the microstructure developed is martensitic rather than pearlitic, which is subsequently changed into a single austenitic microstructure of the steel. The twinning process is also preferred with 15-25% Mn content. Another function of Mn is to regulate the SFE of steel in order to prevent the martensitic transition.

### **Aluminium**

The role of Al is to control the steel's SFE in order to stop the martensitic transformation. Al has the potential to increase the SFE and hence impede the shift from fcc to hcp. Consequently, Al plays a role in promoting the development of deformation twins, which increases TWIP steel's strength and plasticity (Grässel *et al.*, 1997; Grässel *et al.*, 2000; Hamada *et al.*, 2007). According to Hamada *et al.* (2007), Al may defer dynamic recrystallization, which would refine the austenite grain and significantly boost the thermal deformation resistance of high-Mn steel. Due to the increase in activation energy for carbon diffusion, Al additions also prevent the formation of Portevin-Le Chatelier (PLC) bands and move the region of serrated flow to higher temperatures (Kim *et al.* 2009; De Cooman *et al.*, 2012; Jim & Lee, 2012). The SFE is increased linearly with Al additions, preventing martensitic transition (Dumay *et al.*, 2008). For instance, adding 1.5% Al raises the SFE of Fe-18Mn-0.6C from 13 mJ/m<sup>2</sup> to 30 mJ/m<sup>2</sup> (Kim *et al.*, 2011), which in turn raises the  $(\tau_c)_{\text{twin}}$  or twinning (Park *et al.*, 2010; De Cooman *et al.*, 2012). According to Abbasi *et al.* (2009), adding Al improves yield strength while lowering ultimate tensile strength, elongation, and plastic deformation caused by twinning.

### **Silicon**

Si has a solution-strengthening effect and can dissolve in the austenite of TWIP steels. Additionally, Si can alter the solubility of C in austenite, making it difficult to determine the influence of Si on the mechanical characteristics of steels. In the cooling and deformation of TWIP steels, Si can lower the SFE and encourage the fcc-to-hcp phase transition (Vercammen *et al.*, 2004). In Fe-Mn-Si-C alloys with up to 8 at-%Si, Tian and Zhang (2009) found that SFE decreases as Si concentration increases. Jeong *et al.* (2013) confirmed this, finding that at Si concentrations up to 1.5 mass-%, SFE decreased at a rate of 4 mJm<sup>2</sup> per mass-% of Si.

### **Carbon**

Carbon plays a pivotal role in influencing various properties of high-Mn steel, such as: (a) improving the lattice parameter; (b) strengthening the austenite phase's stability in comparison

to  $\epsilon$ -martensite; (c) significantly increasing SFE, which is more pronounced for lower Mn content in Fe-Mn-C TWIP steels; and (d) having a strong solid solution hardening effect. For many microstructural features, the preferred placement of C atoms is crucial, and it is observed that the stacking fault energy is maximum when C atoms are located in the stacking fault plane. Furthermore, the further distant the C atoms are from the fault plane, the faster the impact of C on the stacking fault energy drops. Abbasi *et al.* (2011) noted a substantial correlation between the stacking fault energy and the location of the C atoms in relation to the stacking fault as well as a considerable rise in the stacking fault energy with increasing C content. The characteristics of C are impacted by substitutive solutes like Al and Mn. Although it has been demonstrated that Al has only a minor impact on the diffusivity of carbon in austenite Fe-C-Al alloys, however, according to Shun *et al.* (1992), the activation energy for bulk diffusion of carbon was much higher than the apparent activation energy for the commencement of DSA-related serrations on the deformation curves. They also showed that the activation energy for the start of serrations increased with the addition of 2.7% Al, demonstrating that Al lowers C mobility at dislocations.

#### **1.4 Critical twinning stress of high-Mn steel**

According to various mechanisms, such as the Venables pole mechanism (Venables, 1961), the Cohen & Weertman deviation process (Cohen & Weertman, 1963), or the Mahajan and Chin SF process (Mahajan & Chin, 1975), the formation of deformation twins is typically thought to be a defect assisted nucleation phenomenon preceded by dislocation activity. The experimental calculation of the twinning stress is notoriously challenging, despite the fact that several formulae are available to theoretically estimate the critical twinning stress ( $\tau_c$ )<sub>twin</sub> for certain deformation twinning models.

Twinning is activated in grains with the  $\langle 111 \rangle$  orientation in the tensile direction during tensile deformation. At RT, stage B of strain hardening, which corresponds to the flow stress, marks the beginning of deformation twinning in TWIP steels. Bouaziz *et al.* (2008) demonstrated that, for Fe-22Mn-0.6C TWIP steel, the twin nucleation stress was unaffected by grain size, at least throughout the 1.3-25  $\mu\text{m}$  grain size range. Under cyclic loading, Rahman *et al.* (2015) evaluated the twinning stress and its correlation to grain size, with the stress amplitude being below yield strengths (YS). According to their findings for a single crystal of Fe-15Mn-0.7C-2Al-2Si, critical twinning stress is 67 MPa. This number is comparable to the critical resolved



shear stress of 72 MPa for a Fe-22Mn-0.6C single crystal orientated to facilitate deformation twinning, that is, in compression along the [001]-axis, as reported by Choi *et al.* (2015).

Classical theories predict that  $(\tau_c)_{twin}$  is proportional to SFE,  $\gamma_{eff}$ :

$$\tau_c b_{112} \approx \gamma_{eff} \quad (1.3)$$

Narita & Takamura (1974) further report the following equation for  $(\tau_c)_{twin}$

$$(\tau_c)_{twin} = \frac{\gamma_{eff}}{2b_p} \quad (1.4)$$

where  $b_p$  is the partial dislocation's Burgers vector. Suzuki and Barrett (1958) made the assumption that a tiny dislocation segment made up of a sessile partial and a twinning partial pinned at two points serves as a twin nucleus. They defined  $(\tau_c)_{twin}$  as the critical stress for the partial bowing out of the twinning structure under the shear stress:

$$(\tau_c)_{twin} = \frac{\gamma_{eff}}{2b_p} + \frac{Gb_p}{L_0} \quad (1.5)$$

where  $L_0$  denotes the length of the sessile partial dislocation in the twin nucleus. The process of deformation twinning is then typically thought to be hindered by grain reduction, and Meyers *et al.* (2001) calculated the twinning stress trend using a grain-size dependent  $(\tau_c)_{twin}$  equation:

$$(\tau_c)_{twin} = \frac{\gamma_{eff}}{b_p} + \frac{K_T}{\sqrt{D}} \quad (1.6)$$

where  $K_T$  stands for temperature-dependent stress intensity and  $D$  for grain diameter. It is not totally understood how grain size affects the critical shear stress for twinning in high-Mn TWIP steel. While Mohammed *et al.* (2007) found an increase in the  $(\tau_c)_{twin}$  values with decreasing grain size, Phiu-on (2008) claims that the grain size has no influence on  $(\tau_c)_{twin}$ . In addition, Gutierrez-Urrutia & Raabe (2010) noted that for a Fe-22Mn-0.6C TWIP steel, a reduction in grain size led to a rise in the  $(\tau_c)_{twin}$  in the 3-50  $\mu\text{m}$  grain size range. They suggested the following grain size dependent equation:

$$(\tau_c)_{twin} = \frac{\gamma_{isf}}{2b_p} + \frac{Gb_p}{D} \quad (1.7)$$

where  $\gamma_{isf}$  is the intrinsic SFE. It is also logical to suppose that the three-layer twin nuclei discovered by Mahajan and Chin are multi-layer defects that already exist and are located at grain boundaries. When the stress reaches a critical level, these defects become active.

According to Steinmetz *et al.* (2013), the twin nucleus of a Mahajan and Chin three-layer twin is a small section located between two pinning sites. The  $(\tau_c)_{twin}$  is described by the following equation in terms of the creation of an unstable bow-out of the three twinning partials. (Steinmetz *et al.*, 2013):

$$(\tau_c)_{twin} = \frac{\gamma_{eff}}{3b_p} + \frac{3Gb_p}{L_0} \quad (1.8)$$

Eq. (1.8) offers extremely respectable values for the critical twinning stress for Fe-22Mn-0.6C TWIP steel, indicating that twins are triggered in the early stages of deformation.

### 1.5 A review on the grain size strengthening of high-Mn steels

Numerous studies have demonstrated that the yield stress,  $\sigma_{YS}$ , of polycrystalline high-Mn steels follows the Hall-Petch relation, which is stated in Eq. (1.1), and its validation for different high-Mn steels is shown in Fig. 1.14. Table 1.2 summarises the published data for the parameters  $\sigma_{YS}^0$  and  $k_{YS}^{HP}$  for a variety of high-Mn steels (Dini *et al.*, 2010; Bouaziz, *et al.*, 2011,

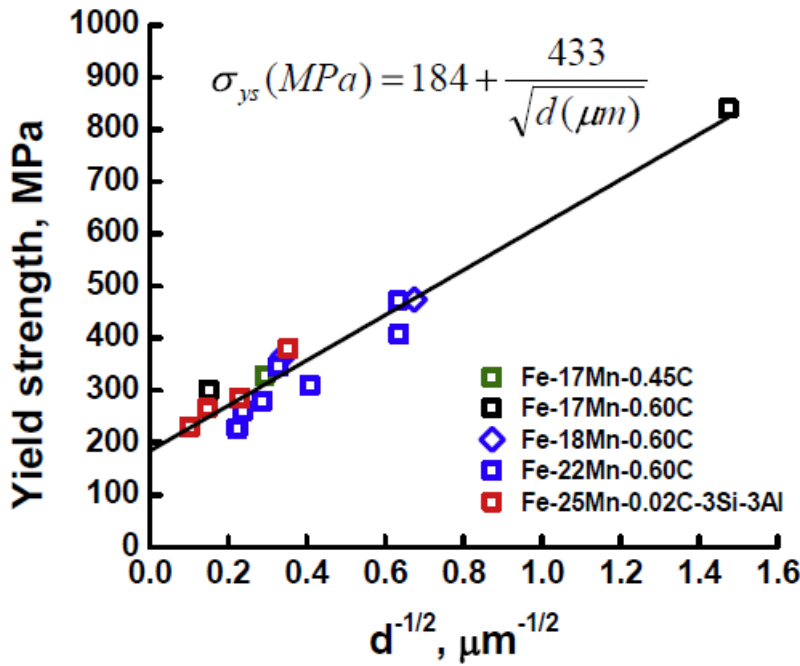


Fig. 1.14: Verification of the Hall-Petch relationship for several high-Mn steels (Fe-22Mn-0.6C (Scott *et al.*, 2011), Fe-17Mn-0.45C (Gwon, 2017), Fe-25Mn-3Si-3Al-0.02C (Wang *et al.*, 2009), Fe-17Mn-0.6C (Yen *et al.*, 2012).

Scott *et al.*, 2011., Sevillano & Cuevas, 2012; Shen *et al.*, 2016; Gwon, 2017; Rahman *et al.*, 2015). For polycrystalline Fe-22Mn-0.6C high-Mn steel, the values of  $\sigma_{YS}^0$  and  $k_{YS}^{HP}$  have been

**Table 1.2:** Parameters of the Hall-Petch relations for high-Mn steels

Alloys	$\sigma_{YS}^0$ MPa	$k_{YS}^{HP}$ , MPa $\mu\text{m}^{1/2}$	Reference
Fe-31Mn-3Al-3Si	53	764	Dini <i>et al.</i> (2010)
Fe-22Mn-0.6C	137	449	Bouaziz <i>et al.</i> (2011)
Fe-22Mn-0.6C	170	428	Scoot <i>et al.</i> (2011)
Fe-22Mn-0.6C	157	357	Gil Sevillano & Cuevas (2012)
Fe-20Mn-0.6C	158	485	Shen <i>et al.</i> (2016)
Fe-17Mn-0.45C-1.5Al-1Si (Hot rolled)	208	445	Gwon, (2017)
Fe-17Mn-0.45C-1.5Al-1Si (Hot rolled and recrystallization annealed)	403	445	Gwon, (2017)
Fe-15Mn-0.7C-2Al-2Si	305	330	Rahman <i>et al.</i> (2015)

reported to be 132 MPa and 449 MPa  $\mu\text{m}^{1/2}$  (14.2 MPa  $\text{mm}^{1/2}$ ), respectively. Since, the yield stress level is much lower than the value determined using the parameters from the same reference, therefore there appears to be some conflict with the  $\sigma_{YS}^0$  value provided by Bouaziz *et al.* (2011) in their original publication. As a result, the magnitude of  $\sigma_{YS}^0$  for polycrystalline Fe-22Mn-0.6C steel was re-evaluated, and De Cooman *et al.* (2018) got a revised magnitude for  $\sigma_{YS}^0$  of 242 MPa as opposed to 132 MPa, the value given by Bouaziz *et al.* (2011). Assuming a Taylor factor of 3.06, the equivalent critical resolved shear stress was calculated to be 79 MPa (Bouaziz *et al.*, 2011). For Fe-22Mn-0.5C-0.08N, De Cooman *et al.* (2018) obtained the following Hall-Petch equations for the YS and the UTS as:

$$\sigma_{YS}(\text{MPa}) = 219 + \frac{15.1 \text{ MPa mm}^{1/2}}{\sqrt{d(\text{mm})}} = 219 + \frac{477.5 \text{ MPa } \mu\text{m}^{1/2}}{\sqrt{d(\mu\text{m})}} \quad (1.9)$$

$$\sigma_{UTS}(\text{MPa}) = 754 + \frac{18.8 \text{ MPa mm}^{1/2}}{\sqrt{d(\text{mm})}} = 754 + \frac{594.5 \text{ MPa } \mu\text{m}^{1/2}}{\sqrt{d(\mu\text{m})}} \quad (1.10)$$

In order to assure equilibrium C segregation to the accessible grain boundary sites, Kang *et al.* (2016) examined the effect of the C content on the Hall-Petch coefficient  $k_{YS}^{HP}$  utilising a gradual cooling approach. They noticed that when the C concentration was increased from 0.3 mass-% to 0.6 mass-%,  $k_{YS}^{HP}$  increased from 218 MPa  $\mu\text{m}^{1/2}$  to 344 MPa  $\mu\text{m}^{1/2}$ . There are two possible explanations for this considerable rise in  $k_{YS}^{HP}$ . There are two possible explanations for this considerable rise in  $k_{YS}^{HP}$ , and the effect may be connected with either a greater stress for the activation of dislocation sources in a grain when the C content is increased.

Another proposed explanation was an increased density of grain boundary ledges functioning as dislocation causes (Li & Chou, 1970). The second theory is criticised by De Cooman *et al.* (2018) because the mechanism would result in a drop in  $k_{YS}^{HP}$  as C increased.

Alloying additions can change the Hall-Petch diagram for high-Mn steels, as shown in Fig. 1.15 for the example of alloying high-Mn steels with Ti, V, and Ni. Pre-strain during measurements is especially crucial because, in contrast to a-Fe and ferritic steels, where the slope of the Hall-Petch diagram,  $k_{YS}^{HP}$ , drops with increasing strain, austenitic steels' slope actually increases with strain. Additionally, the latter trend is seen with high-Mn steels. The Hall-Petch slope for the YS was around  $350 \text{ MPa } \mu\text{m}^{1/2}$ , while for the UTS, it was  $630 \text{ MPa } \mu\text{m}^{1/2}$ , according to Gil Sevillano (2009) and de las Cuevas *et al.* (2010). The results of Wang *et al.* (2009) for Fe-24.8Mn-0.022C-3.17Si-3.12Al validates that the Hall-Petch slope is higher for the UTS  $\sim 638 \text{ MPa } \mu\text{m}^{1/2}$ , while it is  $\sim 568 \text{ MPa } \mu\text{m}^{1/2}$  for the YS. Hall-Petch slopes of  $630 \text{ MPa } \mu\text{m}^{1/2}$  for the UTS and roughly  $350 \text{ MPa } \mu\text{m}^{1/2}$  for the YS were reported by de las Cuevas *et al.* (2010) and Gil Sevillano (2009), respectively. According to Wang *et al.* (2009)'s findings for Fe-24.8Mn-0.022C-3.17Si-3.12Al, the UTS's Hall-Petch slope is greater at  $638 \text{ MPa } \mu\text{m}^{1/2}$  than the YS's, at  $568 \text{ MPa } \mu\text{m}^{1/2}$ .

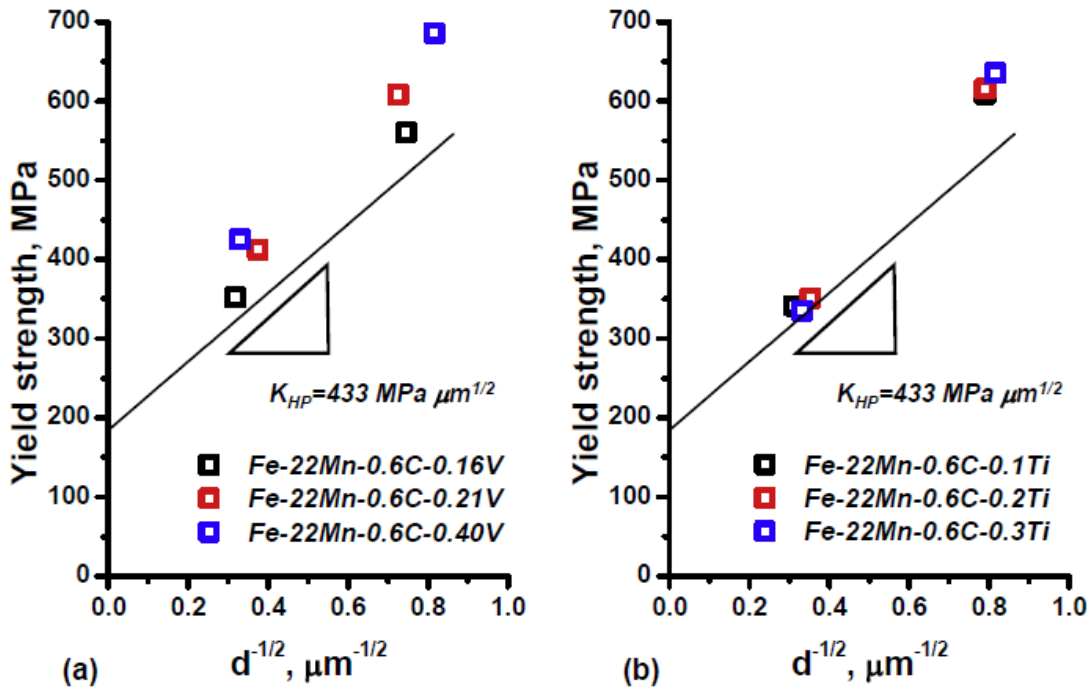


Fig. 1.15: Effect of (a) V and (b) Ti micro-alloying additions on the Hall-Petch diagram of high-Mn steel. (Scott *et al.*, 2011, Gwon, 2017).

With a few notable exceptions, it is widely acknowledged that grain refining to the submicron grain size,  $100 \text{ nm} < d < 1 \text{ }\mu\text{m}$ , leads to a decrease in strain hardening and, as a result, a reduction in uniform tensile elongation. (Valiev *et al.*, 2006; Estrin & Vinogradov, 2013). The ultrafine grained (UFG) materials maintain a significant post-uniform elongation in the necking area, demonstrating that plasticity as such is not suppressed. High-Mn steels have continuous elongation without any detrimental effects from small grain sizes. It is possible to get a wide range of grain sizes for a high-Mn steel through grain growth during recrystallization annealing. In C-free Fe-31Mn-3Al-3Si high-Mn steel (with SFE  $42 \text{ mJ/m}^2$ ), Ueki *et al.* (2007, 2008) observed that grain size reduction caused a severe suppression of deformation twinning and a significant decrease in ductility. In grains oriented in a  $\langle 111 \rangle$  direction near the tensile axis of fine-grained high-Mn steel, twinning was nevertheless common. According to Gutierrez-Urrutia *et al.* (2010), grain refinement made deformation twinning in a Fe-22Mn-0.6C high-Mn steel (intrinsic SFE  $23 \text{ mJ/m}^2$ ) more challenging but did not completely eliminate it. Additionally, they linked the reduced twin volume fraction to the observed smaller grain size. When Lee *et al.* (2012) examined the tensile deformation behaviour of UFG C-free Fe-17Mn and Fe-17Mn-0.6C high-Mn steels with that of the C-added high-Mn steel, they came to the conclusion that the latter's grain refinement-induced reduction in elongation was less pronounced. One thing to keep in mind is that high-Mn steels with grain sizes as small as  $2 \text{ }\mu\text{m}$  nevertheless had a significant uniform elongation of roughly 50% engineering strain. In a recent study (Timokhina *et al.*, 2014), the characteristics of a high-Mn steel with the composition Fe-22.3Mn-0.19Si-0.14Ni-0.27Cr-0.61C were examined by using the equal channel angular pressing (ECAP). It was shown that a suitable processing schedule selection may be employed to produce a UFG structure in the steel that has a reasonable balance between strength (1702 MPa) and tensile elongation (24%) in the steel. This was connected to the microstructure's development of deformation microbands and twins, including nano-twins, during the ECAP procedure.

## 1.6 Aims and scopes of the dissertation

The preceding debate on the interpretation of the deformation microstructure of high-Mn austenitic steels clearly indicated the significance of TWIP effect in displaying high strength and superior plasticity necessary for weight reduction of automotive structures and components (De Cooman *et al.*, 2018). Three types of high-Mn steels have so far been studied: Fe-Mn-C (Idrissi *et al.*, 2010), Fe-Mn-Al-C (Jin & Lee, 2012), and Fe-Mn-Si-Al (Idrissi *et al.*, 2013).

The most researched of these three varieties, Fe-Mn-Al-C, has a strong strength and ductility combination that can be achieved by controlling austenite SFE by adjusting Al in the steel (De Cooman *et al.*, 2018). Deformation twinning is severe in coarse-grained high-Mn steels, and most literature on TWIP steels assesses the deformation microstructure with an emphasis on the development of deformation twins, while similar attention is not paid to various dislocation substructures evolved during plastic deformation. In general, the significance of dislocation plasticity is ignored when strain hardening behaviour is explained in terms of the TWIP effect (De Cooman *et al.*, 2018), although other recent results suggest that the TWIP impact is overstated (Liang *et al.*, 2016; Luo & Huang, 2018; Zhi *et al.*, 2020).

Although low SFE is frequently associated with the occurrence of deformation twinning in fcc metals and alloys, particularly high-Mn steels, another significant but poorly understood component is grain size (De Cooman *et al.*, 2018). The creation of stacking faults (SF), deformation twinning, and dislocation glide are all commonly thought to be affected by grain size (De Cooman *et al.*, 2018). It's interesting to note that, there are also reports of an unanticipated effect of the grain size on the material's inherent SFE, notably in high-Mn steels, which may also have an indirect impact on these steels' propensity for twinning (De Cooman *et al.*, 2018). In general, twinning density is seen to be decreased by grain refinement; its coarse grain counterpart showed the reverse pattern. Where Gutierrez-Urrutia *et al.* (2008) showed that grain refinement retards mechanical twinning by increasing the critical twinning stress, Dini *et al.* (2010) found that coarse-grained TWIP steel is more prone to twinning and deformation under stress than fine-grained steel. Volosevich *et al.* (1976) first reported about the relationship between the grain size and SFE of binary Fe-Mn alloys, which was later supported by Takaki *et al.* (1993) and Lee and Choi (2000). This theory is based on grain size dependent internal stresses, which produce a shift in the dislocation dissociation width of the  $\frac{a}{2}\langle 110 \rangle$  dislocations. This has also recently been proven directly with TRIP for high-Mn steels with varying grain sizes (Chen *et al.*, 2021). To prevent the unanticipated effects of grain size, only coarse-grained steel was used in the current dissertation.

Furthermore, whereas dislocation activity is generally understood to be crucial to any plastic deformation, the presence of various forms of dislocation substructures in the deformation microstructures of high-Mn steels has not been extensively examined. It is seen that, the strain accommodation of high-Mn steels is mostly credited to deformation twinning, while the obstacle to dislocation glide at twin boundaries (TBs) also imparts an important

contribution (De Cooman *et al.*, 2018). High-Mn steels containing Al have better ductility and a substantially larger stacking fault energy (SFE) than Al-free steels, which is known to minimize twinning in such steels (De Cooman *et al.*, 2018). In addition to certain other plasticity processes, such as microband-induced plasticity (Park *et al.*, 2010) and dynamic slip band refinement (Welsch *et al.*, 2016), the presence of Al is also known to increase short-range ordering (SRO) (Yoo & Park, 2008), where the dislocation plasticity is predominate. The majority of the research on TWIP steels evaluates the deformation microstructure with a focus on the growth of deformation twins, whereas the numerous dislocation substructures developed during plastic deformation receive less attention. De Cooman *et al.* (2018) have stated unambiguously in their inspiring review that dislocation activity, rather than twinning, is the predominant plasticity mechanism in TWIP steels. However, determining their precise impact on the strengthening processes that regulate the deformation behavior of high-Mn steels remains a challenge. In a part of this study, we report the microstructure evolution in a high-Mn steel during quasi-static uniaxial tensile deformation, studied using transmission electron microscopy (TEM), with a particular emphasis on the evolution of dislocation substructures and their interaction in the microstructure.

A certain amount of plastic deformation is always necessary to activate deformation twinning since the critical stress for twinning is higher than the critical stress for slip (Huang *et al.*, 2006). It is also considered that prior dislocation activity is required for the nucleation of deformation twins in high-Mn steel, and a threshold dislocation density is required (El-Danaf *et al.*, 1999; Mahato *et al.*, 2015), but the critical SFE to produce twinning-induced plasticity continues to be debated (De Cooman *et al.*, 2018). SFE has been the subject of several prior findings that have suggested various deformation maps based on it (Remy & Pineau, 1976, 1977; Allain *et al.*, 2004; Kim & De Cooman, 2016). The favored method for modifying the deformation mechanism(s) in fcc metals/alloys is still composition-based SFE control (Dumay *et al.*, 2008; Saeed-Akbari *et al.*, 2009). However, a recent study on SFE estimate had shown that this method can be a dubious paradigm in low SFE fcc metals and alloys, such as the high-Mn steels (Werner *et al.*, 2021). SFE is still an important factor to consider when assessing the deformation behavior of high-Mn steels, thus it is important to calculate it accurately. A few relatively recent studies have already concluded that experimentally measured SFE might be better considered as apparent or effective values - diverging from theoretically derived values, since the latter are more intrinsic in nature (Pierce *et al.*, 2014;

Mahato *et al.*, 2015). Such apparent or effective SFEs involve an excess term besides the intrinsic SFE; known to arise from the critical resolved shear stress for twinning (Werner *et al.*, 2021). But in light of the aforementioned problems with intrinsic SFE in low SFE alloys, we investigate the room-temperature uniaxial tensile deformation behavior and the associated microstructure of three low carbon Fe-Mn-Al-C steels from a critical shear stress for twinning perspective. In order to interpret the deformation behavior, a critical shear stress of twinning-based approach has the advantage that the values can be compared with the shear stress values calculated from the ultimate tensile strength (UTS); assuming maximum stress concentration condition and in such cases the comparison of the deformation mechanism(s) in the steels is well supported. Additionally, the apparent or effective SFE was calculated using XRD pattern analyses, and some basic TEM investigations were also conducted to learn more specifically about the deformation microstructures. It is anticipated that a critical shear stress for twinning perspective would allow one to more accurately characterize the deformation behavior of high-Mn steels than one that relies solely on SFE regimes (Kim & De Cooman, 2016).

Due to the production of deformation twinning in their tensile-deformed specimens, high-Mn twinning induced plasticity (TWIP) steels have demonstrated remarkable mechanical characteristics with high strength and ductility; nevertheless, its compression counterpart has received little attention. Because most metallic materials exhibit symmetric uniaxial tension and compression behavior (Leidermark *et al.*, 2009), compression testing is preferred over tensile testing when studying large strain hardening responses because the specimen can be smaller and simpler in size and shape, removing the need for specimen gripping. However, tension and compression can impose a different sort of strain route in certain metallic materials, resulting in tension-compression asymmetry and markedly different mechanical characteristics and microstructures (Yapici *et al.*, 2007; Chumlyakov *et al.*, 2008; Leidermark *et al.*, 2010). As a result, it is critical to investigate the mechanical behavior and associated deformation microstructure of a steel under tension as well as compression. While studying numerous advanced high-strength steels (AHSS), an asymmetry in tensile-compressive loading was observed (Verma *et al.*, 2011; Sun *et al.*, 2013; Cyr *et al.*, 2018), but no such investigations were aimed at any high-Mn TWIP steel under both tensile and compressive loading. Finally, we investigated the true stress-strain curve of a Fe-Mn-Si-Al steel under tensile and compressive loading and interpret the flow stress and corresponding strain hardening behavior in terms of differently activated deformation mechanisms at different stage of deformation -



studied using synergistical applications of transmission electron microscopy (TEM), electron back scattered diffraction (EBSD), and X-ray diffraction (XRD) line profile analysis.

## References

- Abbasi, A., Dick, A., Hickel, T., Neugebauer, J. (2011) *Acta Mater.* **59**, 3041-3048
- Abbasi, M., Kheirandish, S., Kharrazi, Y., and Hejazi, J. (2009) *Mater. Sci. Eng. A*, **A513-A514**, 72-76.
- Allain, S., Chateau, J. P., Bouaziz, O., Migot, S. & Guelton, N. (2004a). *Mater.Sci. Eng. A*. **387-389**, 143-147.
- Allain, S., Chateau J. P., Bouaziz, O., Migot, S. & Guelton N. (2004b). *Mater.Sci. Eng. A*. **387-389**, 158-162.
- Armstrong, R. W. (2014) *Mater. Trans.* **55**, 2-12.
- Benito, J. A., Cobo, R., Lei, W., Calvo, J., Cabrera, J. M. (2016) *Mater. Sci. Eng. A* **655**, 310-320.
- Beladi, H., Timokhina, I. B., Estrin, Y., Kim, J., De Cooman, B. C. & Kim S. K. (2011). *Acta Mater.* **59**, 7787-7799.
- Bhadeshia, H. K. D. H. (2010) *Proc. R. Soc. Lond. A*. **466**, 3-18.
- Bouaziz, O., Allain, S., Scott, C., Cugy, P., Barbier, D. (2011) *Curr. Opin. Solid. St. M.* **15**, 141-168.
- Brofman, J., Ansell, G. S. (1978) *Metallurg. Trans. A* **9(6)**, 879-881.
- Chen, F. C., Chou, C. P., Li, P., and Chu, S. L. (1993) *Mater. Sci. Eng. A*, **160(2)**, 261-270.
- Chen, J., Dong, F., Liu, Z., & Wang, G. (2021) *J. Mater. Res. Technol.* **10**, 175-187. Chen, L., Kim, H. -S., Kim, S. -K. (2007) *ISIJ Int.* **47**, 1804-1812.
- Choi, K., Seo, C. H., Lee, H., Kim, S. K., Kwak, J. H., Chin, K. G., Park, K. T. & Kim, N. J. (2010) *Scr. Mater.* **63**, 1028-1031.
- Chateau, J. P., Dumay, A., Allain, S., Jacques, A. (2010) *Journal of Physics: Conference Series* **240**, 012023.
- Chévenard, P. (1935) *Métaux*. **10**, 203.
- Christian, J.W., Mahajan, S. (1995) *Prog. Mater. Sci.* **39**, 1-157.
- Chumlyakov, Y., Panchenko, E., Kireeva, I., Karaman, I., Sehitoglu, H., Maier, H.J., Tverdokhlebova, A., Ovsyannikov, A. (2008) *Mater. Sci. Eng. A* **481-482** 95-100.
- Chung, K., Ahn, K., Yoo, D.-H., Chung, K.-H., Seo, M.-H., Park, S.-H. (2011) *Int. J. Plast.* **27** 52-81.

- Clayton, P., Devanathan, R., Jin, N., Steele, R. K. (1992) *International conference on rail quality and maintenance for modern railway operation*, Delft, Kluwer Academic Publishers.
- Colette, G., Crussard, C., Kohn, A., Plateau, J., Pomey, G., Weiz, M. (1957) *Rev. Métall.* **54**(6), 433-86.
- Cordero, Z. C., Knight, B. E. & Schuh, C. A. (2016) *Int. Mater. Rev.* **61**, 495-512.
- Cornette, D., Cugy, P., Hildenbrand, A., Bouzekri, M., Lovato, G. (2005) *Rev. Métall.* **12**, 905-918.
- Curtze, S., Kuokkala, V.T. (2010) *Acta Mater.* **58**, 5129-5141.
- Cyr, E., Lloyd, A., Mohammadi, M. (2018) *Mater. Manuf. Process.* **35**, 289-294.
- Dai, Q.-X., Wang An-Dong, C. X.-N., Luo, X.-M. (2002) *Chin. Phys.* **11**(6), 596-600.
- Dastur, Y., Leslie, W. (1981) *Metall. Mater. Trans. A* **12**, 749-759.
- Das, S.R., Shyamal, S., Shee, S.K., Kömi, J.I., Sahu, P. (2021) *Mater. Charact.* **172**, 110833.
- De Cooman, B. C., Chen, L., Kim, H. S., Estrin, Y., Kim, S. K. & Voswinckel, H. (2009). *State of the science of high manganese twip steels for automotive applications, Microstructures and texture in steels*, ch.10. Halder A., Suwas, S. & Bhattacharjee, D. eds., Springer.
- De Cooman, B. C., Estrin, Y. & Kim, S. K., (2018) *Acta Mater.* **142**, 283-362.
- De Cooman, B.C., Chin, K.G. & Kim, J.Y. (2011) *New Trends and Developments in Automotive System Engineering*, Ed. M. Chiaberge, Publisher: InTech, Rijeka, Croatia.
- De Cooman, B.C., Estrin, Y. & Kim, S.K. (2018) *Acta Mater.* **142**, 283-362.
- Diehl, J. (1956) *Z. Metall.* **47**, 331.
- Dieudonné, T., Marchetti, L., Wery, M., Miserque, F., Tabarant, M., Chêne, J., Allely, C., Cugy, P., Scott, C. P. (2014) *Corros. Sci.*, **83**, 234-244.
- Dini, G. & Ueji, R. (2012) *Steel Res. Int.* **83**, 374-378.
- Dini, G., Najafizadeh, A., Ueji, R. & Monir-Vaghefi, S.M. (2010) *Mater. Des.* **31**, 3395-3402.
- Doepken, H. C. (1952) *J. Met.* **4**, 166-170.
- Dumay, A., Chatau, J.P., Allain, S., Migot, S. & Bouaziz, O. (2008). *Mater. Sci.Eng. A.* **483-484**, 184-187.
- El-Danaf, E., Kalidindi, S. R. & Doherty, R. D. (1999). *Metall. Mater. Trans. A.* **30A**, 1223-1233.
- Estrin, Y., Kubin, L. P. (1986) *Acta Metall.* **34**(12), 2455-2464.
- Estrin, Y. & Vinogradov, (2013) *Acta Mater.* **61**, 782-817.
- Fan, D. W., Kim, H. S. & De Cooman, B. C. (2009) *Steel Res.Int.* **80**, 241-248.
- Friedel, J.( 1964) *Dislocations*, Pergamon, Oxford, , pp 264.

- Frommeyer, G. & Brux, U. (2006) *Steel Res. Int.* **77**, 627-633.
- Frommeyer, G., Drewes, E. J. & Engl, B. (2000) *Rev. Metall. Cah. Inf. Tech.* **97**, 1245-1253.
- Frommeyer, G., Br  x, U., & Neumann, P. (2003). *ISIJ Int.*, **43**, 438-446.
- Fu, X., Wu, X. & Yu, Q. (2018) *Mater. Today Nano.* **3**, 48-53.
- Gleiter, H. (1989) *Prog. Mater. Sci.* **33**, 223-315.
- Grassel, O., Frommeyer, G., Derder, C., Hofmann, H. (1997) *J. Phys. IV* **7**, 383-388.
- Grassel, O., Kruger, L., Frommeyer, G. & Meyer, L. W. (2000) *Int. J. Plast.* **16**, 1391-1409.
- Gutierrez-Urrutia, I. & Raabe, D. (2011). *Acta Mater.* **59**, 6449-6462.
- Gutierrez-Urrutia, I. & Raabe, D. (2012) *Acta Mater.* **60**, 5791-5802.
- Gutierrez-Urrutia, I. & Raabe, D. (2012a). *Scr. Mater.* **66**, 992-996.
- Gutierrez-Urrutia, I. & Raabe, D. (2012b). *Mater. Sci. Forum.* **702-703**, 523-529.
- Gutierrez-Urrutia, I. & Zaefferer, S., Raabe, D. (2010) *Mater. Sci. Eng. A.* **66**, 3552-3560.
- Gwon, H. MS Thesis, Pohang University of Science and Technology, South Korea, 2017.
- Gwon, H., Kim, J. K., Shin, S., Cho, L., De Cooman, B. C. (2017) *Mater. Sci. Eng. A* **696**, 416-428.
- Gwon, H., Kim, J. H., Kim, J. K., Suh, D. W., Kim, S. J., Mater. Sci. Eng. A, 773 (2020) 138861.
- Hall, E. O. (1951) *Proc. Phys. Soc. Lond. B.* **64**, 747-753.
- Hamada, A. S. & Karjalainen, L. P. (2006) *Can. Metall. Q.* **45**, 41-48.
- Hamada, A. S., Karjalainen, L. P., Puustinen, J. (2009) *Mater. Sci. Eng. A* **517**, 68-77.
- Hamada, A. S., Karjalainen, L. P. (2010) *Mater. Sci. Eng. A* **527**, 5715-5722.
- Heinz, A., Neumann, P. (1990) *Acta Met. Mater.* **38**, 1933-1940.
- Herrmann, J., Inden, G. & Sauthoff, G. (2003) *Acta Mater.* **51**, 2847-2857.
- Hickel, T., Sandl  bes, S., Marceau, R. K. W., Dick, A., Bleskov, I., Neugebauer, J., Raabe, D., (2014) *Acta Mater.* **75**, 147-155.
- Hirsch, P. B.( 1975) *The Physics of Metals*, P. B. Hirsch (ed.), Cambridge University Press, Cambridge, , pp. 193.
- Hughes, D.A. (1993). *Acta Metall. Mater.* **41**, 1421-1430.
- Huang, C.X., Wang, K., Wu, S.D., Zhang, Z.F., Li, G.Y., Li, S.X. (2006) *Acta Mater.* **54**, 655-665.
- Idrissi, H., Renard, K., Ryelandt, L., Schryvers, D. & Jacques P. J. (2010). *Acta Mater.* **58(7)**, 2464-2476.
- Idrissi, H., Renard, K., Schryvers, D., Jacques, P.J. (2010) *Scr. Mater.* **63** 961-964.

- Idrissi, H., Renard, K., Schryvers, D., Jacques, P.J. (2013) *Philos. Mag.* **93**, 4378-4391.
- Jackson, P. J. (1983) *Mater. Sci. Eng.* **57**, 39-47.
- Jang, J. H., Lee, C. H., Heo, Y. U. & Suh, D. W. (2012) *Acta Mater.* **60**, 208-217.
- Jeong, J. S., Woo, W., Oh, K. H., Kwon, S. K., Koo, Y. M. (2012) *Acta Mater.* **60(5)**, 2290-2299.
- Jeong, K., Jin, J.-E., Jung, Y.-S., Kang, S., Lee, Y.-K. (2013) *Acta Mater* **61**, 3399-3410.
- Jin, J.E. & Lee, Y.K. (2009) *Mater. Sci. Eng. A.* **527**, 157-161.
- Jin, J.-E. & Lee, Y.-K. (2012) *Acta Mater.* **60**, 1680-1688.
- Joseph, J., Stanford, N., Hodgson, P., Fabijani, D. M. (2017) *Scr. Mater.* **129** 30-34.
- Jun, J. H. and Choi, C. S. (1998) *Mater. Sci. Eng. A* **257(2)**, 353-356.
- Kang, J.-H., Duan, S., Kim, S.-J., Bleck, W. (2016) *Metall. Mater. Trans. A.* **47**, 1918-1921.
- Kang, S., Jung, J. G., Kang, M., Woo, W. & Lee Y.K. (2016) *Mater. Sci. Eng. A.* **652**, 212-220.
- Kannan, M. B., Raman, R. S., Khoddam, S. (2008) *Corros. Sci.* **50**, 2879-2884.
- Katyk, S. A., Volodin, V. L., Zuev, L. B., Rasshchupkin, V. P., Dadotckin, N. V, Vulf, V. V. (1985) *Izvest. Vhz. Chermaya. Met.* **6**, 99-103.
- Kim, J.K. & De Cooman, B. C. (2016). *Mater. Sci. Eng. A.* **676**, 216-231.
- Kim, J., Lee, S. J., De Cooman, B. C. (2011) *Scr. Mater.* **65(4)**, 363-366.
- Kim, J., and De Cooman, B. C. (2011) *Metall. Mater. Trans. A* **42(4)**, 932-936.
- Kim, S.-D., Park, J. Y., Park, S.-J., Hoon Jang, J., Moon, J., Ha, H.-Y., Lee, C.-H., Kang, J.-Y., Shin, J.-H., Lee, T.-H. (2019) *Sci. Rep.* **9**, 1-13. 15171.
- Karjalainen, L. P., Hamada, A., Misra, R. D. K., Porter, D. A. (2012) *Scr. Mater.* **66**, 1034-1039.
- Kireeva, I.V., & Chumlyakov, Yu. I. (2009) *Phys. Met. Metallogr.* **108**, 298-309.
- Kubin, L.P., & Kratochvíl, J. (2000) *Philos. Mag. A.* **80**, 201-218.
- Kuhlmann-Wilsdorf, D. (2001) *Mater. Sci. Eng. A* **315**, 211-216.
- Kuprekova, E. I., Chumlyakov, Yu. I. & Chernov, I. P. (2008). *Met. Sci. Heat. Treat.* **50**, 282-288.
- Latanision, R. M., Ruff, A. W. (1971) *Metall. Trans.* **2(2)**, 505-509.
- Lee, P. Y., Chiu, C. S., Gau, Y. J. & Wu, J. K. (1992) *High Temp. Mater. Proc.* **10**, 141-144.
- Lee, S. -J., Kim, J., Kane, S. N., De Cooman, B. C. (2011) *Acta Mater.* **59**, 6809-6819.
- Lee, S., De Cooman, B. C. (2015) *Steel Res. Int.* **86**, 1170-1178.
- Lee, T., Koyama, M. Tsuzaki, K., Lee, Y.-H., Lee, C.S. (2012) *Mater. Lett.* **75**, 169-171.
- Lee, Y.-K. & Choi, C. (2000) *Metall. Mater. Trans. A* **31**, 355-360.

- Lee, Y.-K. (2012) *Scr. Mater.* **66**, 1002-1006.
- Lehnhoff, G. R., Findley, K. O., De Cooman, B. C. (2014) *Scr. Mater.* **92**, 19-22.
- Leidermark, D., Moverare, J.J., Johansson, S., Simonsson, K., Sjöström, S. (2010) *Acta Mater.* **58**, 4986-4997.
- Leidermark, D., Moverare, J.J., Simonsson, K., Sjöström, S., Johansson, S. (2009) *Comput Mater Sci.* **47(2)**, 366-72.
- Li, J. & Chou, Y. (1970) *Metall. Mater. Trans.* **1**, 1145.
- Li, Y., Bushby, A. J., Dunstan, D. J. (2016) *Proc. R. Soc. A.* **472**, 20150890.
- Liang, Z. Y., Li, Y. Z. & Huang, M. X. (2016) *Scr. Mater.* **112**, 28-31.
- Luo, Z. C. & Huang, M. X. (2018) *Scr. Mater.* **142**, 28-31.
- Mahajan, S. & Chin, G.Y. (1973) *Acta Mater.* **21**, 1353-1363.
- Mahajan, S., Jin, S., Brasen, D. (1980) *Acta Metall.* **28**, 971-977.
- McDermid, J.R., Bhadhon, K. M., McNally, E. A., Pallisco, D. M., Goodwin, F. E. (2016) In Proc. of the 108th Galvanizers Association Meeting, NW Resort, Farmingham, PA.
- McHargue, C. J., McCoy, H. E. (1963) *Amer. Inst. Min. Eng.* **227**, 1170.
- Miao, J., Pollock, T. M., Wayne Jones, J. (2012) *Acta. Mater.* **60**, 2840-2854.
- Miao, J., Pollock, T. M., Wayne Jones, J. (2009) *Acta. Mater.* **57**, 5964-5974.
- Mineur, M., Villechaise, P., Mendez, J. (2000) *Mater. Sci. Eng. A* **286**, 257-268.
- Miodownik, A.P. (1998). *Z. Metallkunde.* **89**, 840-847.
- Mohammed, A. A. S., El-Danaf, E. A. & Radwan, A. A. (2007). *Mater. Sci. Eng. A.* **457**, 373-379.
- Morris, D. G., Munoz-Morris, M. A. & Requejo, L. M. (2006) *Acta Mater.* **54**, 2335-2341.
- Nabarro, F. R. N. (1967) *Theory of Crystal Dislocations*, Oxford University Press, Oxford, , pp. 260.
- Nabarro, F. R. N., Basinski, Z. S. & Holt, D. B. (1964) *Adv. in Phys.* **13**, 193-323.
- Naik, S. N. & Walley, S. M. (2019) *J. Mater. Sci.* **55**, 2661-2681.
- Niendorf, T., Lotze, C., Canadinc, D., Frehnc, A., Maier, H. J. (2009) *Mater. Sci. Eng. A* **499**, 518-524.
- Niendorf, T., Rubitschek, F., Maier, H. J, Niendorf, J., Richard, H. A, Frehn, A. (2010) *Mater. Sci. Eng. A* **527**, 2412-2417.
- Niewczas, M., Saada, G. (2002) *Philos. Mag. A* **82**, 167-191.
- Oh, B. W., Cho, S. J., Kim, Y. G., Kim, Y. P., Kim, W. S. and Hong, S. H. (1995) *Mater. Sci. Eng. A* **197**, 147-156.
- Olson, G. B. & Cohen, M. (1976a) *Metall. Trans. A.* **7**, 1897-1904.

- Ookawa, A. (1957) *J. Phys. Soc. Japan* **12**, 825.
- Otte, H. M. (1957) *Acta Metall.* **5(11)**, 614-627.
- Park, K. T. (2013) *Scr. Mater.* **68**, 375-379.
- Park, K. T., Jin, K. G., Han, S. H., Hwang, S. W., Choi, K. & Lee, C. S. (2010) *Mater. Sci. Eng. A*. **527**, 3651-3661.
- Park, K.-T., Kim, G., Kim, S.K., Lee, S.W., Hwang, S.W., Lee, C.S. (2010) *Met. Mater. Int.* **16**, 1-6.
- Peng, X., Zhu, D. Y., Hu, Z. M. (2014) *J. Iron Steel Res. Int.* **21(1)**, 116-120.
- Petch, N. J. (1953). *J. Iron. Steel. Inst.* **174**, 25-28.
- Pei, W., Zhang, Y., Yang, S., Li, X., Zhao, A. (2022) *Mater. Res. Express* **9**, 066503.
- Pierce, D. T., Bentley, J., Jiménez, J. A. & J. E. Wittig. (2012). *Scr. Mater.* **66**, 753-756.
- Pierce, D. T., Jimenez, J. A., Bantley, J., Raabe, D. & Witting, J.E. (2015). *Acta Mater.* **100**, 178-190.
- Pierce, D.T., Jimenez, J. A., Berntley, J., Raabe, D., Oskay C. & Witing, J.E. (2014). *Acta Mater.* **68**, 238-253.
- Qin, X.M., Chen, L.Q., Di, H.S. & Deng, W. (2011). *Acta Metall. Sin.* **47**, 1117.
- Raghavan, K. S., Sastri, A. S., Marcinkowski, M. J. (1969) *Trans. Met. Soc. AIME* **245**, 1569-1575.
- Rahman, K., Vorontsov, V., Dye, D. (2015) *Acta Mater.* **89**, 247-257.
- Remy L. (1977) *Acta metall.* **25(2)**, 173-179.
- Remy, L. & Pineau, A. (1977) *Mater. Sci. Eng.* **28**, 99-107.
- Riaz, T., Das, S.R., Sahu, T., Chakraborti, P.C., Sahu, P., Mater. Lett. 282 (2021) 128691.
- Rittel, D., Roman, I. (1989) *Int. J. Fatigue* **11(3)**, 177-182.
- Roberts, W. N. (1964) *Trans. AIME* **230**, 372-377.
- Rolltt, A.D. & Kocks, U. F. (1993) *Solid State Phenom.* **35-36**, 1-18.
- Sato, Y. S., Kwon, E.P., Imafuku, M., Wagatsuma K., Suzuki, S. (2011). *Mater.Character.* **62**, 781-888.
- Saxena, V. K., Krishna, M. S. G., Chhaunker, P. S. & Radhakrishnan, V. M. (1994) *Int. J. Press. Vessels Pip.* **60**, 151-157.
- Schmidt, W. (1930) *Arch. Eisenhüttenwes.* **3**, 293.
- Schumann, V.H. (1972). *NeueHütte.* **17**, 605-609.
- Scott, C., Guelton, N., Allain, S. & Faral, M. (2005). *Mater. Sci. Technol. Conf.*, **2**, 127-138.
- Scott, C., Remy, B., Collet, J.-L., Cael, A., Bao, F. Danoix, C., Malard, B. Curfs, C. (2011) *Int. J. Mater. Res.* **102**, 538-549.

- Seo, W., Jeong, D., Sung, H., Kim, S. (2017) *Mater. Charact.* **124**, 65-72.
- Sevillano, J.G. & de Las Cuevas, F. (2012) *Scr. Mater.* **66**, 978-981.
- Sevillano, J.G. (2009) *Scr. Mater.* **60**, 336-339.
- Shao, C. W., Zhang, P., Wang, X. G., Wang, Q., Zhang, Z. F. (2019) *Mater. Res. Lett.* **7(1)**, 26-32.
- Shen, Y., Jia, N., Misra, R., Zuo, L. (2016) *Acta Mater.* **103**, 229-242.
- Shih, S. T., Tai, C. Y. & Perng, T. P. (1993) *Corrosion* **49**, 130-134.
- Shun, T., Wan, C., Byrne, J. (1992) *Acta Metall. Mater* **40**, 3407-3412.
- Sun, L., Wagoner, R.H. (2013) *Int J Plast.* **45**, 174-87.
- Takaki, S., Nakatsu, H. & Tokunaga, Y. (1993) *Mater. Trans. JIM.* **34**, 489-495.
- Tang, Z., Huang, J., Ding, H., Cai, Z., Zhang, D., Misra, D. (2018) *Metals.* **8(7)**, 476.
- Tian, X., Li, H. and Zhang Y. (2008) *J. Mater. Sci.* **43(18)**, 6214-6222.
- Tian, X., Zhang, Y. (2009) *Mater. Sci. Eng. A* **516(1-2)**, 73-77.
- Timokhina, I., Medvedev, A., Lapovok, R., (2014) *Mater. Sci. Eng. A.* **593**, 163-169.
- Timokhina, I. B., Hodgson, P. D., Pereloma, E. V. (2004) *Metall. Mater. Trans. A* **35(8)**, 2331-2341.
- Tirry, W., Schryvers, D. (2005) *Acta Mater.* **53**, 1041-1049.
- Troiano, A. R. & McGuire, F. T. (1943) *Trans. ASM* **31**, 340-346.
- Uejii, R., Tsuchida, N., Fujii, H., Kondo, D., Kunishige, K. (2007) *J. Jpn. I. Met.* **71**, 815-821.
- Uejii, R., Tsuchida, N., Terada, D., Tsuji, N., Tanaka, Y., Takemura, A. & Kunishige, K. (2008) *Scr. Mater.* **59**, 963-966.
- Valiev, R.Z., Estrin, Y., Horita, Z., Langdon, T.G., Zechetbauer, M.J., Zhu, Y.T. (2006) *JOM* **58**, 33-39.
- Venables, J. A. (1961) *Philos. Mag.* **6**, 379-396.
- Venables, J. A. (1964) *J. Phys. Chem. Solids.* **25**, 685-692.
- Venables, J.A. (1974) *Philos. Mag.* **30**, 1165-1169.
- Verma, R.K., Chung, K., Kuwabara, T. (2011) *Isij Int.* **51**, 482-90.
- Vitek, V. (1968) *Philos. Mag.* **18**, 773-786.
- Vitek, V. (1970) *Scr. Metall.* **4**, 725-732.
- Volosevich, P., Gridnev, V. & Petrov, Y. (1976) *Phys. Met. Metallogr.* **42**, 126-130.
- Wang, L., Guan, P., Teng, J., Liu, P., Chen, D., Xie, W., Kong, D., Zhang, S., Zhu, T., Zhang, Z., Ma, E., Chen, M., Han, X. (2017) *Nat. Commun.* **8**, 1-7.
- Wang, X. D., Huang, B. X., & Rong, Y. H. (2006). *Mater. Sci. Eng. A*, **438-440**, 300-305.
- Wang, X., Liang, Z. Y., Liu, R. D., Huang, M. X. (2015) *Mater. Sci. Eng. A* **647**, 249-255.

- Welsch, E., Ponge, D., Hafez Haghighat S.M., Choi, P., Herbig, M., Zaefferer, S., Raabe, D. (2016) *Acta Mater.* **116**, 188-199.
- Werner, K. V., Niessen, F., Villa, M., Somers, M. A. J. (2021) *Appl. Phys. Lett.* **119**, 141902.
- Wilsdorf, D. K. (1989). *Mater. Sci. Eng. A*, **113**, 1-41.
- Wu, Y.- X., Tang, D., Jiang, H. -T., Mi, Z. -L.; Xue, Y., Wu, H. -P. (2014) *J. Iron Steel Res. Int.* **21**, 352-358.
- Yakubtsov, I. A., Airapour, A. & Perovic, D. D. (1999). *Acta Mater.* **47**, 1271-1279.
- Yamakov, V., Wolf, D., Salazar, M., Phillpot, S. R., Gleiter, H. (2001) *Acta Mater.* **49**, 2713-2722.
- Yapici, G.G., Beyerlein, I.J., Karaman, I., Tomé, C.N. (2007) *Acta Mater.* **55**, 4603-4613.
- Yen, H. W., Huang, M., Scott, C. P., Yang, J. R., (2012) *Scr. Mater.* **66(12)**, 1018- 1023.
- Yoo, J. D. & Park, K. T. (2008) *Mater. Sci. Eng. A*. **496**, 417-424.
- Yoo, J. D., Hwang, S. W. & Park, K. T. (2009). *Mater.Sci. Eng. A*, **508**, 234-240.
- Zambrano, O. A. (2016) *J. Eng. Mater Technol.* **138(4)**, 041010.
- Zan, N., Ding, H., Guo, X., Tang, Z., Bleck, W. (2015) *Int. J. Hydrogen Energy* **40**, 10687-10696.
- Zhi, H., Zhang, C., Antonov, S., Yu, H., Guo, T., Su, Y. (2020) *Acta Mater.* **195**, 371-382.
- Zhu, Y. T., Liao, X. Z., Wu, X. L. (2012) *Prog. Mater. Sci.* **57**, 1-62.
- Zhu, X. M. & Zhang, Y. S. (1998) *Corrosion*, **54**, 3-12.



# *Chapter 2*

## *Methodologies adopted for microstructure characterization*



## 2.1 Determination of extended defect and the underlying principles

A large number of methods already exist to study the defect of a crystal arising from the disruption of lattice periodicity due to applied strain. Some method helps us to get direct observation of the defect whereas some methods give the quantitative information of different microstructural parameters such as dislocation density, dislocation outer cut-off radius and dislocation character to identify the defect present in the sample. These approaches may be divided into two categories: (I) Direct observation and (II) indirect observation. Different methods used to detect and characterized the defect of a sample are discussed here.

*(I) Direct method:*

(i) Field ion microscopy method for etching and decorating (ii) X-ray and synchrotron X-ray tomography (iii) Secondary ion mass spectroscopy (iv) High and low energy electron diffraction (v) X-ray fluorescence (vi) Auger and photoelectron spectroscopy (vii) Transmission, scanning, scanning transmission and high-resolution electron microscopy

*(II) Indirect method:*

(i)Electrical resistivity (i) Ultrasonic method (ii) Solid diffusion (iii) XRD and small angle X-ray scattering (iv) Neutron irradiation (v) Replica electron microscopy (vi) Mossbauer spectroscopy

Indirect method namely, XRD analysis is used to determine the defect and characterize the microstructures of a sample via different microstructural parameters obtained from the XRD peak profile analysis and the direct method mainly, TEM is used to confirm the corresponding defect via direct observation.

## 2.2 X-ray diffraction

X-ray diffraction is a common and useful method for studying the microstructure of a sample by measuring various structural and microstructural parameters. To study the nature of imperfection introduced during crystal growth of sample preparation or during plastic deformation, it may be tensile testing or fatigue testing, X-ray diffraction technique is the very useful indirect methods. X-ray diffraction is actually a scattering-phenomena arising from the scattering of X-ray from different atoms in the sample and their interference. Scattered X-ray from the atoms with same phase or integral multiple of the wavelength of X-ray when interfere constructively by maintaining the Bragg's law, we get X-ray diffraction peak. If  $d_{hkl}$  be the

interplanar spacing of set of parallel planes defined by particular miller indices ( $hkl$ ) and  $\theta$  be the angle between the incident X-ray and that particular planes for constructive interference called Bragg angle then Bragg equation can be written as

$$2d_{hkl} \sin \theta = n\lambda \quad (2.1)$$

where  $\lambda$  is the wavelength of the X-rays and  $n$  is the integer represent order of diffraction.

Due to the presence of particular set of characteristic interplanar spacing  $d_{hkl}$  for an ideal crystal, the diffraction patterns observed at the perspective Bragg angle  $\theta$  are to be all discrete lines but in general for real crystal broad peaks are observed due to lack of perfectly parallel and monochromatic beam and departure from perfect crystal. A schematic representation of Bragg's law and an image of the X-ray diffractometer used here for X-ray scanning are shown in Fig. 2.1.

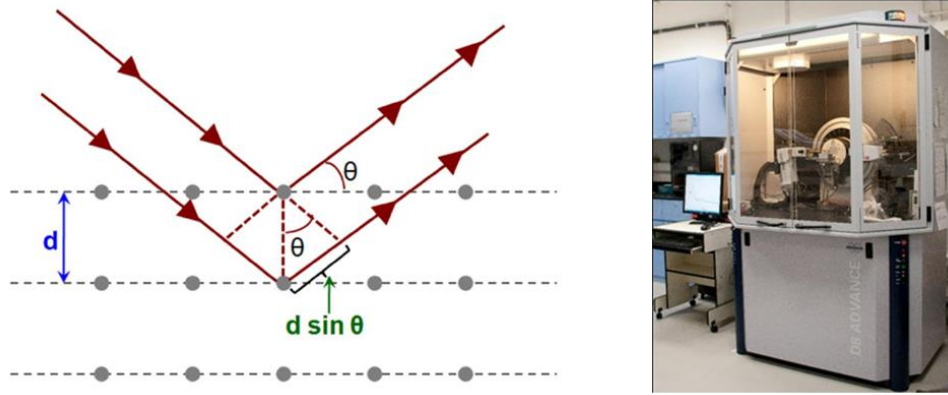


Fig. 2.1: (a) Schematic representation of the Bragg's law. (b) Bruker D8 Advanced Powder X-ray Diffractometer.

To study the nature of crystal imperfection the use of diffraction line profiles is one of the most important application of power diffraction. Earlier studies with XRD line profile of cold work sample implies that plastic deformation induces the shift, asymmetry and broadening of the XRD peak profile. Calculating the shift, asymmetry and broadening of the XRD peak we can easily calculate the stacking fault, twinning fault probability and many other microstructural parameters.

As previously described, that broadening of line profiles of X-ray diffraction mainly controlled by small size of crystallite, microstrain induced inside the crystallites and SFs. Slit widths, size of the experimental sample, imperfect focusing and unresolved  $\alpha_1$  and  $\alpha_2$  peaks etc are some instrumental parameters which are also responsible for extraneous broadening of

the line profile. All these parameters related to the instrument which are responsible for such a broadening of the XRD line profile, named all together as "instrumental broadening". Besides the effect of particle size and microstrain on the line profile, Fourier analysis method was also effectively used to determine stacking and twin faults probability. Scherrer discovered in 1918 that the line breadth of the XRD peak varied inversely with crystallite size, and he suggested a relationship below to measure crystallite size from the X-ray line profile:

$$\beta = \frac{K_s \lambda}{D \cos \theta} \quad (2.2)$$

This equation known as Scherrer formula, where  $\lambda$  is the wavelength of X-ray,  $\theta$  represents the Bragg angle,  $\beta$  is the measure of line breadth,  $K_s$  is Scherrer constant and its range is ( $1.0 > K_s > 0.89$ ) and finally  $D$  represents an apparent crystallite size and its value depends on the direction of  $hkl$  planes, measurements of breadth and the shape of the crystallites. This Eq. (2.2) is actually used in the Scherrer formula to calculate the crystal length in the direction perpendicular to the diffraction planes, and it also says that size broadening is independent of the order of reflection. Important drawback to this formula is that Scherrer totally neglected instrumental effects which also contribute a great role to the broadening. This formula is also completely useless in the case of certain crystals where strain broadening results from atom displacement relative to their mean location. All these drawbacks minimize the application of Scherrer formula to a broad area of sophisticated problem, but still, it has great importance as an initiation of this analysis and also it is useful in some simple cases where line broadening is primarily depends on the crystal size and when its size fairly less than hundred angstroms.

Many earlier observations by various physicist were that the line broadening which arise from microstrain,  $\varepsilon_L$  was found to depend on the order of reflection and Bragg angle and they proposed a relation that:

$$\beta = 4\varepsilon_L \tan \theta \quad (2.3)$$

Microstrain parameter,  $\varepsilon_L$  can be determined by using the above equation. In case of polycrystalline samples, crystallite size shows a noticeable change with grains containing dislocation networks, SFs, twin planes and other faults and in this case peak broadening interpretation is very difficult. Usually, the calculation by Scherrer equation offers very large values of crystallite size of coherently diffracting domains, however Scherrer equation is the first link between distinct microstructural features of materials and their associated Bragg

reflection profiles. Some more advanced techniques to determine various structural and microstructural parameters in the present days is briefly discussed in the following sections.

### 2.2.1 Fourier analysis: determination of coherent domain sizes and r.m.s. strains

Peak-shape analysis by Fourier method using the Warren-Averbach (WA) procedure is a very common and prevailing method to analyze the peak broadening in imperfect crystal due to size and strain. Now if power distribution is expressed as a Fourier series (Warren, 1969) then:

$$P_i(\Delta K) = N \sum_{L=-\alpha}^{+\alpha} A(LK_i) \cos(2\pi L\Delta K) + B(LK_i) \sin(2\pi L\Delta K) \quad (2.4)$$

where,  $N$  approximately constant,  $A$  and  $B$  stand for the cosine and sine Fourier coefficients, respectively, while  $L$  stands for the measurement length in reciprocal space perpendicular to the diffracting planes. In actuality,  $L$  takes the discontinuous value  $n\Delta L$ , where  $n$  is an integer and  $\Delta L$  denotes the length change in the reciprocal space. Above Eq. (2.4) is defined with respect to a parameter  $K_i$  represents distance to the origin in reciprocal space which is directly related to the diffraction angle  $2\theta_i$ , by  $K_i = 2\sin\theta_i/\lambda$ , where  $\lambda$  is the wavelength of the X-ray.  $\Delta K$  is the deviation from  $K_i$  is represented by  $\Delta K = 2(\sin\theta - \sin\theta_i)/\lambda$ . In general,  $2\theta_i$  is chosen as the location of the centroid of the line profile. Any pair of line profile  $P_1$  and  $P_2$  with  $K_2 = 2K_1$  is called a first and second order reflection. As the sine coefficients could not be interpreted physically (Mittemeijer & Delhez, 1978; Ungar *et al.*, 1989) that's why only the cosine Fourier coefficients  $A(LK_i)$  are considered.

### 2.2.2 Conventional Warren-Averbach analysis

X-ray diffraction line profile intensity measured from a structurally imperfect crystal is thought to be a product of the structurally broadened line profile and instrumental line profile. As a result, Fourier coefficients of the measured profile must also be the combination of Fourier coefficient of the structural and instrumental line profiles. A specimen known as a "standard" specimen, devoid of lattice imperfections is used to measure the instrumental line profile. It is now simple to acquire the Fourier coefficients of the structurally broadened line profile if we deconvolute the Fourier coefficients of the line profile of the "standard" specimen and the defective specimen. (Stokes, 1948). In case of unavailability of the standard specimen one can assign the smaller broadening profile as a standard profile for instrumental broadening profile then two broadened profiles can be treated analogously. Thus, resultant Fourier coefficients

show the differences in lattice imperfection (microstrain and crystallite size and) (Keijser & Mittemeijer, 1980).

Fourier cosine coefficients of a line profile which is structurally broadened can be considered as the products order-independent size coefficients  $A^s(L)$  and order-dependent strain coefficients  $A^d(L, K_i)$  (where superscript  $s$  used for size and  $d$  used for distortion). Assuming that the specimen consists of columns that are parallel to the diffraction vector, the size Fourier coefficient  $A^s(L)$  may be ascertained using the column length size distribution function  $\rho(D)$ , where  $D$  represents the column length.  $\langle D \rangle$  is also denoted as the average column length (size). Similarly strain Fourier coefficient  $A^d(L, K_i)$  is determined by the strain distribution function  $\rho(\varepsilon_L)$  where  $\varepsilon_L$  is considered as the average true (local) strain  $\varepsilon_0$  over a length  $L$ . Now if all the distribution are normalized to unit area, then Fourier coefficient and both the size and strain Fourier coefficients can be written as (Warren, 1959):

$$A(L, K_i) = A^s(L) A^d(L, K_i), \quad (2.5)$$

$$A^s(L) = \frac{1}{\langle D \rangle} \int_{|L|}^{\infty} (D - |L|) \rho(D) dD \quad (2.6)$$

$$A^d(L, K_i) = \int_{-\infty}^{\infty} \rho(\varepsilon_L) \cos(2\pi L K_i \varepsilon_L) d\varepsilon_L \quad (2.7)$$

In order get the information on  $A^s(L)$  and  $A^d(L, K_i)$  independently, it is necessary to measure a minimum of two orders of reflections and specify both of them using assumptions on  $\rho(D)$  and  $\rho(\varepsilon_L)$ . The separation step, which comes last, can be completed in a variety of ways with a variety of techniques, but in actuality, one must always select the approach that best suits the specimen being studied.

In WA analysis the  $K_i$  dependence strain Fourier coefficient  $A^d(L, K_i)$  is expressed by Taylor-series expansion taking an approximation of smaller value of  $L$  and  $K_i$  (Warren & Averbach, 1950; van Berkum *et al.*, 1994) as.

$$\ln [A^d(L, K_i)] \cong -2\pi^2 L^2 K_i^2 \langle \varepsilon_L \rangle \cong (K_i/K_1)^2 \ln [A^d(L, K_1)] \quad (2.8)$$

where,  $\langle \varepsilon_L \rangle$  is the mean squared strain. The aforementioned equation is accurate for all values of  $L$  and  $K_i$  if all  $\rho(\varepsilon_L)$  are Gaussian (Warren & Averbach, 1950). Deviation of  $\rho(\varepsilon_L)$  from the Gaussian smaller the range in  $L$  for which Eq. (2.8) to be valid.

Now following the above Warren (Warren & Averbach, 1952) equation and taking the order independence of size Fourier coefficient, WA analysis can be written as:

$$\ln [A(L, K_i)] = \ln [A^s(L) - 2\pi^2 L^2 K_i^2 \langle \varepsilon_L^2 \rangle] \quad (2.9)$$

Now to compare with the other suited separation method applicable, WA analysis looks like the following form:

$$\ln [A(L, K_i)] = \ln [A^s(L) - (K_i/K_1)^2 \ln [A^d(L, K_i)]] \quad (2.10)$$

Now size Fourier coefficients and strain Fourier coefficients of the profile  $\rho_1$  can be easily obtained from the intercept and slop of the plot of  $\ln [A(L, K_i)]$  versus  $(K_i/K_1)^2$  respectively and the mean squared strain  $\langle \varepsilon_L^2 \rangle$  also be calculated from  $A(L, K_i)$  using Eq. (2.8).

### 2.2.3 Modified Williamson-Hall and Warren-Averbach analyses

The scatter in the conventional Williamson-Hall plot is produced mostly by strain anisotropy of elastic constants, which Ungar and colleagues resolve by incorporating dislocation contrast factors ( $\bar{C}_{hkl}$ ) into their analysis for various Bragg reflections ( $hkl$ ). This is the modification of conventional WH plot and commonly known as the modified Williamson-Hall and WA analyses. This was done by making an assumption that microstrain is modelled using the contribution of screw and edge dislocations of a glide system when they are equally populated. The average value of contrast factors ( $\bar{C}_{hkl}$ ) corresponding to different Bragg reflections ( $hkl$ ) were also used for modification of W-A procedure (Ungar *et al.*, 1998; Sahu *et al.*, 2012) known as *modified* W-A. This *modified* W-A procedure was used to calculate the dislocation densities ( $\rho$ ), the effective outer cut-off radius ( $R_e$ ) of dislocations. Effective outer cut-off radius of dislocation actually represents a range in which the dislocation distribution is purely random maintaining a constant density  $\rho$  and no interaction of these dislocation with the outside region. A dimensionless quantity named Wilken's parameter ( $M = R_e \sqrt{\rho}$ ) can also be calculated with the above two determined parameters which indicates the dipole character of dislocation where value lower than 1 represents strong dipole interaction between dislocations and vice versa (Wilken, 1970; Ungar *et al.*, 1998a). Using a pseudo-Voigt function fitting method as described by Enzo *et al.* (1988), the full-width-at-half-maximum (FWHM) of the observed Bragg reflections were obtained and subsequently substituted into the following *conventional* W-H equation (Williamson & Hall, 1953):



$$\Delta K = \frac{0.9}{D} + \Delta K^D \quad (2.11)$$

where,  $\Delta K = \frac{2\cos\theta}{\lambda}\Delta\theta$  is the FWHM in  $\text{nm}^{-1}$  and  $\Delta\theta$  is the FWHM in radian,  $\theta$  and  $\lambda$  denote the Bragg angle and wavelength of the employed X-rays, respectively.  $D$  considered as the volume averaged crystallite size or coherently diffracting domains size, while  $\Delta K^D$  represents the strain contribution to X-ray peak broadening. Then the concept of dislocation contrast factors was introduced through the following *modified* W-H equation (Ungár *et al.*, 1998, 1999 & 2001):

$$\Delta K = \frac{0.9}{D} + \left(\frac{\pi M^2 b^2}{2}\right)^{1/2} \rho^{1/2} K \bar{C}_{hkl}^{1/2} + O(K^2 \bar{C}_{hkl}) \quad (2.12)$$

The magnitudes of the Burgers vector and dislocation density are represented by  $b$  and  $\rho$ , respectively, while  $O$  stands for non-interpreted higher order terms in  $K^2 \bar{C}_{hkl}$ . Neglecting the higher order terms and then squaring Eq. (2.12), the following equation is obtained:

$$[(\Delta K^2) - \alpha]/K^2 = \beta \bar{C}_{hkl} \quad (2.13)$$

where,  $\alpha = \left(\frac{0.9}{D}\right)^2$  and  $\beta = \frac{\pi M^2 b^2 \rho}{2}$ . In cubic crystals, the average contrast factors of dislocations,  $\bar{C}_{hkl}$ , corresponding to the Bragg reflections ( $hkl$ ) are related to the average contrast factor for  $h00$  type of Bragg reflection by the following relation (Ungar *et al.*, 1999):

$$\bar{C}_{hkl} = \bar{C}_{h00}(1 - qH^2) \quad (2.14)$$

where,  $\bar{C}_{h00}$  is obtained from the elastic constants of the crystal, while  $q$  controls the screw or edge character of dislocations and  $H^2$  is defined as:

$$H^2 = \frac{(h^2 k^2 + k^2 l^2 + l^2 h^2)}{(h^2 + k^2 + l^2)^2} \quad (2.15)$$

Using Eq. (2.14) in Eq. (2.13), Eq. (2.12) for modified W-H plot further reduces to:

$$[(\Delta K^2) - \alpha]/K^2 = \beta \bar{C}_{h00}(1 - qH^2) \quad (2.16)$$

Now if  $[(\Delta K^2) - \alpha]/K^2$  plotted with  $H^2$  according to Eq. (2.16), then the parameter  $q$  is given by the reciprocal of the intercept of  $H^2$  axis (X-axis). Reported values  $q$  in austenite by Ungar *et al.* (1999) for pure edge and screw dislocations respectively are 1.71 and 2.46. The calculated values of the dislocation character parameter ( $q$ ) are then utilised to calculate the fractions of

edge and screw dislocations in the deformed microstructure using the equation below (Garabagh *et al.*, 2008):

$$f_{\gamma(edge)} = \frac{(2.46 - q_{\gamma})}{(2.46 - 1.71)} \quad (2.17)$$

$$f_{\gamma(screw)} = 1 - f_{\gamma(edge)} \quad (2.18)$$

where,  $f_{\gamma(edge)}$  and  $f_{\gamma(screw)}$  are the fraction of the edge and screw dislocations, respectively.

The computed  $\bar{C}_{hkl}$ 's values according Eq. (2.14) were then used in the following *modified* W-A equation (Ungar *et al.*, 1998a):

$$\ln A(L) \cong \ln A^s(L) - \rho \frac{\pi b^2}{2} L^2 \ln \left( \frac{R_e}{L} \right) (K^2 \bar{C}_{hkl}) + Q(K^4 \bar{C}_{hkl}^2) \quad (2.19)$$

where,  $A^s(L)$  are the size Fourier coefficients of the peak profile,  $L$  is the Fourier variable. Neglecting the higher order terms of  $K^2 \bar{C}_{hkl}$  in Eq. (2.19),  $\ln A(L)$  now becomes a function of  $K^2 \bar{C}_{hkl}$ . Consequently, it was possible to visualise the real component of the Fourier coefficients that were obtained by fitting the observed Bragg reflections over a range of  $L$  values. The slope ( $Y$ ) of these coefficients in the linear area may be roughly expressed as  $\rho \frac{\pi b^2}{2} L^2 \ln \left( \frac{R_e}{L} \right)$ . Further rearrangement of the slope in Eq. (2.19) directly leads to:

$$\frac{Y(L)}{L^2} = \rho \frac{\pi b^2}{2} \ln(R_e) - \rho \frac{\pi b^2}{2} \ln(L) \quad (2.20)$$

Eq. (2.20) thus represents a  $y = mx + c$  like linear relationship between  $\frac{Y(L)}{L^2}$  and  $\ln(L)$ , wherein ( $\rho$ ) and ( $R_e$ ) could be directly evaluated from the slope and intercept of Eq. (2.20), respectively.

#### 2.2.4 Consideration of planar faults

X-ray diffraction is considered to be a powerful device when we try to study how SFs affect the microstructure of a deformed material. Barrett (1952) first suggested that the XRD pattern of the deformed sample is changed by the formation of SFs in the close-packed fcc metals as a result of cold working. According to Paterson (1952), deformation and stacking fault produces symmetrical broadening or peak shift in fcc metals or alloys while twin or growth faults introduces asymmetry in the broadening of the XRD line profile. Among the various methods

to deal with the SF problem, Wilson first used the difference equations method in 1942 then followed by Paterson in 1952. Difference equation method generally express the probability of  $m^{\text{th}}$  neighbour layer which can be same or different from the original layer. Difference equation which is formed by considering the combined effect of growth and deformation faults was deduced by Gevers (1954a) and the simplified form this equation was generated by Warren by making an assumption of sufficiently small value of probabilities for both the faults of fcc structure.

The peak position shift, peak asymmetry and peak broadening effects which are mainly controlled by SFs and twinning gives two important parameters i.e. stacking fault SFs ( $P_{sf}$ ) and twin fault probability ( $P_{tw}$ ). These two parameters can be individually calculated from each of these factors as described below:

SFs, lattice parameter ( $\Delta a/a_0$ ) change and long-range residual stress are the different deformation effect which combinedly affect the peak position of a X-ray diffraction profile and made a shift to the peak of cold worked material with respect to its annealed specimen. Considering very small value of residual stress term with respect to stacking fault term in cold-worked sample and neglecting it the entire peak shift can be written as

$$\delta(\Delta 2\theta)_{hkl-h'k'l'} = A_{hkl-h'k'l'}(\Delta a/a_0) + H_{hkl-h'k'l'}(\alpha' - \alpha'') \quad (2.21)$$

$$A_{hkl-h'k'l'} = (-360/\pi)(\tan \theta_{hkl} - \tan \theta_{h'k'l'}) \quad (2.22)$$

$$H_{hkl-h'k'l'} = (-360/\pi)(G_{hkl} \tan \theta_{hkl} - G_{h'k'l'} \tan \theta_{h'k'l'}) \quad (2.23)$$

Here,  $\alpha'$ ,  $\alpha''$  are the intrinsic and extrinsic stacking fault probability,  $a_0$  refers to the lattice parameter of annealed specimens and  $H$  depends only on the reflecting planes through faulting co-efficient,  $G$ 's. Using the above equations, we can directly determine the value of intrinsic and extrinsic stacking fault probability.

In absence of an annealed specimen another novel approach is existed for determining the values of  $P_{sf}$  which is used by several researchers to calculate  $P_{sf}$  in different austenitic steels (Tolonen & hanninen, 2007; Huang *et al.*, 2008). This innovative method uses the Warren treatment (Warren, 1969) in conjunction with Bragg's rule to compute the angular location of the faulted austenite diffraction lines as:

$$2\theta_{hkl} = 2\arcsin\left(\frac{\lambda}{2d_{hkl}}\right) + \frac{90\sqrt{3} P_{sf} \tan\theta_{hkl}}{\pi^2 h_0^2 (u+b)} \sum(\pm) L_0 \quad (2.24)$$

where,  $\theta_{hkl}$  is the angular position of austenite corresponding to  $(hkl)$  reflection plane,  $\frac{1}{\pi^2 h_0^2 (u+b)} \sum(\pm) L_0$  is a constant for a particular austenite  $(hkl)$  reflection and their values corresponding to each reflection plane are available in the literature (Warren, 1969).  $d_{hkl} = \frac{a}{\sqrt{h^2 + k^2 + l^2}}$  is the interplanar spacing of fault  $(hkl)$  plane, where  $a$  is the lattice parameter of the austenite and  $\lambda$  is wavelength of X-ray used. For each Bragg reflection a set of linear equations are obtained from the above equation which are used to determine the  $P_{sf}$  via regression analysis. Due to insignificant effect of long-range residual stress on the peak shift of the diffraction line its contribution was assumed to be zero in Eq. (2.24).

## 2.3 Transmission electron microscopy

Among the direct methods TEM is the most important technique for the microstructural characterization of materials which is widely used for imaging crystal defects namely, dislocations, SFs, twin, grain boundaries and voids. This direct observation method, helps to identification the location of the defects, determine its nature and configuration, etc. For all crystal defects the imaging principle and underlying contrast formation mechanism are the same, which essentially utilises the influence of their strain fields on electron scattering. Different modes of imaging of dislocations in TEM is presented briefly in the next sections.

### 2.3.1 Contrast formation in transmission electron microscope

Depending on the contrast mechanism involved in the image generation, image production on TEM may be categorised into two distinct modes: phase contrast and diffraction contrast. A high-resolution TEM (HRTEM) image is created using the phase contrast technique, which involves imaging end-on columns of atoms parallel to the electron beam. HRTEM is able to photograph the dislocation's missing planes and core structure directly. It can even distinguish between planes that are spaced as little as 0.2 nm apart (Li, 2009). However, HRTEM can only be used for a restricted set of issues since dislocation imaging can only be done in cases when the dislocation line is parallel to the electron beam, straight, and has a constant core length (Li, 2009; William & Carter, 2009). As a result, the study of dislocations with HRTEM is generally limited to planar core structures of dislocations, as in the case of covalent crystals, and the use of HRTEM for metallic materials remains quite limited.

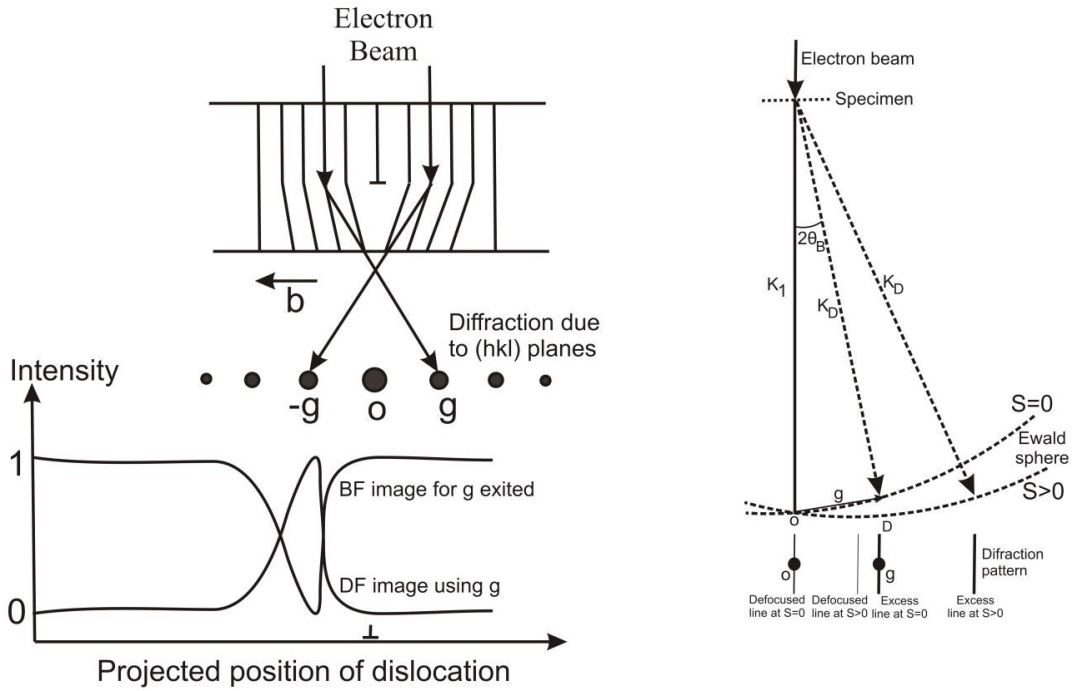


Fig. 2.2: Schematic diagram showing deformed planes near the dislocation centre that diffract into  $\vec{g}$  and  $-\vec{g}$ . This condition is obtained by tilting the specimen slightly away from the Bragg condition  $s = 0$  in order to put deformed planes near the core into the precise Bragg condition  $s = 0$ . The dislocation contrast intensity profiles that are shifted from their anticipated position when photographed with  $-\vec{g}$  reflection are shown in the lower diagram. (b) Ewald sphere geometry for two beam diffraction condition with  $s = 0$  and  $s < 0$ . The lines depicted are Kikuchi lines, which result from electrons that are inelastically scattered (William & Carter, 2009). A pair of Kikuchi lines consists of a “excess” and a “deficient” line. These lines facilitate the Bragg's condition setup. When  $s > 0$  Kikuchi lines are on the same of side of as  $\vec{g}$  as O; they are on the opposite side of  $\vec{g}$  when  $s < 0$ .

The effect of strain fields in Bragg diffraction condition is used for diffraction contrast imaging of dislocations. Atomic planes are bent by dislocation in a lattice, especially in areas near the core. To facilitate imaging, the specimen must initially be tilted into a two-beam condition, which excites a strong diffraction vector  $\vec{g}$  from just a specified set of  $hkl$  planes apart from the direct (transmitted) beam. As seen in Fig. 2.2, it is then tilted away somewhat from the precise Bragg condition (i.e., with some excitation error or deviation,  $s > 0$ ) so that deformed planes close to the dislocation core are brought into the Bragg condition while areas far from the dislocation core are tilted away. Because of size effects, the Bragg peak may broaden or streak from regions that are not exactly at the Bragg condition, leaving some scattered intensity visible. The contrast of dislocation image is determined by the dot product

of vector  $\vec{g}$  and vector  $\vec{R}$  ( $\vec{g} \cdot \vec{R}$ ) where  $\vec{R}$  is considered to be the lattice distortion vector. An examination of the  $\vec{g} \cdot \vec{b}$  condition is a crucial parameter to monitor the contrast condition of dislocations, as  $\vec{R}$  is directly proportional to  $\vec{b}$  for a pure screw dislocation. Screw dislocations when  $\vec{g} \cdot \vec{b} = 0$  result in no strain contrast because the diffracting planes are parallel to  $\vec{R}$ . This condition for diffraction contrast imaging is referred to as the “invisibility” criteria for dislocations. The requirement  $\vec{g} \cdot \vec{b} \times \vec{u} = 0$  where  $\vec{u}$  is the line direction, must also be met for edge dislocations since the displacement field of an edge dislocation causes the glide planes to buckle. Images created in TEM by diffraction contrast are asymmetric, with the position of the diffracted intensity contrast relative to the core determined by the signs and deviations  $\vec{g}$ ,  $\vec{b}$  and  $s$ . When either of these parameters is reversed, the contrast throughout the core alters.

Depending on whether a transmitted beam or a diffracted beam is utilised to create the image, two distinct techniques of imaging the dislocations in a TEM are known as bright field (BF) and dark field (DF). Dislocation appears in dark contrast on a bright background when operating in the BF mode, and in bright contrast on a dark background when operating in the DF mode. The dislocation contrast is caused only by the operating diffraction vector and the area where the  $hkl$  planes satisfy the Bragg condition appears as dark/bright in the BF/DF images. The character of dislocations (i.e. edge, screw or mixed type) their Burgers vector and the glide plane direction can be identified by TEM analysis. Diffraction contrast imaging is also used to identify other distinct feature types, such as jogs or kinks, and the interactions between dislocations and lattice defects. Diffraction contrast imaging has a role to reveal the existence of unusual defects like faulted dipoles, and multipoles and SF tetrahedron, (William & Carter, 2009).

When dealing with elastically anisotropic materials, dynamic scattering of the intense diffracted beam might obstruct the route of the diffraction contrast of the dislocation imaging, which restricts the interpretation and analysis of closely spaced dislocations for super dislocations of inter-metallics. In this situation computer simulation of dislocation contrast is needed to interpret the experimentally observed diffraction contrast of dislocation. We know that the mathematical formula for the invisibility criteria is the dot product of  $\vec{g}$  and  $\vec{b}$  (i.e.,  $\vec{g} \cdot \vec{b}$ ) fulfilled by dislocations with a Burgers vector  $\vec{b}$  would likewise be satisfied by dislocations with a Burgers vector an integral multiple of  $\vec{b}$ . As the Burgers vectors of perfect dislocation in ordered phases are integral multiples of the Burgers vectors in the corresponding

disordered phase therefore, it is impossible to determine explicitly the magnitude of the Burgers vector of dislocations in ordered phases using of invisibility criterion alone. In this case, the computer simulation of dislocation images (Singh *et al.*, 1988) also used to determine the magnitude of Burgers vector.

Diffraction contrast imaging is very effective for studying in-situ deformation, where a notion of dislocation response is important to understand the evolution of dislocation structure. Here, tensile samples with gauge lengths of less than 3 mm are strained under a microscope to watch the multiplication processes during plastic deformation as well as the real-time phenomena of dislocation motions and interactions with other defects. To study the micro-processes that control the dislocation mobility, in-situ experiments are the powerful method. This technique also useful for direct measurement of mobile dislocation density, kinetics of movements or events, measurement of activation volume etc. Metastable core configurations which exist only when the stress is applied are possible to be observed by this useful technique. Finally, this is the unique method for directly seeing the phenomenon of dislocations overcoming barriers like interfaces and precipitates.

### 2.3.2 Weak Beam Transmission Electron Microscopy

The Weak Beam (WB) Technique is a specific type of Diffraction Contrast Imaging in Transmission Electron Microscopy that uses weakly stimulated reflections to image dislocations. The reason why this technique is called WB is because the intensity of the diffraction point used for imaging is weak when averaged over region. The WB condition requirement is achieved if the crystal orientation is adjusted so that its placement in the two beam condition moves away from the Bragg condition (*i.e.*  $s > 0$ ). The specimen is tilted to a 3g WB condition to fulfil the diffraction condition of this criterion is shown schematically in Fig. 2.3.

Setting  $\vec{g}$  vector in this condition in the DF imaging the dislocations are imaged as bright and sharp lines where negligible intensity in the neighbour region. Prior to tilting the specimen, a standard two-beam condition must be established in order to acquire WB imaging. As the specimen tilted, deviation as well as  $s$  increases and the average intensity decreases at a rate of  $\frac{1}{s^2}$  as a result diffraction beam appears as a weak spot (William & Carter, 2009). Large value of  $s$  produce a smaller value of the excitation which subsequently form sharp and narrow images of dislocations. In contrast to traditional DF imaging, dislocations observed under WB

have well-defined positions in relation to their cores. The smallest volume of crystal (locally arranged in Bragg orientation) that results in constructive interference limits the resolution in the WB condition (William & Carter, 2009). The minimum separation between the Dislocation pairs can be resolved by using WB imaging as  $\sim 1.5$  nm (Veyssier, 1991).

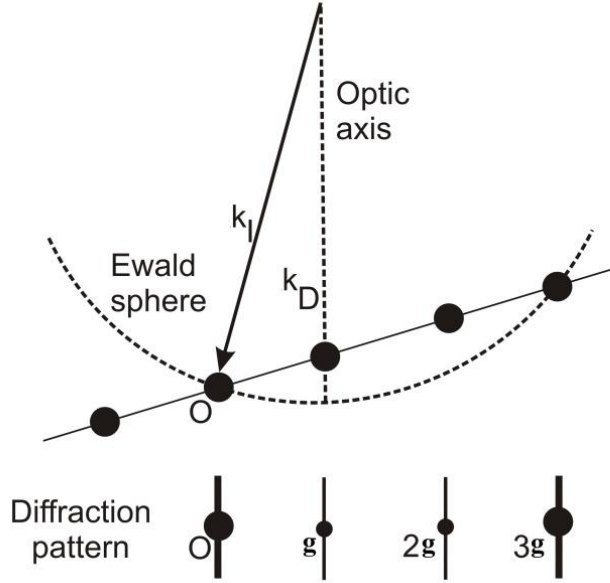


Fig. 2.3: Ewald sphere and positions of Kikuchi lines for the diffraction conditions. (William & Carter, 2009).

In intermetallic alloys dislocation pairs separated by very small distance (of the order of nm) and for this type finely separated dislocation WB technique is mostly useful technique. Additional benefits of WB imaging over DF imaging include its less sensitivity to foil thickness and dislocation positions within the sample. WB technique has lower uncertainties in elastically anisotropic crystals compared to DF. Dislocation characterization by WB technique has become popular in intermetallic metal as fine structures of dislocations can be resolved easily by this technique in ordered structure.

Estimation of deformation mechanism by TEM analysis of a bulk material may create the doubt of its reliability as the maximum volume of a sample characterized by TEM is only about  $10^{-5}$  mm<sup>3</sup>. Veyssier (1991) predict that a rough estimation of the defect density can be made by TEM analysis. Considering that a sample deformed to a permanent strain of 1% has a dislocation density of approximately  $10^9$  cm<sup>-2</sup>, this suggests that only a few centimetres of the dislocation length can be examined in order to characterise the entire deformation process.



Of these, only a small fraction of the dislocations (such as the slip plane and Burgers vector dislocation reaction) can be analysed. In spite of this limitation microstructure investigation of the bulk specimen by TEM is found to be reasonably consistent with the of different experimental, theoretical and computational techniques.

The most comprehensive examination of the dislocation and deformation behaviour is offered by TEM, which is the sole instrument capable of identifying unique slip systems and deformation mechanisms for several alloy systems that are undergoing development for use in high-temperature structural applications. No other technique can match its level for imaging capacities while for the case of larger volume specimen sampling others techniques may takes its place as well.

## **2.4 Electron Backscatter Diffraction**

Electron Backscatter Diffraction (EBSD) is a scanning electron microscope (SEM) based analysis technique to obtain crystallographic orientation with sub-micron spatial resolution as well as phase information of the material. The TEM-obtained Kikuchi diffraction patterns are the fundamental basis for the EBSD image (Nishikawa & Kikuchi, 1928a, 1928b; Joy & Booker, 1971; Venables & Harland, 1973; Dingley, 1984). The Hough transform is then introduced to interpret the obtained images (Schmidt *et al.*, 1991; Lassen *et al.*, 1992; Lassen, 1996). The formation of Kikuchi bands, also known as "EBSPs" (electron backscatter patterns), occurs when accelerated electrons in the SEM's main beam diffract by atomic layers in crystalline materials. The diffracted electrons then strike on a phosphor screen, producing lines that are visible. These visible lines called the Kikuchi bands. The patterns that emerge on the screen are essentially projections of the crystal's lattice planes, which provide direct insight into the grain's crystalline structure and crystallographic orientation. The data may be utilised to perform fabric analyses on polycrystalline aggregates and identify phases based on crystal structure when combined with a data base that contains crystallographic structure information for phases of interest and software for processing the EPSPs and indexing the lines.

A well-polished and highly flat crystalline specimen is first placed in the SEM chamber for EBSD imaging. The polished sample is positioned such that it leans towards the electron beam's normal incidence by about 70 degrees and the electron beam then strikes the sample at a grazing angle of about 20 degrees (Fig. 2.4). For diffraction, electron beam must be accelerated with an acceleration voltage of 10-30 kV by using an incident current of 1-50 nA.

The EBSD pattern resulted from diffraction of a divergent source of electrons generated within the sample just below the point where the primary beam of electrons strikes the specimen.

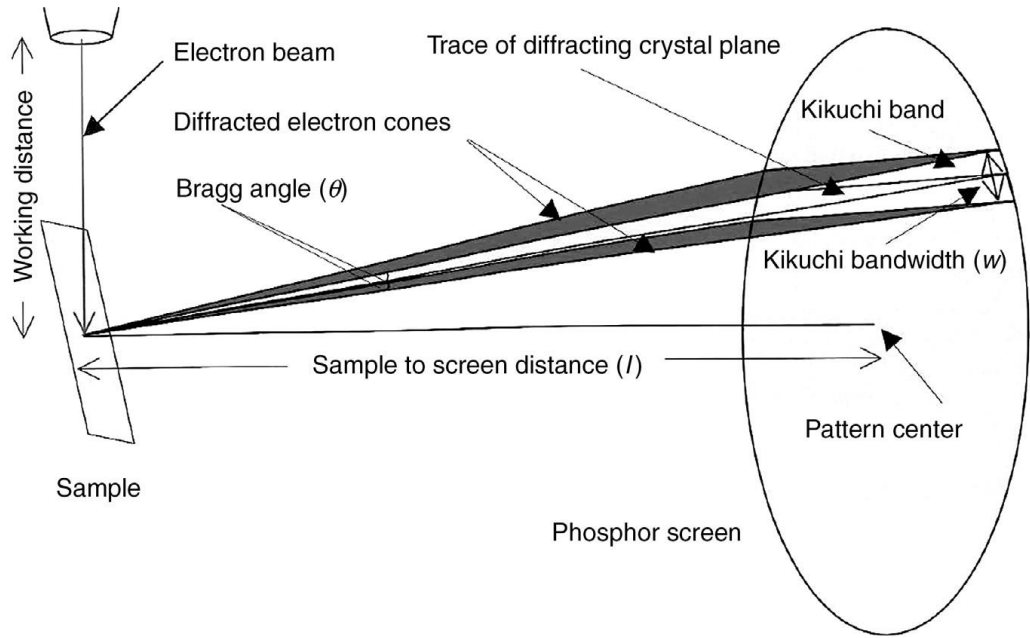


Fig. 2.4: Detection setup for Electron backscatter diffraction (EBSD). (Pereira-da-Silva & Ferri,2017).

The detector is actually a charge-coupled device (CCD)-type camera equipped where phosphor screen is embedded with a digital frame grabber. The camera is positioned on a motorised carriage that is placed horizontally and is inserted up to a few millimetres below the surface of the incline sample. The ideal arrangement condition is reached when the camera approaches the sample as closely as feasible without causing a collision between the sample surface and the fragile phosphor screen. A diffraction pattern along the direction of the diffracted electrons may now be seen if the phosphorous screen is positioned extremely near to the sample (Wells, 1999). The diffracted electrons are converted into photons by the phosphorous screen, which turns the backscattered signal into light. This transformed light directly enters into the CCD camera and gets detected. Now the detected image of EBSD by the CCD camera is recorded for further operation and also analysed to get different information about the phase, crystal orientation etc. The EBSD images affected by crystal’s spatial

orientation in the sample, separation between the sample and the phosphorous screen and the wavelength of the incident electron beam.

To identify each unique Kikuchi line in the spectrum, the pattern of Kikuchi lines shown on the phosphor screen is electronically digitised and processed. The areas of the specimen where low density of defects is seen and/or where half of the beam can penetrate, or thicker than that, then Kikuchi lines are best seen for those areas of the specimen. Only spots become visible when the specimen is thinner but when specimens is very thick then Kikuchi lines are formed. Hough space is used to identify the Kikuchi bands where the brightest peaks represent the location of the more intense Kikuchi bands (Fig. 2.5) and the other peaks are indistinct and almost unnoticeable. According to the peak detection algorithm, most intense peaks are

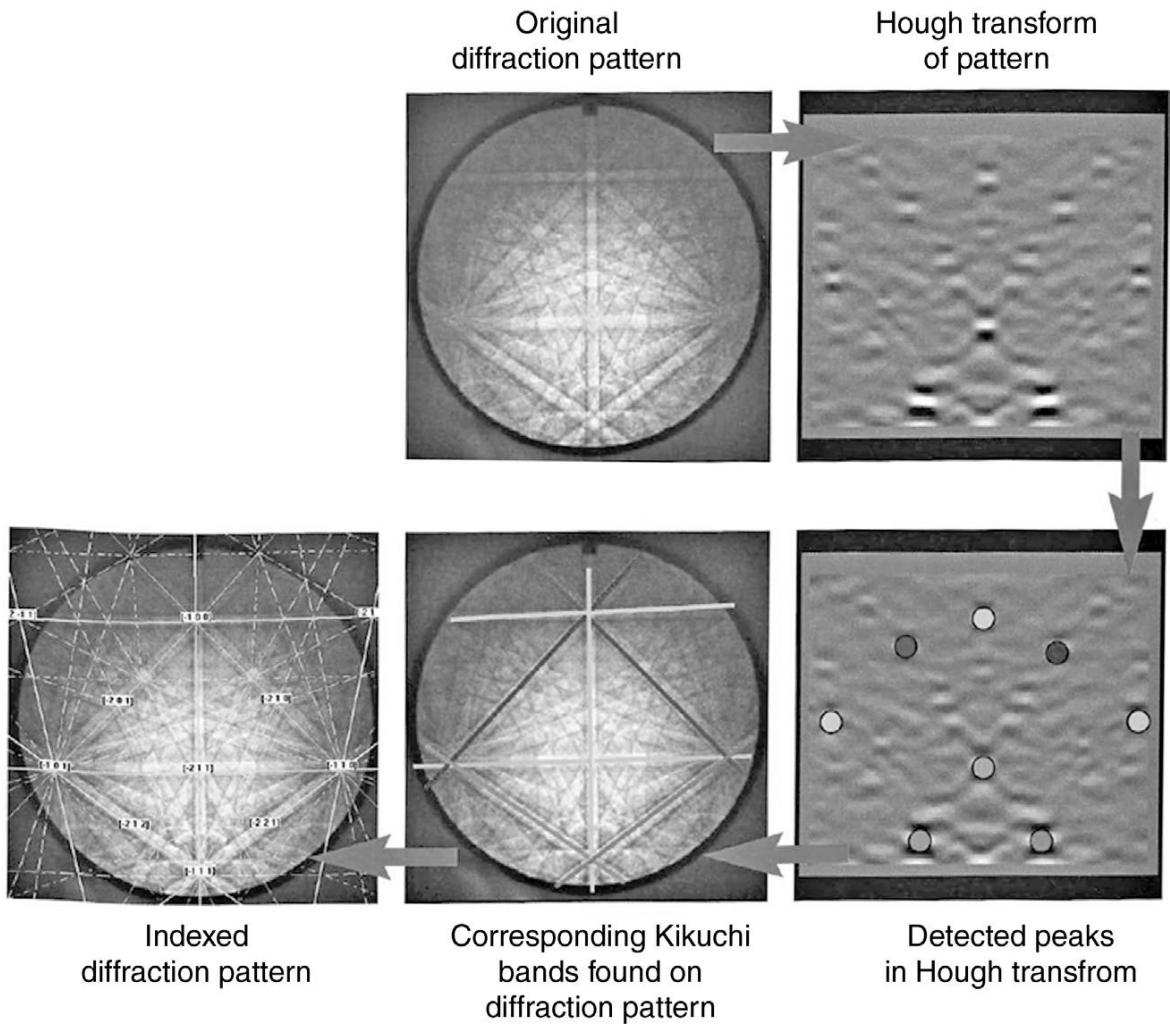


Fig. 2.5: EBSD order to acquire structural properties. The initial diffraction pattern, the Hough transformed pattern, the peaks obtained during the Hough transformation, the associated Kikuchi bands discovered inside the diffraction pattern, and the indexed diffraction patterns are all included in this sequence. (Pereira-da-Silva & Ferri,2017).

analysed (Fig. 2.5) and the very low intense ultrafine false peaks are disregarded. A line matching to each peak in the preceding image is placed on the original image of the Kikuchi diffraction pattern to analyse the findings. The superimposed lines and peaks are coded after considering the connection with each point or set of points. Now for structural characterization, points with the same structural features are identified then a map is generated. EBSD data may be utilised for many different things, such as figuring out the crystal's orientation, indexing the pattern, and identifying the phase of the crystal. In addition to performing statistical analysis of the sample's microfabric, EBSD research is utilised to determine the relative abundance of each phase in a polyphase sample as well as to pinpoint the systematic textural relationship between individual grains or phases. All symmetric phases (even isotropic phases) and opaque phases data are possible to obtain by the EBSD analysis. This data delivers a true 3-dimensional orientations of the individual crystals where the spatial resolution is of few microns.

## 2.5 Estimation of experimental stacking fault energy

Experimental determination of SFE was done by Schramm & Reed method (1975) later modified by Dey *et al.* (2005) adopting the X-ray diffraction line profile analyses where they consider the effect of dislocation parameters on SFE. Due to overgeneralized assumptions and indirect nature of estimation this method often criticised though this can yield SFE values with higher statistics. Besides this approach, there are other two approaches available based on WBDF imaging in TEM. One approach through the measuring the radii of isolated extended nodes (Ruff (1970) and the another one is extension width method based on the calculating the extension widths of  $\frac{a}{2}\langle 111 \rangle$  glide dislocations (Brown & Thölen, 1964; Ray & Cockayne, 1971). There is no doubt that TEM approach is direct in nature to estimate the SFE, yet some shortcoming cannot be neglected that it offers extremely low statistics and this method is extremely restricted to early deformation stages. Thus, keeping in mind the merits and demerits of TEM and X-ray diffraction and accepting the practical challenge to measure SFE experimentally, these methods should be used concomitantly for reliability of the results. The underlying principles of each method are outlined below.

### 2.5.1 X-ray diffraction approach

Stacking fault energy measurement using the X-ray diffraction analysis by Schramm and Reed (1975) method was done by calculating the mean square microstrain  $\langle \epsilon_L^2 \rangle$  of the deformed austenite and the stacking fault probability ( $P_{sf}$ ). Mean square microstrain  $\langle \epsilon_L^2 \rangle$  was determined

along  $\langle 111 \rangle$  direction taking average over the distance of Fourier variable (coherence length),  $L = 50 \text{ \AA}$ . As the microstrain distribution and the effects of austenite dislocation density in the microstructure are not considered to develop the formula of SFE determination, therefore, this approach could be considered as a very oversimplified approach predicted by Dey *et al.* (2005). Microstrain broadening depends on the orientation of the crystal for low SFE material and according to Wilkens (1970) the reason of this dependency is the strain field anisotropy of the crystal which is induced by the contrast factor of dislocations. Hence dislocation related proper correction terms i.e., dislocation contrast factor, dislocation density and its arrangement need to be included for appropriate determination of SFE by X-ray analyses (Dey *et al.*, 2005).

From the above explanation, it is evident that to calculate the accurate SFE, estimation of the dislocation parameters is very fundamental. Considering the idea of variation of the strain field within the dislocation core and the dependency of dislocation contrast factor on the strain broadening, Wilkens improved Krivoglaz (1969) idea by introducing an assumption that parallel screw dislocations distributed randomly within a certain region bounded by effective outer cut off radius ( $R_e$ ). It has been demonstrated that, in the presence of dislocation-induced strain broadening, the change of the strain field within the dislocation core may be characterised by the Wilkens strain function, denoted by (Wilkens, 1970):

$$\langle \epsilon_L^2 \rangle = \rho \bar{C}_{hkl} \pi \left( \frac{b}{2\pi} \right)^2 \ln \left( \frac{R_e}{L} \right) \quad (2.25)$$

where,  $\vec{b}$  is the magnitude of Burgers vector of  $\frac{a}{2} \langle 110 \rangle$  perfect dislocations estimated from the Rietveld analysis,  $\rho$  is the dislocation density and  $R_e$  refers to the effective outer cut-off radius of the dislocations indicating the range over which the dislocations remain randomly distributed and finally  $\bar{C}_{hkl}$  considered as the average contrast factors for the different Bragg reflections ( $hkl$ ). The parameters required for the above calculation may be acquired directly from the graphical plots of the modified Warren-Averbach equation and modified Williamson-Hall equation, as described by Eq. (2.20). Now considering these effect, new modified expression for SFE in terms of dislocation density and dislocation arrangement parameters is given as (Dey *et al.*, 2005):

$$\gamma = \frac{K_{111} \omega_0 G a A^{-0.37}}{\sqrt{3} \pi P_{sf}} \left\{ \left( \frac{b}{2\pi} \right)^2 (\rho \bar{C}_{111} \pi) \ln \left( \frac{R_e}{L} \right) \right\} \quad (2.26)$$

where,  $G$  is the shear modulus of the steel its value considered as  $\approx 72$  GPa,  $A \approx 3.43$  represents as anisotropy factor which is directly connected to the X-ray elastic constants and its value determined according to Pierce *et al.* (2014),  $K_{111}\omega_0$  is actually a proportionality constant with a value of 6.6 (Martin *et al.*, 2016) and  $\bar{C}_{111}$  referred to the average contrast factor of dislocations for the austenite (111) Bragg reflection. It is to be noted that the SFE determined by the above Eq. (2.26) of a deformed specimen essentially gives the effective SFE instead of ideal SFE. When all other faults are taken into account, the ideal and effective SFEs of a real crystal are connected as follows (Müllner & Ferreira, 1996):

$$\gamma_{eff} = \gamma_{\infty} + \frac{\partial E_{str}}{\partial A} \quad (2.27)$$

where,  $\gamma_{eff}$  and  $\gamma_{\infty}$  are considered here as the effective and ideal SFEs respectively and  $\frac{\partial E_{str}}{\partial A}$  refers to the change of elastic coherency strain energy per unit area of the SF. However, this idea accepts that the coherency strain energy is conserved in volume where Olson & Cohen (1976) assume that elastic coherency strain energy comprises of two components as:

$$E_{str} = E_{dil} + E_{sh} \quad (2.28)$$

where,  $E_{str}$  is the dilatation energy which occurs due to volumetric strain arises with the volume change during  $\gamma_{eff} \rightarrow \varepsilon_{hcp}$  martensitic transformation and  $E_{sh}$  is the shear energy related to the shear strain components. The deformation conditions in the present study do not show the significant  $\gamma_{eff} \rightarrow \varepsilon_{hcp}$  transformation hence for the experimental estimation of SFE in austenite Mullner & Ferreira (1996) approach was adapted here.

### 2.5.2 Transmission electron microscopy approach

Brown and Thölen (1964) presented the extended node technique of SFE calculation, which takes into account the equilibrium form of a symmetrical extended node according to isotropic elasticity. In this method, a dislocation's self-stress is described so that it may be computed at the dislocation core using line integrals over the dislocation. Using an iterative process, the form of extended nodes is computed by gradually dislocating points on the dislocation core until the entire load on them (self-stress plus stress from SF and other partials) is eliminated. There is always a discrepancy between the nodes formed by screw and edge dislocations since it is discovered in an isotropic media that the self-stress due to curved screw dislocations can be substantially larger than the self-stress due to curved edge dislocations. The kind of partials

either edge-type or screw-type determines the connection between the SFE and the radius of curvature of the partials in the node. If we believe that the curvature of the partials rather than the nature of the dislocations explicitly determines the width of the node, then SFE may be roughly determined by merely measuring the width of the node using the following equations that they provided with tolerable accuracy.

$$\frac{\gamma_{eff} \times R_1}{G b_p^2} = 0.27 - 0.08 \left( \frac{v}{1-v} \right) \cos 2\alpha'' + \left\{ 0.104 \left( \frac{2-v}{1-v} \right) + 0.24 \left( \frac{v}{1-v} \right) \cos 2\alpha'' \right\} \log_{10} \frac{R_1}{e} \quad (2.29)$$

$$\frac{\gamma_{eff} \times R_2}{G b_p^2} = 0.055 \left( \frac{2-v}{1-v} \right) - 0.06 \left( \frac{v}{1-v^2} \right) \cos 2\alpha'' + \left\{ 0.018 \left( \frac{2-v}{1-v} \right) + 0.036 \left( \frac{v}{1-v} \right) \cos 2\alpha'' \right\} \log_{10} \frac{R_2}{e} \quad (2.30)$$

Where,  $G$  refers to the shear modulus,  $v$  is the Poisson's ratio,  $\vec{b}_p$  is considered as Burger's vector of the partial dislocation,  $e$  refers to the vector normal to the dislocation line and related to Burger's vector,  $R_1$  and  $R_2$  are defined in Fig.2.6,  $\alpha''$  denotes the character of the partials at points L, M and N in Fig. 2.6.

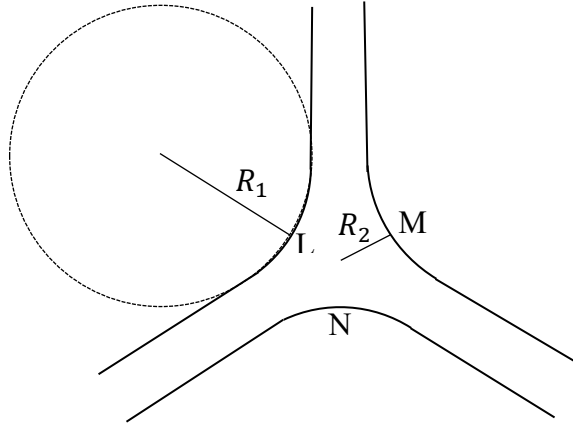


Fig. 2.6: An extended three-fold node and the parameters used to determine SFE according to Eqs. (2.29) and (2.30).

In the extension width approach, the equilibrium configuration of dissociated dislocations requires that the attractive force brought on by an increase in the area of the SF balance out the repulsive elastic force between the partial dislocations. The following equation may be used to calculate SFE under equilibrium conditions if experimental separation values are used and fit with the theoretical curves proposed by Hirth & Lothe in 1982 using an approximation of anisotropic dislocation theory:

$$\gamma = \frac{G b_p^2}{8\pi x_{eq}(1-v)} (2 - v - 2v \cos 2\alpha'') \quad (2.31)$$

where,  $\vec{b}_p$  refers to the Burgers vector of the Shockley partial dislocations (SPD), calculated from the austenite lattice parameters,  $x_{eq}$  is the separation distance of the partial dislocation pairs at equilibrium configuration,  $\nu$  is the Poisson's ratio of the studied steel and  $\alpha''$  is the angle between the perfect dislocation line and Burgers vector. Since Teutonico (1967) asserted that anisotropic and isotropic theories offer a satisfactory level of agreement on the dislocations' extension width for  $\frac{a}{2}\langle 110 \rangle$  dislocations gliding on  $\{111\}$  planes in fcc materials, the isotropic theory of elasticity was approximated in the current dissertation. The measuring of the angle between the Burgers vector of the perfect dislocation and the dislocation line on the g-3g WBDF micrographs is made possible by the detection of both partial dislocations under weak  $\langle 220 \rangle$  reflection (Kim *et al.*, 2011). In order to avoid the constrictions-affected areas, many measurements must be taken along the length of straight, parallel portions of isolated dislocations.

## References

- D.A. & Karjalainen, L.P. (2014). *Metall. Mater. Trans. A*. **45**, 1937-1952.
- Barret, C. S. (1952). *Imperfections in nearly perfect crystal*, Chap. III, John. Wiley, New York.
- Brown, L. M. & Thölen, A. R. (1964). *Disc. Faraday Soc.* **38**, 35-41.
- Bryne, J.G. (1965). *Recovery Recrystallization and Grain Growth*, McMillan CO, NY.
- Dey, S. N., Chatterjee, P. & Sen Gupta, S. P. (2005). *Acta. Mater.* **53**, 4635-4642.
- Dingley, D. J. (1984) *Scanning Electron Microscopy* **2**, 569-575.
- Enzo, S., Fagherazzi, G. Benedetti, A. & Polizzi, S. (1988) *J. Appl. Crystallogr.* **21**, 536-542.
- Garabagh, M. R. M., Nedjad, S.H., Shirazi, H., Mobarekeh, M.I. & Ahmadabadi M.N. (2008). *Thin Solid Films.* **516**, 8117-8124.
- Gevers, R. (1954a). *Acta Cryst.* **1**, 337-343.
- Gevers, R. (1954b). *Acta Cryst.* **1**, 740-744.
- Greenough, G. B. (1952). *Prog. Metal. Phys.* **3**, 176-219.
- Hirth, J. P. & Lothe, J. (1982). *Theory of Dislocations*, Wiley, New York.
- Huang, B. X., Huang, X. D., Wang, L. & Rong, Y.H. (2008) *Metall. Mater. Trans. A*. **39A**, 717-724.
- Joy, D.C. & Booker, G. R. (1971) *J Phys E Sci Instrum* **4**, 837.
- Keijser, de Th. H. & Mittemeijer, E. J. (1980). *J. Appl. Cryst.* **13**, 74-77.
- Kim, J. Y., Lee, S. J. & De Cooman, B.C. (2011). *Scr. Mater.* **65**, 363-366.
- Lassen, N. C. K. (1996) *Mater Sci Technol.* **12**, 837-843.



- Lassen, N. C. K; Jensen, D. J. & Conradsen, K. (1992) *Scanning Microsc.* **6**, 115-121.
- Li, X.W. (2009). *Adv. Mater. Res.* **79-82**, 215-218.
- Martin, S., Wolf, S., Martin, U., Krüger, L. & Rafaja, D. (2016) *Metal. Mater. Trans. A.* **47**, 49-58.
- Mittemeijer, E. J. & Delhez, R. (1978). *J. Appl. Phys.* **49**, 3875-3878.
- Müllner, P. & Ferreira, P.J. (1996). *Philos. Mag. Lett.* **73**, 289-297.
- Nishikawa, S. & Kikuchi, S. (1928a) *Nature* **122**, 726-726.
- Nishikawa, S. & Kikuchi, S. (1928b) *Nature* **121**, 1019-1020.
- Olson, G.B. & Cohen, M. (1976). *Metall. Trans. A.* **78**, 1897-1923.
- Paterson, M. S. (1952). *J. Appl. Phys.* **23**, 805-811.
- Pereira-da-Silva, M. de Assumpção. & Ferri, F.A. (2017) Scanning electron microscopy *Nanocharacterization Techniques*, William Andrew Publishing, 1-35.
- Pierce, D.T., Jimenez, J.A., Bentley, V., Raabe, D., Oskay, C. & Witting, J.E. (2014). *Acta Mater.* **68**, 238-253.
- Ray, I.L.F. & Cockayne, D. J. H. (1971). *Proc. R. Soc. Lond. A.* **325**, 543-554.
- Ruff Jr. A.W. (1970). *Metall. Trans.* **1**, 2391-2413.
- Sahu, P., Shee, S. K., Hamada, A. S., Rovatti, L., Sahu, T., Mahato, B., Ghosh Chowdhury, S., Porter, D.A. & Karjalainen, L.P. (2012). *Acta Mater.* **60**, 6907-6919.
- Scherrer, P. & Gottinger Nachrichten (1918). **2**, 98-100.
- Schmidt, N. H; Bildesorensen, J. B. & Jensen, D. J. (1991) *Scanning Microsc.* **5**, 637-643.
- Schramm, R.E. & Reed, R.P. (1975). *Metall. Trans. A.* **6**, 1345-1351.
- Singh, J.B., Sundaraman, M., Mukhopadhyay, P. (1988). *Phillos. Mag. A*, **57**, 499-523.
- Smallman, R.E. & Ngan, A.H.W. *Physical Metallurgy and Advanced Materials*, Seventh edition, Elsevier Ltd, 2007.
- Smallman, R.E. & Westmacott, K.H. (1957) *Philos. Mag.* **2**, 669-683.
- Stokes, A. R. (1948). *Proc. Phys. Soc.*, London, **61**, 382-391.
- Talonen, J., & Hanninen, H. (2007) *Acta Mater.* **55**, 6108-6118.
- Teutonico, L.J. (1967). *Philos. Mag.* **15**, 959-967.
- P. J; Wilkinson, A. J. & Watson, I. M. (2007) *Phys. Rev. B.* **75**, 085301.
- Turunen, M. J., Keijser, Th.H. de., Delhez, R., van der Pers, N. M. (1983). *J.*
- Ungár, T. & Borbély A. (1996). *Appl. Phys. Lett.* **69**, 3173-3175.
- Ungar, T. & Ribarik, G. (2017) *IOP Conf. Ser. Mater. Sci. Eng.* **194**, 1-8.
- Ungár, T. (2001). *Mater. Sci Eng. A.* **309-310**, 14-22.
- Ungar, T., Dragomir, I., Revesz, A., Borbely, A. (1999) *J. Appl. Crystallogr.* **32**, 992-1002.

- Ungár, T., Groma, I. & Wilkens, M. (1989). *J. Appl. Cryst.*, **49**, 26-34.
- Ungár, T., Ott, S., Sanders, P., Borbély, A. & Weertman, J.R. (1998). *Acta Mater.* **46**, 3693-3699.
- Ungar, T., Revesz, A. & Borbely, A. (1998) *J. Appl. Crystallogr.* **31**, 554-558.
- van Berkum, J. G. M., Vermeulen, A. C., Delhez, R., de Keijser, Th.H.. & Mittemeijer, E. J. (1994). *J. Appl. Cryst.* **27**, 345-357.
- Venables, J. A. & Harland, C. J. (1973.) *Philos. Mag.* **27**, 1193-1200.
- Veyssier, P. (1991). *ISIJ International*. **31**, 1028-1048.
- Warren, B. E. & Averbach, B. L. (1950). *J. Appl. Phys.* **21**, 595-599.
- Warren, B. E. & Averbach, B. L. (1952). *J. Appl. Phys.* **23**, 497-498.
- Warren, B. E. (1959). *Prog. Met. Phys.* **8**, 147-202.
- Warren, B. E. (1969). *X-ray diffraction*, Addison-Wesley, Reading, Mass.
- Wells, O. C. (1999) *Scanning*. **21**, 368-371.
- Wilkens, M. (1970) *Phys. Status Solidi (a)* **2**, 359-370.
- Wilkens, M. in: J.A. Simmons, R. de Wit, R. Bullough (Eds.), (1970) *Fundamental Aspects of Dislocation Theory Vol. II*, Natl Bur. Stand. Publ., Washington, 1195-1221.
- William, D.B. & Carter, C.B. (2010). *Transmission Electron Microscopy*, second ed., Springer Science, NY, Vol-3.
- Williamson, G.K. & Hall, W.H. (1953) *Acta Metall.* **1**, 22-31.

## *Part B*

*Case study of some coarse-grain  
high-Mn steels*



# *Chapter 3\**

## *Dislocation substructure study of Fe-25Mn-2Al-0.1C steel*

\*This chapter is published in Materials Letters, 282 (2021) 128691. (No. 1 in the list of publications)



### 3.1 Material processing & flow stress behavior

#### 3.1.1 Material and experimental

A steel with chemical composition Fe-25Mn-2Al-0.1C (in wt.%) was prepared by induction melting. Homogenization and hot rolling were carried out at 1100°C, followed by water quenching. Uniaxial tensile tests were carried out with DIN 50114 standard specimens in a Zwick Z 100 tensile testing machine at a strain rate of  $10^{-4} \text{ s}^{-1}$ . The test was interrupted at strains: 2%, 5% and 10%, and also continued until fracture. TEM specimens were prepared from gauge region of specimens with TenuPol-5 twin jet electropolisher using electrolyte containing 90% methanol and 10% perchloric acid. The specimens were observed in a JEOL 2200FS transmission electron microscope at 200 kV.

#### 3.1.2 Flow stress and strain hardening behavior

Fig. 3.1 reveals that the steel had excellent combination of high tensile strength  $\sim 1.4 \text{ GPa}$  at  $\sim 42\%$  fracture strain. The strain hardening rate (SHR) of the steel plotted as secondary Y-axis of Fig. 3.1(a) reveals that the SHR decreases rapidly until 16% strain, stage A, while the constant hardening regions (stages B and D) remained absent. Thereafter, the SHR decreases relatively slowly between 16% to 38% strain, (stage C), followed by yet another rapidly decreasing stage E until necking initiates. Thus, the present steel reveals a distinct three-stage strain hardening, which is clearly evident in modified Crussard-Jaoul (C-J) analysis, Fig. 3.1(b) (Jin & Lee, 2012). TWIP steels generally show four/five-stage strain hardening (De

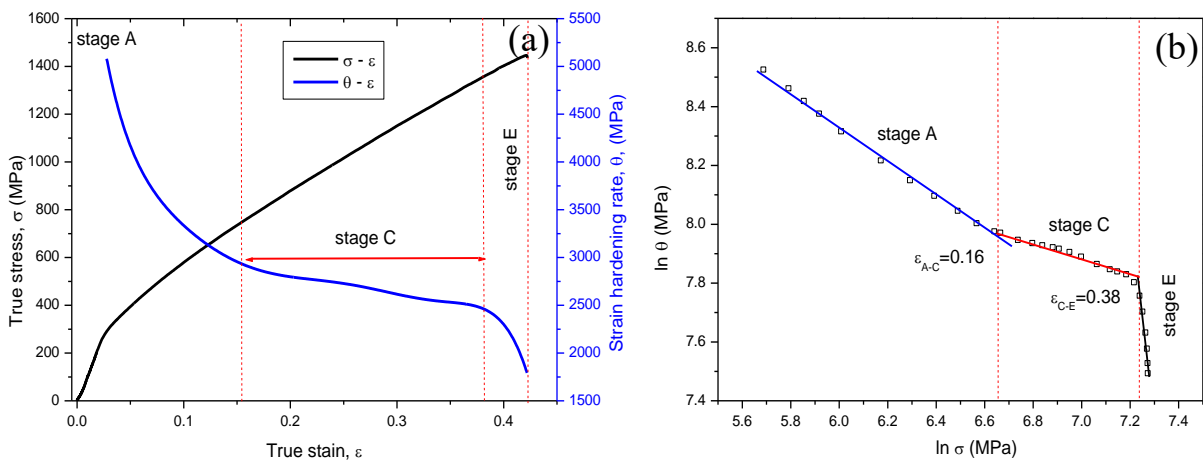


Fig. 3.1: (a) True stress-strain ( $\sigma - \varepsilon$ ) and strain hardening ( $\theta - \varepsilon$ ) responses of the steel (b)  $\ln \theta - \ln \sigma$  plot for modified C-J analysis.

Cooman *et al.*, 2018), while a three-stage strain hardening is also reported (Jin & Lee, 2012).

The absence of stages B and D in Fig. 3.1 implies slowdown of primary and secondary twinning, respectively, attributable to the rise in SFE of the steel due to presence of Al (Jin & Lee, 2012). In fcc crystals, stage A is a short initial strain hardening stage, which however was not observed here, since it extends until 16% strain (Fig. 3.1(a)). Kalidindi (1998) proposes that stage A is governed by dislocation glide and evolution in dislocation density, while twinning is expected in stage B. Furthermore, overlapping stacking faults (SFs) are also expected in stage A, which might correspond to twin incubation stage (De Cooman *et al.*, 2018). The microstructural evolution at intermediate strains is interpreted through a series of TEM micrographs in the following chapter.

### 3.2 TEM investigations of deformation microstructure & their influence on the strain hardening behavior

#### 3.2.1 TEM investigation at different stage of deformation

Fig. 3.2 shows early dislocation activity at 2% strain. The bright field (BF) image in Fig. 3.2(a) reveals activation of selective planar glide of mutually intersecting  $\frac{a}{2}\langle 110 \rangle$  perfect dislocations, likely due to the ‘glide plane softening effect’ arising from the SRO induced by Al (Yoo & Park, 2008). The corresponding weak beam dark field (WBDF) micrograph in a  $g - 3g$  condition additionally reveals that such dislocations are pinned and that they do not dissociate into Shockley partials. The dissociation widths of  $\frac{a}{2}\langle 110 \rangle$  dislocations under weak  $g - 3g$

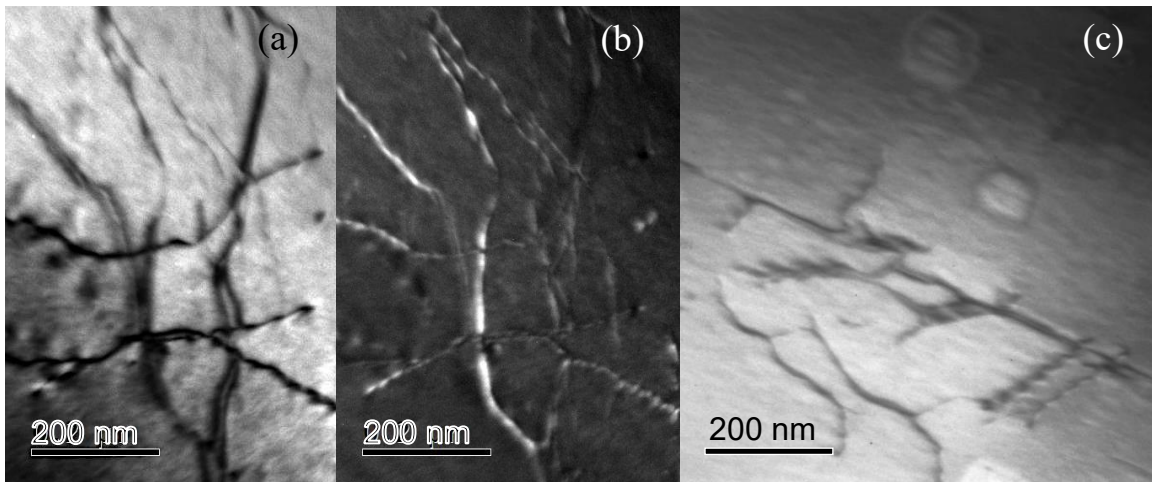


Fig. 3.2: Dislocation substructures at 2% strain: (a) planar glide of intersecting dislocations (b) WBDF imaging of (a) (c) stair-rod dislocation.



conditions are utilized previously to determine the SFE of TWIP steels (Mahato *et al.*, 2015, 2017). At this strain (i.e. 2%), it is also observed from Fig. 3.2(c) that a  $\frac{a}{6}\langle 110 \rangle$  stair-rod dislocation is formed when a Shockley partial on the primary plane cross-slips onto the conjugate plane to dissociate into a sessile stair-rod dislocation and another glissile Shockley partial according to the following reaction (Mori & Fujita, 1980; Mahato *et al.*, 2015):

$$\frac{a}{6} [\bar{1}21]_{(11\bar{1})} \rightarrow \frac{a}{6} [\bar{1}12]_{(1\bar{1}1)} + \frac{a}{6} [01\bar{1}]_{sessile} \quad (3.1)$$

Stair-rod dislocations formed due to multiple- and cross-slip (Mori & Fujita, 1980) results in high strain hardening by impeding the transmission of dislocations across a TB (Zhu *et al.*, 2011). Fig. 3.2(a) further ascertains that multiple-slip is activated at 2% strain, and therefore it is reasonable that any dissociated  $\frac{a}{2}\langle 110 \rangle$  dislocations could lead to the incidence of  $\frac{a}{6} [01\bar{1}]$  stair-rod dislocation according to Eq. (3.1). At 5% strain, the gliding  $\frac{a}{2}\langle 110 \rangle$  dislocations seen to interact further to produce a Taylor lattice (Fig. 3.3(a)), which is a low energy dislocation structure (LEDS) that forms at early strains due to planar glide on highly stressed glide planes, without involving any systematic lattice rotations (Kuhlmann-Wilsdorf, 1989). They are rare in TWIP steels; hence their contribution to strain hardening is still unclear (Gutierrez-Urrutia & Raabe, 2012). It is however known that the dislocations in a Taylor lattice rearrange themselves according to second law of thermodynamics to attain a low energy configuration (Bay *et al.*, 1989). LEDS can easily transform into dislocation cells at high strains (Kuhlmann-Wilsdorf, 1989; Gutierrez-Urrutia & Raabe, 2012). It is therefore expected that a microstructure containing Taylor lattice would reveal a gradually dropping SHR with increasing strain, as observed in Fig. 3.1(a).

A  $g_{1\bar{1}1}$  axial dark-field (DF) micrograph along  $B \approx [110]$  presented in Fig. 3.3(b) reveals nucleation and growth of a twin lamella at 5% strain. The extrinsic-intrinsic SF pair in the twin lamella is determined from the outer fringe contrast (Mahato *et al.*, 2015, 2017). Boucher and Christian (1972) proposed twinning is suppressed in presence of a homogenous dislocation distribution. The present study indeed supports their findings since the region of twin lamella in Fig. 3.3(b) remains devoid of any homogenous dislocation substructure in its vicinity. Fig. 3.3(c) further shows another grain at 5% strain revealing Shockley partials connecting the stair-rod dislocation to the twin, marking the onset of dislocation-twin interaction. At 10% strain, the interaction between the dissociated partial dislocations with randomly distributed fine SFs increase in the matrix, and the situation is depicted in Fig. 3.3(d).

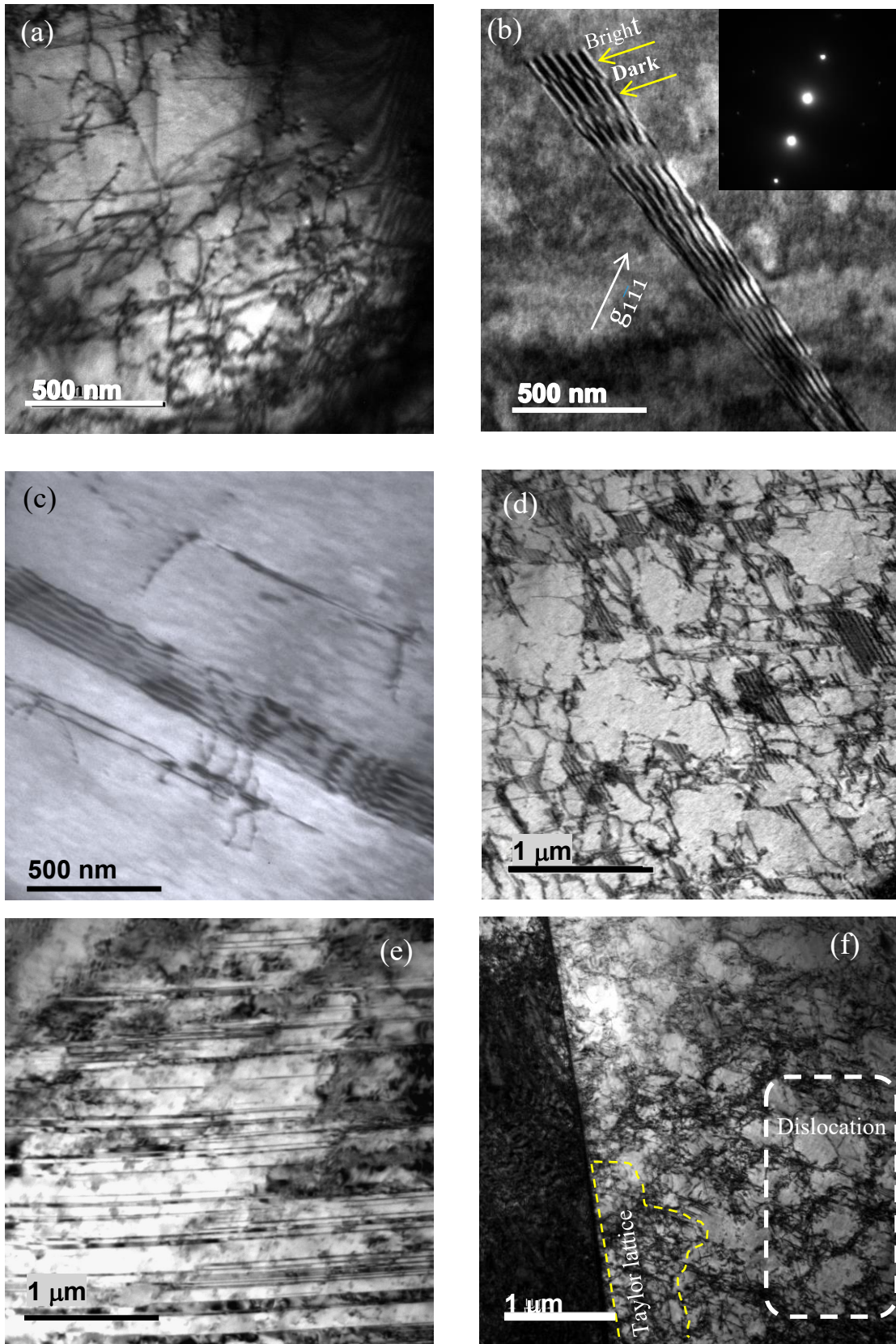


Fig. 3.3: Microstructures at higher strains: (a) Taylor lattice (b) twin lamella under DF (c) interaction between a twin and stair-rod dislocation (d) partial dislocations interacting with stacking faults (e) twin bundle at fracture (f) dislocation substructures at fracture.

The specimen at 42% strain reveals the formation of fine twin bundles in Fig. 3.3(e), which are believably responsible for the high SHR  $\sim 2.5$  GPa observed in stage C (De Cooman et al., 2018). However, no secondary twinning was observed at any strain, and is arguably the reason for the absence of stage D in Fig. 3.1 (Jin & Lee, 2012). Interestingly, the BF micrograph presented in Fig. 3.3(f) reveals the coexistence of dislocation cell and Taylor lattice at fracture strain (42%), implicating the conversion of Taylor lattice to dislocation cell through cross-slip (Bay *et al.*, 1989), causing dynamic recovery.

### 3.2.2 Interpretation of strain hardening behavior

Thus, a drop in SHR is not unusual since the dislocation storage capacity of the matrix is lowered (Hirsch, 1975). Therefore, the continuously decreasing SHR of the studied steel (Fig. 3.1(a)) is interpreted from cross-slip induced recovery of dislocations associated with dislocation cell formation and absence of secondary twinning. In other words, this is synonymous to that the contribution of dislocation strengthening here seems to overwhelm any contribution from twinning. Besides, the average size of dislocation cell,  $d_{\text{cell}}$  formed during deformation of fcc metals/alloys is governed by the well-known Holt relation (Holt, 1970):  $d_{\text{cell}} = \frac{K}{\sqrt{\rho}}$ , where, K is a coefficient  $\sim 7$  for austenitic steels (Koneva *et al.* 2008). The dislocation density value for the fractured specimen was  $\sim 10^{15} \text{ m}^{-2}$ , estimated from X-ray diffraction analysis (Mahato *et al.*, 2015, 2017), which further estimates that average  $d_{\text{cell}}$  for the present steel is  $\sim 0.23 \mu\text{m}$ , and several submicron cells are also observed in Fig. 3.3(f).

### References

- Bay, B., Hansen, N., Kuhlmann-Wilsdorf, D. (1989) *Mater. Sci. and Eng. A* **113**,385-397.
- Boucher, N., Christian, J. (1972) *Acta Metall.* **20**, 581-591.
- De Cooman, B. C., Estrin, Y., Kim S.K. (2018) *Acta Mater.* **142**, 283-362.
- Gutierrez-Urrutia, I., Raabe, D. (2012) *Acta Mater* **60**, 5791-5802.
- Hirsch P.B.: The Physics of Metals, Cambridge University Press, Cambridge, 1975.
- Holt, D.L. (1970) *J. Appl. Phys.* **41**, 3197-3201.
- Jin, J.-E., Lee, Y.-K. (2012) *Acta Mater.* **60**, 1680-1688.
- Kalidindi, S.R. (1998) *Int. J. Plast.* **14**, 1265-1277.

- Koneva, N.A., Starenchenko, V.A., Lychagin, D.V., Trishkina, L.I., Popova, N.A., Kozlov, E.V. (2008) *Mater. Sci. Eng. A*. **483-484**, 179-183.
- Kuhlmann-Wilsdorf, D. (1989) *Mater. Sci. and Eng. A* **113**, 1-41.
- Mahato, B., Shee, S.K., Sahu, T., Ghosh Chowdhury S., Sahu, P., Porter, D.A., Karjalainen, L.P. (2015) *Acta Mater.* **86**, 69-79.
- Mahato, B., Sahu, T., Shee, S.K., Sahu, P., Sawaguchi, T., Kömi, J., Karjalainen L.P. (2017) *Acta Mater.* **132**, 264-275.
- Mori, T., Fujita, H. (1980) *Acta. Metall.* **28**, 771-776.
- Yoo, J.D., Park, K.-T. (2008) *Mater. Sci. Eng. A* **496**, 417-424.
- Zhu, Y.T., Wu, X.L., Liao, X.Z., Narayan, J., Keckés, L. J., Mathaudhu, S. N. (2011) *Acta Mater.* **59**, 812-821.

# *Chapter 4\**

## *Deformation behavior study of Fe-25Mn-0.1C-0.4Si-xAl (x=0,1,3) Steel*

\*The contents of this chapter are published in Materials Characterization, 196 (2023) 112567. (No. 2 in the list of publications), Journal of Materials Engineering and Performance, 32, 1636-1644 (2023) (No. 3 in the list of publications)



**4.1 Material, its processing and the flow stress behavior**

**4.1.1 Material and experimental**

Three Fe-25Mn-0.1C-0.4Si steels with different Al contents, 0, 1 and 3 % (hereinafter coded as: 0Al, 1Al and 3Al, respectively), were prepared by induction furnace melting under Ar atmosphere. The chemical compositions of the studied steels are given in Table 4.1. The specimens were homogenized at 1200°C for 4h in a tubular furnace under Ar atmosphere to eliminate the segregation of different alloying element. The homogenized samples were then hot rolled at 1100°C followed by annealing at 1000°C for 1h and finally cold rolled to a thickness reduction ~50%. The cold rolled plates were solution treated at 800°C for 30 minutes and water cooled to reach room temperature (RT). Uniaxial tensile tests were carried out until failure with specimens, cut the axis parallel to the rolling direction, having the gauge section 6x3.6 mm<sup>2</sup> and the gauge length of 30 mm using a Zwick Z100 tensile testing machine (Zwick Roell, GmbH) at RT with a true strain rate of 10<sup>-4</sup> s<sup>-1</sup>. The low strain rate was deliberately selected to avoid any adiabatic heating during tensile straining which might alter the SFE of the steels.

**Table 4.1:** Chemical composition of studied steels (wt%).

Alloy code	C	Mn	Al	Si	Fe
0Al	0.14	25.1	0.01	0.40	Bal.
1Al	0.10	25.0	1.2	0.42	Bal.
3Al	0.10	24.8	3.4	0.45	Bal.

The uniformly strained gauge regions of the fractured specimens were electrolytically polished to prepare specimens suitable for XRD investigations. XRD data acquisitions of the fractured specimens were carried out on a Bruker D8 Advance laboratory X-ray powder diffractometer operating in the Bragg-Brentano geometry, using Ni-filtered Cu-K $\alpha$  radiation. The peak shape and instrumental broadening parameters were assessed from the X-ray powder patterns of LaB<sub>6</sub>, NIST SRM660b specimen.

The specimens were mechanically ground to about 100  $\mu$ m thickness and 3 mm disks were punched for TEM investigations. The TEM foils were prepared by electropolishing the disks in a TenuPol-5 using a solution of 90% methanol and 10% perchloric acid at -30 °C at 30 V. The TEM observations were carried out on a JEOL 2200FS electron microscope operating at 200 kV having a GATAN 994UltraScan® 1000XP imaging system. Linear intercept method was used to measure the grain sizes of the steels and it was seen that grains are more or less

equiaxed with values: 43, 35 and 45  $\mu\text{m}$  for 0Al, 1Al, and 3Al steels, respectively.

#### 4.1.2 Flow stress behavior

Fig. 4.1 shows the stress-strain response and the strain hardening rate (SHR) of the steels tensile strained at RT at a low strain rate of  $10^{-4} \text{ s}^{-1}$ . The flow stress curves in Fig. 4.1(a) reveal an early discontinuous yielding associated with 1Al steel, while the other two steels show a continuous yielding until fracture and that neither of the flow curves reveal any serrated flow behavior (Fig. 4.1(a)). Discontinuous yielding in high-Mn steel is attributed to the formation of Lüders band, which promotes a delayed as well as low strain hardening rate (Kim & De Cooman, 2016). On the other hand, the absence of serrated flow behavior is credited to absence in dynamic strain aging (DSA) which is usually not favored in low-Carbon high-Mn steels (De Cooman *et al.*, 2018), arising due to successive blocking of moving dislocation by solute atoms (Cottrell, 1953), and such effect is diminished when the SFE of the steel increases due to increasing Al addition (Kim & De Cooman, 2016) and/or by reduced C diffusivity in the alloy

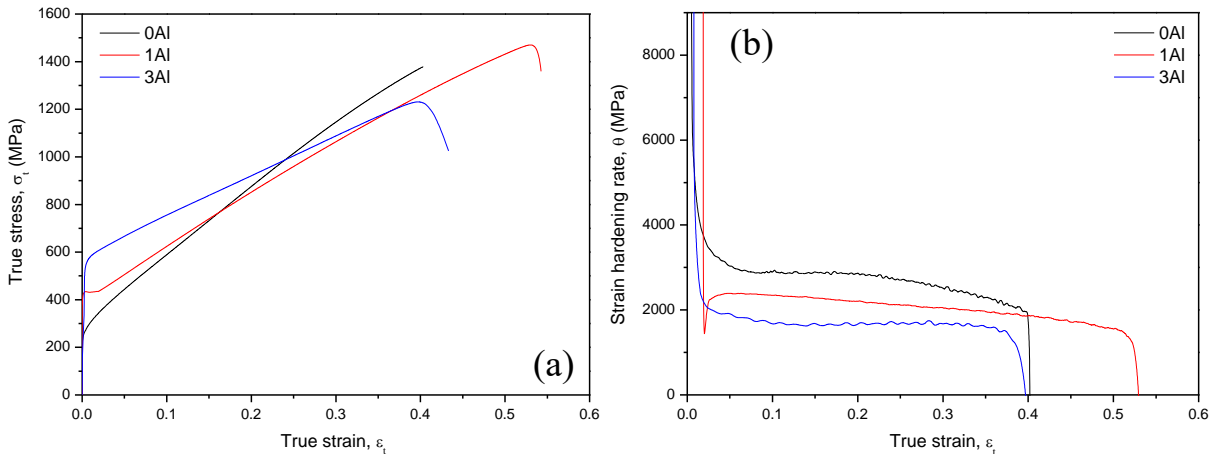


Fig. 4.1: (a) True stress-strain ( $\sigma_t - \varepsilon_t$ ) curves of the studied steels (b) Strain hardening responses ( $\theta - \varepsilon_t$ ) of the steels.

(Zuidema *et al.*, 1987). It is also seen that the yield strength (YS) increases and the SHR decreases with increasing the Al content. Mechanical properties of the studied steels obtained from the tensile tests are presented in Table 4.2, showing that the YS of 0Al steel is  $\sim 232 \text{ MPa}$ , increasing to  $\sim 516 \text{ MPa}$  for 3Al steel. Hamada *et al.* (2007) also showed that a 25Mn steel had the lower YS than that of a 25Mn with 3%Al steel at all testing temperatures between  $-80$  and  $200^\circ\text{C}$ . In the present study, the variation in YS values due to varying Al content in the steels appears much more pronounced than those reported in the literature (De Cooman *et al.*, 2018).



This is attributed to completely different plasticity mechanisms prevailing in the respective steels leading to different microstructures and thereby providing different resistance to dislocation motion and plastic flow, which will be described subsequently. From Fig. 4.1(a) and Table 4.2 it is also seen that among the studied steels, 1Al has the highest true ultimate tensile strength (UTS) ~ 1470 MPa along with highest true tensile elongation (TE) to fracture ~ 54%.

**Table 4.2:** Mechanical properties of the studied steels obtained from tensile test (true values).

Steel	YS(MPa)	UTS(MPa)	TE (%)
0Al	232	1377	40
1Al	396	1471	54
3Al	516	1226	43

UTS = ultimate tensile strength in true strain; TE = tensile elongation in true strain

The strain hardening behaviors of the studied steels are further presented in Fig. 4.1(b), represent almost same nature - revealing nearly a stable or slightly decreasing hardening after the initial rapid decrement while almost identical continuous nature for 0Al and 3Al steels but a tiny discontinuity at 2% strain is observed for 1Al steel. It is also readily seen from Fig. 4.1(b) that 0Al steel exhibits the highest SHR for the entire deformation range despite its lowest YS, while the converse being true for 3Al steel. Another distinct detail from Fig. 4.1(b) is that SHR of the studied steels decreases with increasing the Al content. Jin and Lee (2012) attributed the decreasing nature of SHR with increasing Al addition to the diminution of mechanical twinning arising from increase in SFE due to increasing Al content, though they did not systematically study the associated microstructure using diffraction-based techniques. Thus, the important features of the microstructural evolution with increasing Al concentration in the present steels are investigated using the XLPA based on the description in chapter 2 and their correlation to the mechanical properties is described in the next section.

#### 4.2 Microstructural investigation using X-ray line profile analysis (XLPA)

X-ray line profile analysis (XLPA) is one of the most important indirect techniques to characterize the deformed metals and alloys since it can easily reveal the microstructural information of the deformed sample through the estimations of dislocation density, crystallite size, fault probability and the active slip systems. In the following chapter, a detailed analysis of X-ray diffraction line profile and the evaluation of the different microstructural parameters of differently deformed specimen is discussed.

#### 4.2.1 Normalized intensity profiles and anisotropic strain broadening

The characteristic XRD profiles of (111), (200), (220), (311) and (222) austenite reflections are considered in this study for XLPA analysis and the results are listed in Table 4.3. The normalized measured intensity of the above-mentioned diffraction profiles for 1Al and 3Al steels are plotted in Fig. 4.2, as a representative. Fig. 4.2 shows the variation of normalized intensity of the measured diffraction profiles with  $\frac{2(\sin \theta - \sin \theta_m)}{\lambda}$ , where  $\theta_m$  is the angular maxima of the corresponding Bragg reflections. The experimentally measured diffraction profiles comprise of both instrumental broadening profile convoluted with true diffraction profiles. Therefore, the measured profiles were first deconvoluted according to the approach suggested by Enzo *et al.* (1988) and then the deconvoluted profiles were used in XLPA for microstructural parameters estimation. It is qualitatively evident from the normalized intensity plots in Fig. 4.2 that the (111) diffraction profile suffers from the minimum broadening, while the higher broadening is observed for rest of the Bragg reflections. A further observation in Fig. 4.2(a) and Fig. 4.2(b) is that the FWHMs of the Bragg reflections in 1Al steel are almost independent of the order of diffraction (Fig. 4.2(a)), while the FWHMs for 3Al steel strongly depends on the diffraction order (Fig. 4.2(b)), directly indicating the presence of anisotropic broadening in 3Al, which is discussed in the following section. Additionally, a Rietveld analysis (1969) of the XRD patterns were also carried out using the MAUD program (2006) to estimate the phase constituent of the steels and a selected angular range are presented in Fig. 4.2(c). A critical observation of Fig. 4.2(c) shows that (111) austenite Bragg reflection shifts towards lower Bragg angle due to increase in lattice parameter (Table 4.3) with the increment of Al concentrations, which was also observed by Tian *et al.* (2008) in their studies involving Fe-Mn-Al-C austenitic steels.

**Table 4.3:** Microstructural parameters obtained from X-ray line profile analysis.

Steel	Lattice parameter, $a$	Dislocation character parameter, $q$	Contrast factor ( $C_{111}$ )	Stacking fault probability $P_{sf}(\times 10^{-3})$	Twinning fault Probability $P_{tw}(\times 10^{-3})$	Dislocation density, $\rho(\times 10^{15} \text{ m}^{-2})$	Outer cut-off radii of dislocation $R_e$ (nm)	Dislocation arrangement parameter, $M = (R_e \sqrt{\rho})$	SFE, $\gamma$ (mJm <sup>-2</sup> )
0Al	3.6061	2.28	0.064	7.6	11.89	9.91	35	3.48	18.1
1Al	3.6157	2.29	0.063	4.9	21.7	7.72	68	5.97	25.7
3Al	3.63	2.46	0.048	2.8	-2.22	4.59	104	7.04	41.6

### 4.2.2 Effect of strain anisotropy on Williamson-Hall plots

The FWHM of austenite reflections from the studied steels, thus obtained from a pseudo-Voigt function fitting is inserted in Eq. (2.11) to obtain the conventional W-H plot. It should be mentioned that due to simultaneous presence of austenite and  $\epsilon$ -martensite phases in 0Al steel, the FWHM of austenite (111) reflection was evaluated from the deconvoluted XRD patterns fitted according to Rietveld refinement (1969). In Fig. 4.3(a), the FWHMs of the austenite reflections for the three studied steels are scaled with the diffraction vector,  $K$ , wherein, a significant, but comparable scatter in *conventional* W-H plots is also observed. This scatter is essentially invoked by the dislocation induced anisotropic strain broadening in the deformation microstructures of the studies steels.

The character as well as geometry, *i.e.*, arrangement of the dislocations, bear the influence of deformation microstructure on the peak broadening (Sidor *et al.*, 2021). It is further accepted that the strain broadening contributions of a dislocation strongly depends on the

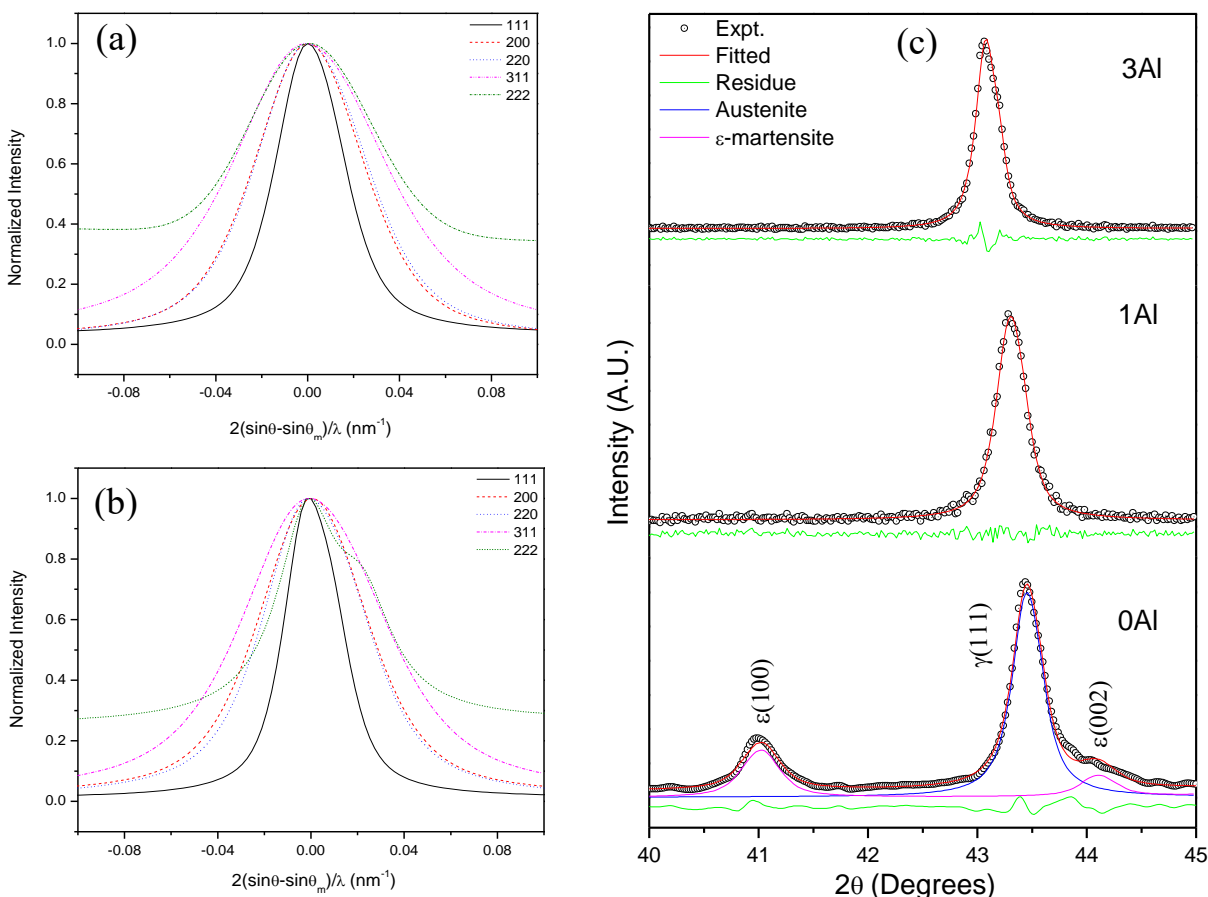


Fig. 4.2: Normalized X-ray diffraction profiles of the fractured steel specimens expressed in the intensity versus  $2(\sin\theta - \sin\theta_m)/\lambda$  for: (a) 1 Al and (b) 3Al steel. (c) A selected angular range of diffraction profiles for the studied steels.

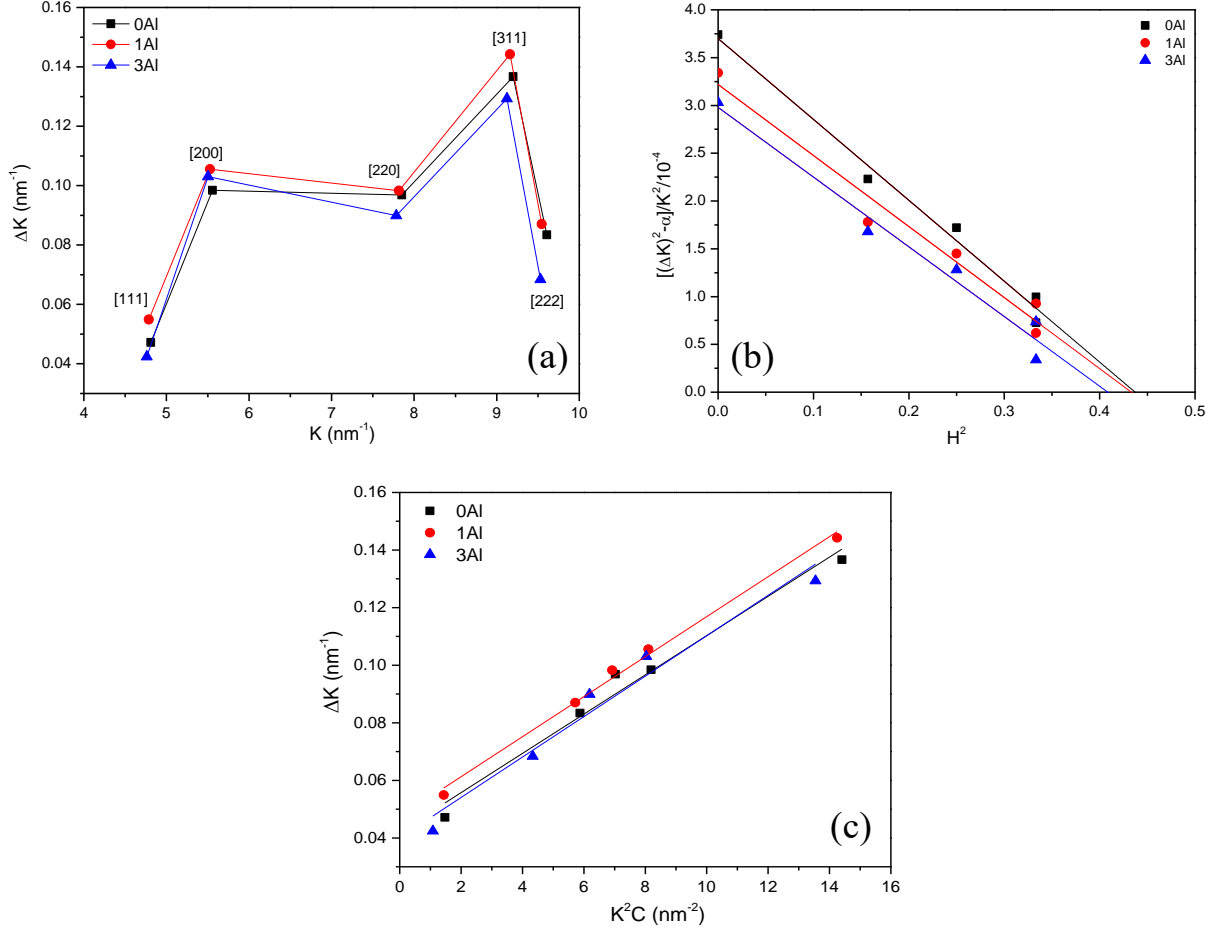


Fig. 4.3: (a) The conventional Williamson-Hall plots (b) linear fitting to the variation of  $[(\Delta K^2) - \alpha]/K^2$  with  $H^2$  according to Eq. (2.16) (c) the *modified* Williamson-Hall plots of the studied steels.

relative orientations between the diffraction vector, line and Burgers vector of that dislocation - quite identical to the dislocation image contrast observed in TEM (Ungár, 2003). Therefore, the concept of W-H plot is modified according to Eq. (2.12) to evaluate the influence of dislocation-induced strain broadening on deformation microstructures after invoking the dislocation contrast factor approach (Ungár *et al.*, 1998). The  $q$  parameter for the three studied steels is directly estimated in Fig. 4.3(b) from a linear fitting of Eq. (2.16) without any priori assumptions related to the fraction of  $\frac{a}{2}\langle 110 \rangle$  edge and screw dislocations present in the deformation microstructure. This approach helps to yield actual proportion of  $\frac{a}{2}\langle 110 \rangle$  edge and screw dislocations, whose respective values are presented in Table 4.3 for the steels with the varying Al concentration. The respective  $q$  values obtained from Fig. 4.3(b) are also listed in Table 4.3 and they are further utilized to estimate the average contrast factors  $\bar{C}_{hkl}$  according to Eq. (2.14), also shown in Table 4.3. It is seen that  $\bar{C}_{111}$ , decreases gradually with increasing

Al addition, indicating towards diminishing dislocation-induced strain anisotropy effect at higher Al concentrations.

The obtained FWHM of each Bragg reflections for the studied steels are once again plotted (i.e., *modified* W-H plot) according to Eq. (2.12) in Fig. 4.3(c) when scaled with  $K^2 \bar{C}_{hkl}$ , leading to significantly smoother curves. A direct comparison between the normal and the *modified* W-H plots presented in Fig. 4.3(a) and Fig. 4.3(c) clearly suggests that the incorporation of dislocation-induced anisotropic strain broadening in XLPAs analyses leads to remarkable improvement in reproducing the diffraction profiles of the deformed steel specimens. A critical interpretation of Fig. 4.3(c) would still allow oneself to conclude that though the FWHMs of the three steel specimens on *modified* Williamson-Hall plots show some scatter the improvement when compared to Fig. 4.3(a) is very much significant. This scatter can be attributed to the fact that the specimens representing Fig. 4.3(c) correspond to a highly deformed state, i.e., fracture strain and thus, development and/or rearrangement of some complex dislocation substructure in the microstructures at high strains are not usual, which are not accurately modelled even by the dislocation contrast factor approach (Ungar *et al.*, 1996).

#### 4.2.3 Conventional and modified Warren-Averbach analysis

The Fourier coefficients of each Bragg reflection are calculated from the Fourier transformation of the experimental intensity distributions, and only the real part of the Fourier coefficients,  $A(L)$ , are plotted against  $K^2$  in Fig. 4.4(a) for 1Al steel, as a representative. The *conventional* W-A plot in Fig. 4.4(a) reveals that  $\ln A(L)$ s for different  $L$  obeys a similar kind

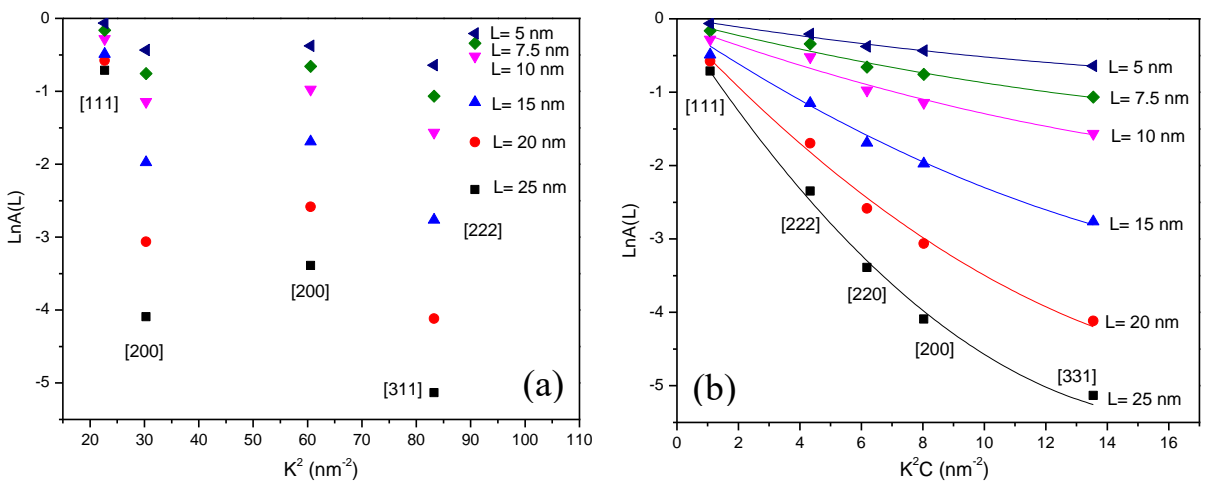


Fig. 4.4: Variation of logarithmic Fourier coefficient,  $\ln A(L)$ , of 1Al steel at different  $L$  values according to: (a) *conventional* Warren-Averbach analysis (b) *modified* Warren-Averbach analysis.

of behavior like the FWHMs revealed in the *conventional* W-H plots (Fig. 4.3(a)). The same Fourier coefficients when plotted according to the *modified* W-A equation (Eq. (2.19)) in Fig. 4.4(b) with the scaling factor,  $K^2 \bar{C}_{hkl}$ , yield significantly smoother curves, and the same is presented for 1Al steel as a representative. A comparison of Fig. 4.4(a) and Fig. 4.4(b) also emphasizes the importance of dislocation-induced anisotropic strain broadening in the 1Al steel. It is also seen from Fig. 4.4(b) that  $\ln A(L)$  vs  $K^2 \bar{C}$  follows almost a linear relationship for all  $L$  values until the first four Bragg reflections, and the slopes of the linear regions in  $\ln A(L)$  vs  $K^2 \bar{C}$  plots are further used for estimating dislocation densities, which is discussed in the following.

### 4.3 Effect of Al on different microstructural parameters

#### 4.3.1 Evolution of dislocation parameters with Al content

The slopes obtained from the linear portion of the *modified* W-A plot (Fig. 4.4(b)) are plotted against  $\ln(L)$  in Fig. 4.5 and fitted according to Eq. (2.20) to estimate the dislocation distribution ( $M$ ) and density ( $\rho$ ) related parameters in Table 4.3. The dislocation density and outer cut-off radius ( $R_e$ ) for each steel were computed from the gradient and ordinate intercept of the linear fittings, shown in Fig. 4.5. The  $R_e$  value indicate the measure of screening effect of dislocation strain field due to the presence of other dislocations, and a lower  $R_e$  value

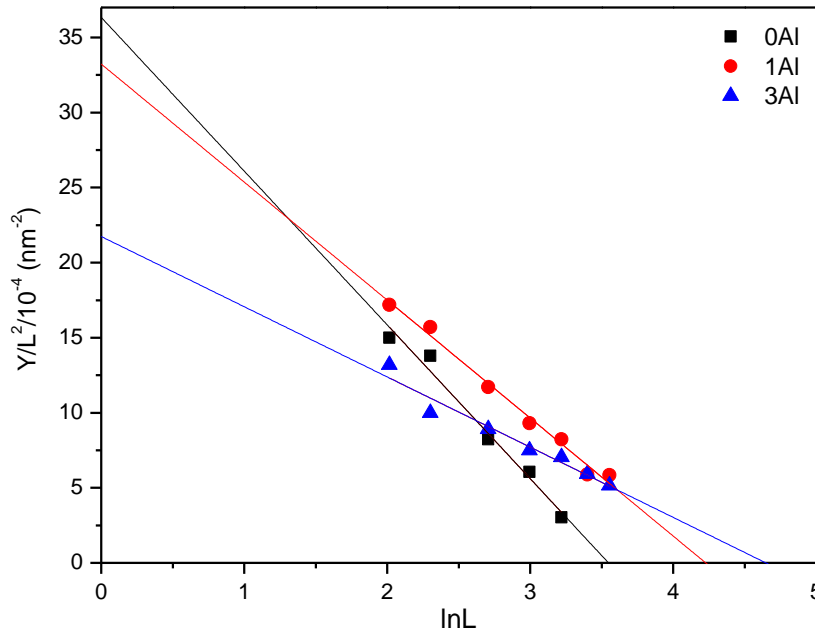


Fig. 4.5: Linear fitting to the variation of  $Y(L)/L^2$  with  $\ln(L)$  for the studied steels according to Eq. (2.20).

suggests a higher level of screening, depending on the arrangement of dislocations existing in a microstructure (Ungar & Borbely, 1996). The dislocation character parameter  $q$ , signifying the edge/screw or mixed character of dislocations present within austenite microstructure is obtained from the linear fittings of Eq. (2.16), also included in Table 4.3. The various dislocations related parameters reported in Table 4.3 are further plotted against Al concentration in Fig. 4.6 to comprehensively represent the correlation of dislocation parameters with the Al content.

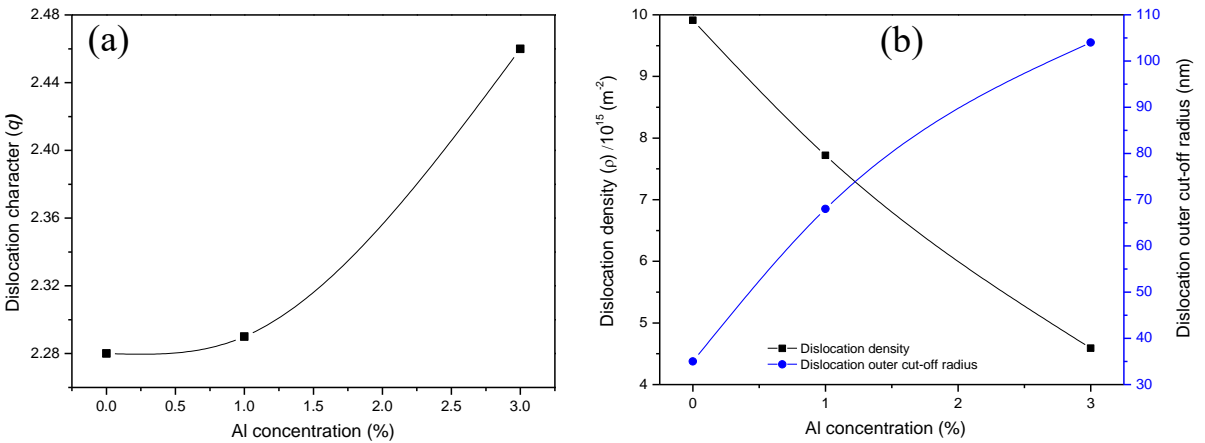


Fig. 4.6: Variation of dislocation parameters with Al content for the studied steels: (a) dislocation character (b) dislocation density and dislocation outer cut-off radius.

It can be seen from Fig. 4.6(a) and Table 4.3 that a  $q$  value  $\sim 2.28$  was obtained for 0Al steel and that it remains nearly constant within the accuracy limit for 1Al steel, while finally increasing to  $\sim 2.46$  for 3Al steel. This corresponds to a population of of about: 76%, 78% and 100% of screw dislocations, for 0Al, 1Al and 3Al, respectively. Additionally, Fig. 4.6(b) and Table 4.3 suggest that all steels exhibit a dislocation density  $\sim 10^{15} \text{ m}^{-2}$ , which decreases with increasing the Al concentration, whereas the  $R_e$  values show the opposite trend. Fig. 4.6(b) and Table 4.3 further reveal that relatively low  $R_e$  value of  $\sim 35 \text{ nm}$  was obtained for 0Al steel, which gradually increased to  $\sim 104 \text{ nm}$  for 3Al steel. It is worth mentioning that  $R_e$  value  $\sim 35 \text{ nm}$  in 0Al steel is significantly lower relative to as estimated in other steel microstructures deformed to failure strain (Das *et al.*, 2021).

The gradually increasing  $q$  value in Table 4.3 and Fig. 4.6(a) has an obvious ramification that the population of screw dislocations in the microstructure at failure strains increases with increasing Al content. In a microstructure comprising of high density of screw dislocations, the dislocations can easily change their slip planes by cross-slip (Hull & Bacon, 2011). Thus, the governance of screw nature of dislocations in 3Al steel suggests that cross-

slip would be predominant and some drop in the dislocation density should be expected due to dynamic recovery during straining (Kim *et al.*, 2018). This kind of situation is generally expected in microstructure of a high SFE alloy, and this will be discussed further subsequently.

On the other hand, the variation of  $R_e$  presented in Fig. 4.6(b) directly suggests that the dislocations are strongly correlated for 0Al steel as compared to the other two steels - lowest being observed in 3Al steel. Usually, a lower  $R_e$  value is expected for highly deformed metals/alloys, wherein strongly correlated dislocation substructures are formed in the microstructure during deformation (Sahu *et al.*, 2012; Das *et al.*, 2021). Though, all the estimated dislocation densities are of the order of  $\sim 10^{15} \text{ m}^{-2}$  but their magnitude gradually decreases with increasing the Al content. The minimum dislocation density is observed in 3Al steel and the variation of dislocation density with Al content is plotted in Fig. 4.6(b). A similar trend of variation in the dislocation density was also observed by Jeong *et al.* (2012) while studying the deformation behavior of Fe-18Mn-(0 to 3)Al-0.6C steels.

The decrease in the dislocation density with increasing the Al content in the present steels can be understood from the interrelation between SFE and dynamic recovery rate. Kim *et al.* (2018) observed that a low SFE twinning induced plasticity (TWIP) steel exhibits a lower dynamic recovery rate than its higher SFE counterpart, and thus a higher dislocation density should be expected in low SFE TWIP steels and consequently the SHR would be higher. Therefore, the high SHRs in Fig. 4.1(b) and dislocation density in Table 4.3 for 0Al steel collectively suggest that it should have a lower SFE compared to those of 1Al and 3Al steels.

Wilkens (1970), however, has suggested that the behavior of dislocations in a microstructure containing dislocation substructures are not understood precisely by considering the dislocation density alone, and thus introduced a dimensionless parameter ( $R_e\sqrt{\rho}$ ), known as Wilkens parameter, whose value directly depends on the correlation degree of dislocations. A value of the Wilkens parameter close to unity signifies that the dislocations are strongly correlated; otherwise, they could be regarded as randomly distributed (Wilkens, 1970). As revealed from Table 4.3, the lowest value ( $\sim 3.48$ ) of the Wilkens parameter was obtained for 0Al steel, which is still significantly higher than the unity, and the values are even higher for 1Al and 3Al steel ( $\sim 5.97$  and  $7.04$ , respectively). Dastur & Leslie (1981) suggested that a reduction in the dislocation correlation happens most probably due to the fact that Al alloying not only raises the SFE of high-Mn steels, but also decreases the chances of twin growth in deformed austenite. This postulate for the present steels about the role of Al addition on SFE and the corresponding deformation mechanism will be tested on the basis of TEM studies, which will be discussed respectively in Section 4.3.3 and 4.4.1.



### 4.3.2 Effect of Al concentration on planar fault densities

It is well understood that XLPA is capable to determine the planar fault propensities in close packed deformed microstructures in a statistically significant manner - Warren's (1969) and Balogh's *et al.* (2006) approaches are most widely used for metals and alloys. Both approaches concur that planar faults influence the peak shift, broadening and asymmetry of a diffraction profile. However, the Warren approach (1969) relates to the occurrence of asymmetry in a diffraction profile due to the presence of deformation twins in microstructure, whereas the peak shift is ascribed to stacking faults only. Thus, the stacking faults probability,  $P_{sf}$ , representing the fraction of slip planes affected by stacking faults was evaluated from the peak shift analysis, whereas the twin fault probability,  $P_{tw}$ , signifying the twin density with the austenite microstructure of the deformed specimen was estimated from the asymmetry of (200) Bragg reflections using Warren's approach (1969). The corresponding peak shifts of (111) and (200) Bragg reflections for the studied steels were measured with respect to the corresponding peak positions of the annealed specimens. The measured peak shifts against the Al concentration of the steels are presented in Fig. 4.7(a). It is seen from Fig. 4.7(a) that the amount of peak shift decreases for both the (111) and (200) reflections with the increased Al concentration, suggesting that a lower value of  $P_{sf}$  is expected at higher Al concentration. The corresponding peak shifts were further used for  $P_{sf}$  estimations, and the respective  $P_{sf}$  values for the three steels are listed in Table 4.3.

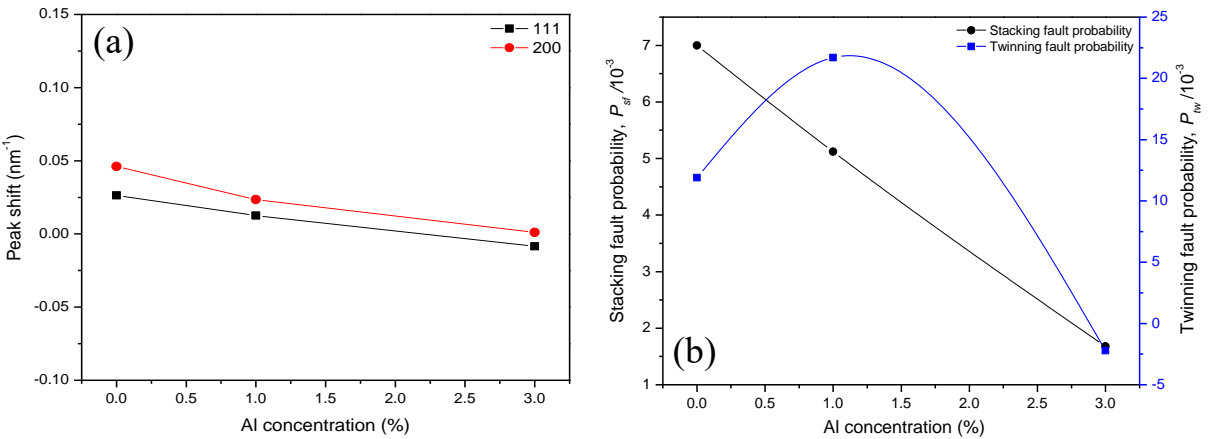


Fig. 4.7: Variation of planar fault parameters with Al content: (a) Peak shifts of (111) and (200) Bragg reflections (b) stacking and twinning fault probability.

The measured fault probabilities are further plotted in Fig. 4.7(b) showing the effect of Al concentration on planar fault abundance in the microstructure. The  $P_{sf}$  values reveal in

accordance with Fig. 4.7(a) that they decrease linearly from 0.0076 to 0.0028 with the Al content increasing from 0 to 3 wt.%. Tian *et al.* (2008) also reported a similar type of linear relationship between SFP and Al concentration while studying austenitic Fe-25Mn-(1.16-9.77)Al-0.68C (at%) alloys. However, the  $P_{sf}$  values estimated by them were higher by an order of magnitude than the values obtained in the present study (Table 4.3). Further, the  $P_{tw}$  values for the present steels are also plotted as a secondary axis in Fig. 4.7(b), indicating that  $P_{tw}$  increases up to 1 wt.% Al content, and then it falls significantly in case of 3Al steel. This has the obvious implication that more intense mechanical twinning is expected in 1Al steel as compared to 0Al and 3Al steels, which was further inspected by TEM examinations which results will be described in Section 4.4.1.

### 4.3.3 Effect of Al concentration on SFE

The subregular solution based thermodynamic model (Saeed-Akbari *et al.*, 2009) suggests that Al addition increases the SFE of high-Mn steels, signifying that the equilibrium energy of the stacking faults increases at higher Al contents. This is consistent with the observed variation of  $P_{sf}$  in Fig. 4.7(b). Schramm and Reed (1975) proposed the first model for estimate the SFE in austenitic steels from X-ray diffraction technique, which was later modified by Dey *et al.* (2005) after taking into account the effect of dislocation-stacking fault interactions (Schramm and Reed, 1975; Mahato *et al.*, 2015). The estimated various dislocation related parameters in Table 4.3 were then utilized to estimate the SFE ( $\gamma$ ) of the considered steels according to the Eq. (2.26) and the values computed are also listed in Table 4.3 being 18.1 mJm<sup>-2</sup> for 0Al steel, increasing to 25.7 mJm<sup>-2</sup> for 1Al steel and finally reaching 41.6 mJm<sup>-2</sup> for 3Al steel.

The SFE values plotted against Al content in Fig. 4.8 are further fitted according to a relation:  $\gamma = 18 + 7.85 \times (\text{Al wt.}\%)$ , which clearly revealed that SFE increases linearly with a constant slope of  $\sim 7.85$  mJm<sup>-2</sup> per 1 wt.% Al for the considered Fe-25Mn-(0-3)Al-0.014C-0.42Si steels. The subregular solution based thermodynamic model suggests that SFE of high Mn steels should increase linearly with Al addition, and the increment is 8.7 mJm<sup>-2</sup> per 1 wt.% Al (Saeed-Akbari *et al.*, 2009). Dumay *et al.* (2008) predict this increment as 6 mJm<sup>-2</sup>. A similar linear relationship between SFE and Al concentration was previously observed by Jin and Lee (2012) for Fe-18Mn-0.6C-xAl TWIP steels, while they reported the SFE increment of about  $\sim 7$  mJm<sup>-2</sup> /wt.% irrespective of the Mn and C contents of the steel. However, the SFE of binary Fe-Mn steels is known to depend strongly on the Mn content and it increases with increasing

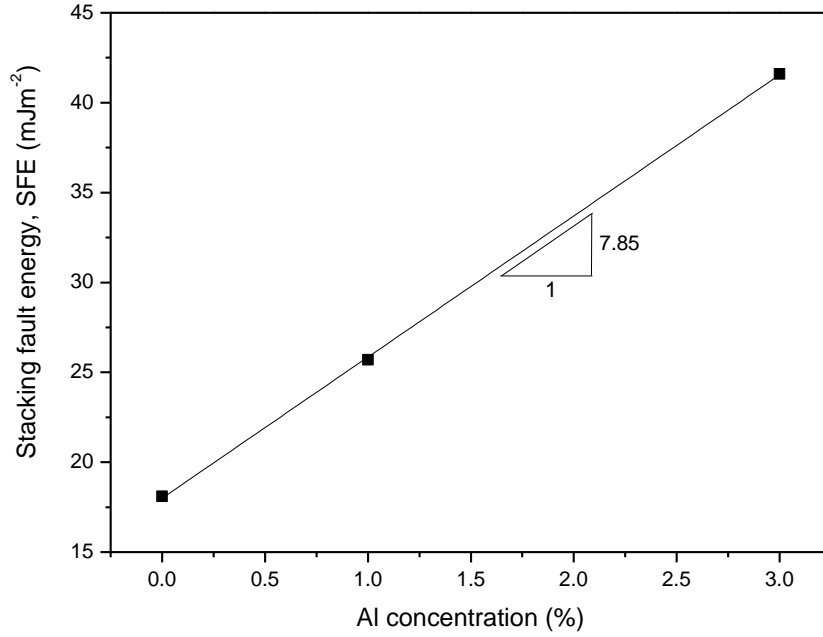


Fig. 4.8: Effect of Al content on the stacking fault energy at room temperature.

Mn content (Lee & Choi, 2000). There are contradicting reports about the role of C on SFE of austenite in high-Mn steels, but for steels with the Mn content higher than 25 wt.%, it increases with increasing C content (Zambrano, 2016). Besides the role of Al on the SFE of Fe-Mn-Al-C steels, the influence of C content on the SFE cannot be ignored - it is profound when the C content is higher and the SFE of the steel increases between a C content: 0.23% - 1.41% (Peng *et al.*, 2014). Therefore, it appears that although the considered steels had slightly varying C contents (Table 4.1), its effect on the SFE should not be as profound as that due to Al variation and thus the effect of Al content on SFE is properly captured in this study. Any difference in the rate of SFE increment due to Al variation should be attributed to the different methodologies used in the literature (Saeed-Akbari *et al.*, 2009; Jin & Lee, 2012).

It is well established that SFE in a close packed metals/alloys have significant influence on their deformation behavior. Thus, it is expected that Al addition would also affect the deformation mode. Kim and De Cooman (2016) revised the SFE limit suggested by Allain *et al.* (2004) to:  $\sim 13 \text{ mJm}^{-2}$  for observing  $\gamma \rightarrow \epsilon$  transformation and they also proposed a SFE dependent deformation map for high-Mn steels. De Cooman *et al.* (2018), in their seminal review work on high-Mn steels, subsequently point out several deviations from the SFE map and attributed that to uncertainty associated in SFE measurements. Nevertheless, since  $\gamma \rightarrow \epsilon$  transformation is observed in 0Al steel (Fig. 4.2(c)), it appears that the map proposed by Kim and De Cooman (2016) is not tenable here, rather the model of Allain *et al.* (2004) holds well.

Extending this argument to 1Al and 3Al steels, their respective SFE values 25.7 and 41.6 mJm<sup>-2</sup> in Table 3 collectively indicate that significant mechanical twinning and dominance of dislocation plasticity would be expected in those steels. However, the predictions of deformation microstructures only using an indirect method such as the XLPAs is not straightforward for TWIP steels since the carbon also plays a key role in their mechanical properties and provides a very strong solid solution effect (De Cooman *et al.* 2018) and thus the deformation microstructures will be further inspected for the considered steels through direct TEM investigations in the following.

#### 4.4 TEM investigations & its implications on the deformation mechanism

##### 4.4.1 TEM investigations of the deformation microstructure

A set of TEM bright field (BF) micrographs is displayed in Fig. 4.9. Fig. 4.9(a) shows the TEM BF microstructure of 0Al steel deformed to its failure strain revealing that its deformation microstructure comprises of the deformation bands and dislocations. Fig. 4.9(b) shows the selected area electron diffraction pattern (SAED) of the area in Fig. 4.9(a). In the SAED, diffraction spots of the austenite are spread into streaks, whereas the spots originated from deformation bands appeared as a distinct set of intensity maxima and which can be indexed as hcp structure,  $\epsilon$ -martensite. The occurrences of  $\epsilon$ -martensite in bands in the microstructure also substantiate the findings of Rietveld refinement plotted in Fig. 4.2(c). It is well known that  $\epsilon$ -martensite acts as effective obstacles to dislocations (Benzing *et al.*, 2018) and leads to a high SHR in the case of 0Al steel, as was observed in Fig. 4.1(b).

The TEM BF microstructure acquired along [110] zone axis in Fig. 4.9(c) and its corresponding SAED pattern in Fig. 4.9(d) indicate the presence of fine twin bundles in the deformation microstructure of 1Al steel, which is also consistent with the XLPAs findings of high twin fault probability in this steel (Table 4.3 and Fig. 4.7(b)). It is well accepted that existences of twin in deformation microstructure provides excellent strength-ductility combination (Bouaziz *et al.*, 2011; De Cooman *et al.*, 2018). This was also observed in case of 1Al steel (Fig. 4.1(a)). Interestingly, Fig. 4.9(e) shows that dislocation tangles and dislocation walls are prominent in the deformation microstructure of 3Al steel without presences of martensite and twins, in consistent with the SAED pattern presented in Fig. 4.9(f). The cell structure, i.e., dislocation walls and a region of low dislocation density, noticeable in Fig. 4.9(e), are essentially a consequence of dynamic recovery that occurred before fracture. This indicates reduced dislocation density, which is in agreement with the findings of XLPAs (Table

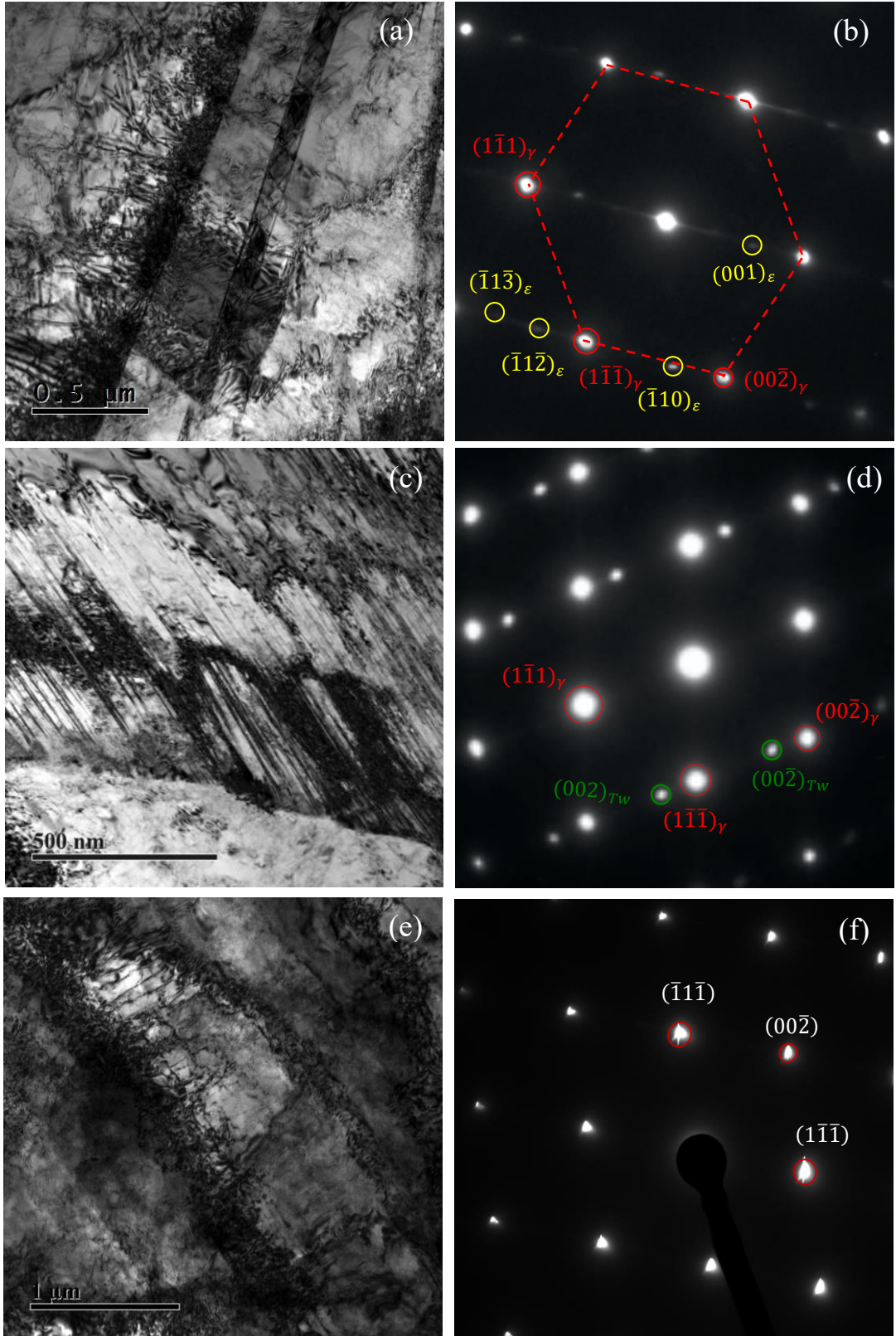


Fig. 4.9: Bright field transmission electron microscope micrographs of the fractured specimens: (a) 0Al steel, along  $B \approx [110]_\gamma \parallel [11\bar{2}0]_\varepsilon$ . (c) 1Al steel, along  $B \approx [110]_\gamma$ . (e) 3Al steel, along  $B \approx [110]_\gamma$ . The corresponding SAD pattern of (a), (c) and (e) are presented in (b), (d) and (f), respectively.

4.3). A further implication of the presence of recovery in 3Al steel also explains the higher value of the Wilkens parameter in Table 4.3, as was discussed in before in Section 4.3.1.

In hindsight, the distinctly different TEM microstructures shown in Fig. 4.9 are a consequence of the different deformation mechanisms activated in these steels. This can be understood in terms of the effective SFE of the steels obtained from XLPA (Table 4.3). In agreement with Allain *et al.* (2004),  $\gamma \rightarrow \varepsilon$  transformation and TWIP effect was observed for 0Al and 1Al steel having SFE value  $18.1 \text{ mJm}^{-2}$  and  $25.7 \text{ mJm}^{-2}$ , respectively. Additionally, the strain hardening responses observed in Fig. 4.1(b) could also be qualitatively understood in terms of obtained SFE values listed in Table 4.3. Kim *et al.* (2018) predicted that TWIP steels having low SFE shows high strain hardening rate due to limited dynamic recovery in addition to martensite formation, and which is also observed in this study in the steel 0Al.

#### 4.4.2 The effect of $\gamma \rightarrow \varepsilon$ transformation on strain hardening

The active deformation mechanism in high-Mn steels can comprise of slip, twinning and strain-induced martensite formation and that they can lead to quite complex deformation mechanisms as more than one mechanism could come into play either individually or collectively - wherein, the SFE plays an important role towards the selection of deformation mechanism(s) (De Cooman *et al.*, 2018). However, the irony is that the range of SFE that demarcates the individual deformation mechanisms is still not well-defined and notwithstanding the SFE map proposed by Kim and De Cooman (2016), it is more or less accepted that  $\gamma \rightarrow \varepsilon$  transformation is preferred when SFE is  $\leq 20 \text{ mJ/m}^2$ . A single isolated SF namely, intrinsic SF when arranged on every alternate  $\{111\}$  austenite planes in a non-localized manner produces hcp  $\varepsilon$ -martensite (De Cooman *et al.*, 2018). Although SFE is an important parameter in observing hcp  $\varepsilon$ -martensite within the austenite matrix; their growth as well as the morphology is strongly controlled by the austenite grain size and the  $\gamma \rightarrow \varepsilon$  transformation proceeds easily within larger austenite grains (Olson & Cohen, 1976).

A set of BF TEM micrographs revealing the growth of  $\varepsilon$ -martensite in 0Al steel at fracture strain are displayed in Fig. 4.10. A  $\lambda$ -like morphology formed by branching of the  $\varepsilon$  plates is clearly discernible in Fig. 4.10(a). In contrast, Fig. 4.10(b) reveals the microstructure with mutually intersecting  $\varepsilon$  plates developed in a direction parallel to (111) plane and the corresponding selected area electron diffraction (SAED) pattern is presented in the lower inset. According to Takaki *et al.* (1993) when an  $\varepsilon$  plate is formed by accumulating a lot of SFs, the stress at the tip of the growing plate also increases with increasing width of the plate and after

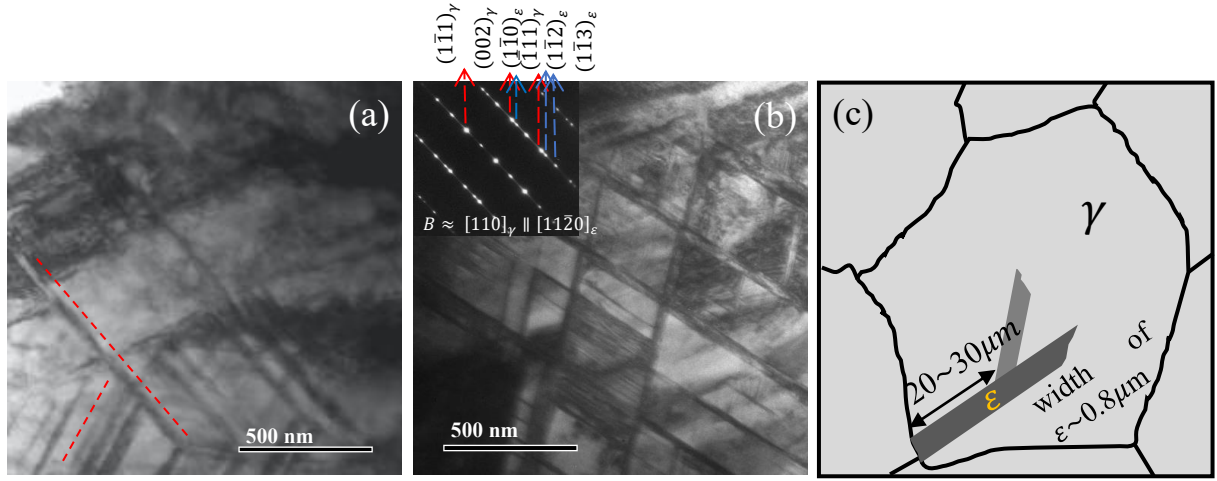


Fig. 4.10: BF micrographs along  $B \approx [110]_{\gamma} \parallel [11\bar{2}0]_{\epsilon}$  representing  $\epsilon$ -martensite formation in 0Al steel at fracture strain: (a)  $\lambda$ -like morphology formed by branching of  $\epsilon$  plates is delineated using dotted red lines (b) mutually intersecting  $\epsilon$  plates at fracture strain. (c) A schematic representation of  $\epsilon$ -martensite formation morphology in austenite grain.

a certain width  $\sim 0.8 \mu\text{m}$  a new plate is formed that grows in a direction parallel to  $\{111\}_{\gamma}$  - in order to minimize the stress field at the tip of the plate. The branching of the  $\epsilon$  plate as schematically shown in Fig. 4.10(c) is known to occur above a critical length of the plate ( $20\sim 30 \mu\text{m}$ ) (Takaki *et al.*, 1993) and the  $\gamma \rightarrow \epsilon$  transformation is greatly suppressed when the austenite grain size is below  $\sim 30 \mu\text{m}$  (Takaki *et al.*, 1993). However, the 0Al steel had a grain size above  $30 \mu\text{m}$  with a corresponding SFE  $\sim 18.1 \text{ mJ/m}^2$  and thus both these parameters should incite profound  $\gamma \rightarrow \epsilon$  transformation in this steel - as was observed in Fig. 4.9(a) and also supported by Rietveld analysis (1969) of the XRD pattern estimating 35%  $\epsilon$ -martensite (Fig. 4.2(c))

The lattice parameters estimated from the Rietveld analysis (1969) for 0Al steel were  $c=4.1036\text{\AA}$  and  $a=2.5389\text{\AA}$  for  $\epsilon$ -martensite, while the corresponding austenite lattice parameter was  $a=3.6061\text{\AA}$ . Accordingly, the austenite unit cell volume is calculated as  $0.0469 \text{ nm}^3$  with an average volume occupied by an Fe atom:  $0.0117 \text{ nm}^3$ , while the same parameters for  $\epsilon$ -martensite are:  $0.0229 \text{ nm}^3$  and  $0.0114 \text{ nm}^3$ , respectively. Therefore, as newer  $\epsilon$ -martensite are formed in the matrix, the adjacent austenite is subjected to extra tensile stress so as to maintain the macroscopic volume at constant and this would lead to higher strain hardening in 0Al alloy due to the presence of  $\epsilon$ -martensite (Sahu *et al.*, 2007). This hypothesis is in reasonable agreement with the strain hardening behavior of the steels observed in Fig. 4.1(b) and discussed under Section 4.1.2.

## 4.5 Critical shear stress for twinning & prediction of deformation map

### 4.5.1 SFE dependent critical shear stress of twinning and stacking fault widths

**Table 4.4:** Burger vector of Shockley partial and shear stress values of the steels.

Steel code	0Al	1Al	3Al
Burger vector of the Shockley partial ( $b_p$ ) (nm)	0.1472	0.1476	0.1482
Critical shear stress of twinning ( $\tau_c$ ) (MPa)	246	348	561
Maximum shear stress (MPa)	689	736	613

Table 4.4 summarizes the maximum possible shear stress experienced by the steels, as well the critical shear stress ( $\tau_c$ ) of twinning for observing infinitely wide SFs *i.e.* for observing twinning (Byun, 2003). The values of the maximum possible shear stress were calculated from the UTS values by considering the maximum possible Schmid factor 0.5; assuming maximum stress concentration condition. The  $\tau_c$  reported in Table 4.4 is calculated considering that the SF widths diverge in most favorably orientated slip system (Byun, 2003), corresponding to the following condition:

$$\tau_c = \frac{2 \times \text{SFE}}{b_p} \quad (4.1)$$

where,  $b_p = \frac{a}{\sqrt{6}}$ , is the magnitude of Burgers vector of the Shockley partials, determined from Rietveld analysis (1969). The SFE map proposed by Kim and De Cooman (2016) for such steel predicts simultaneous incidence of twinning and  $\gamma \rightarrow \varepsilon$  transformation until the SFE limit  $\sim 13$  mJ/m<sup>2</sup>, while they reckon intense twinning in the SFE range: 13-40 mJ/m<sup>2</sup> and dislocation plasticity predominates above  $\sim 40$  mJ/m<sup>2</sup>.

In this study, the SFE map (Kim & De Cooman, 2016) was violated for 0Al steel since  $\gamma \rightarrow \varepsilon$  transformation was observed even though its SFE was  $\sim 18$  mJ/m<sup>2</sup> (Figs. 4.2(c) and 4.9(a)). The SFE also governs the width of SFs under a stress-free condition, and the widths change under the influence of external stress. Therefore, the deformation mechanism(s) in high-Mn steels should be directly related to the width of austenite SFs as function of external shear stress. Thus, the expected width ( $w$ ) of the SFs in the studied steels are calculated based on their dependence on external resolved shear stress ( $t$ ) as (Byun, 2003):

$$w = \frac{Gb_p^2}{\pi(2 \times \text{SFE} - \tau b_p |\sin \theta_2 - \sin \theta_1|)} \left( \cos \theta_1 \cos \theta_2 + \frac{\sin \theta_1 \sin \theta_2}{1 - \vartheta} \right) \quad (4.2)$$

where,  $G=72$  GPa is shear modulus of the steel, assumed not to vary significantly with composition (Pierce *et al.*, 2014),  $\theta_1$  and  $\theta_2$  are angles between Burgers vectors of the leading and trailing partials, assumed as  $-30^\circ$  and  $+30^\circ$ , respectively and  $\vartheta$  is the Poisson's ratio  $\sim$



0.24. The shear stress values thus calculated for highest possible Schmid factor 0.5 are summarized in Table 4.4. The variation in width of SFs with external shear stress predicted according to Eq. (4.2) is presented in Fig. 4.11(a) for different SFE values.

The  $\tau_c$  values in Table 4.4 estimated using XRD SFE values according to Eq. (4.1) represent an increasing nature with Al content, which in other words marks a waning of twinning tendency due the rise in SFE with Al addition. In agreement, Lai *et al.* (2021), in a

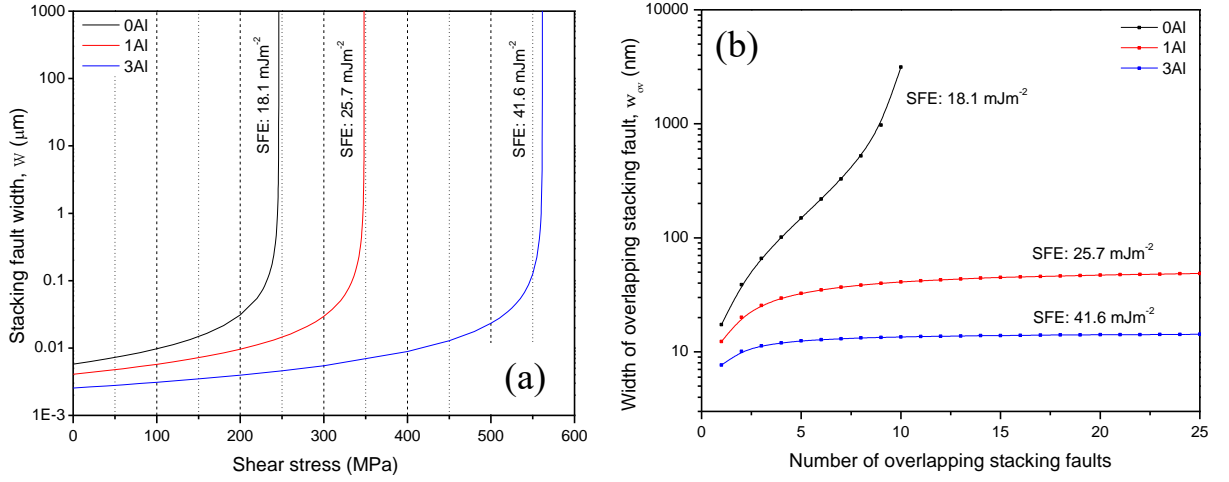


Fig. 4.11: (a) The variation of austenite stacking fault widths with external stress for different SFE values. (b) The variation in the overlapping stacking faults' width with the number of overlaps.

recent report involving a lightweight Fe-Mn-Al-Si-C steel have observed that when the SFE is low, the classical mechanism of twinning is selected, while for high SFE cases, the stress for triggering a SF emission is hardly reached before fracture, so that the deformation twinning is largely suppressed. In other words, this has the implication that overlapping of SFs can easily sustain on austenite  $\{111\}$  planes in 0Al and 1Al steels, while the situation is not that conducive for 3Al. This justification is now further tested using Talonen and Hänenen (2007) approach involving equilibrium width of overlapping SFs ( $w_{ov}$ ) on the number of overlapping SFs ( $N$ ):

$$w_{ov} = \frac{Ngb_p^2}{2\pi(N(SFE - 2\sigma^{\gamma/\varepsilon}) + 2\sigma^{\gamma/\varepsilon})} \left[ \frac{3}{4} - \frac{1}{4(1-\nu)} \right] \quad (4.3)$$

wherein,  $\sigma^{\gamma/\varepsilon}$  is the energy of austenite/ $\varepsilon$ -martensite interface, approximated as  $\sim 10 \text{ mJ/m}^2$  (Wang & Wan, 1990). The calculation of Eq. (4.3) was repeated using XRD SFE values in Table 4.3 and the results are plotted in Fig. 4.11(b). Intriguingly, it turns out that the width,  $w_{ov}$  diverges in case of 0Al steel having SFE  $\sim 18.1 \text{ mJ/m}^2$ , and  $\varepsilon$ -martensite formation is preferred over twinning in such cases (Talonen & Hänenen, 2007). At the same time, Fig.

4.11(b) also indicates that  $w_{ov}$  slowly increases for first few SFs in 1Al steel with SFE  $\sim 25.7$  mJ/m<sup>2</sup> *i.e.* this situation would incite twinning, while  $w_{ov}$  remains nearly constant for 3Al - not even reaching 10 nm. In other words, the situation in 3Al is too restrictive for observing any twinning opportunity. Therefore, dislocation plasticity should be promoted in dearth of twinning (De Cooman *et al.*, 2018; Riaz *et al.*, 2021). This hypothesis is reasonably supported through the TEM investigations presented and discussed in Fig. 4.9 and Section 4.4.1 respectively.

#### 4.5.2 The critical shear stress for twinning based deformation regime

Twin initiation in fcc crystals requires a minimum stress, known as the critical stress of twinning (Hirth & Lothe, 1982) and a detailed account of the effect of SFE on the critical stress of twinning in different alloys systems are proposed (Naeita & Takamura, 1974; Meyers *et al.*, 2001; Steinmetz *et al.*, 2013; Diao *et al.*, 2017) that these activities require accurate estimation/prediction of SFE. Fig. 4.12 schematically summarizes the deformation picture of the studied Fe-Mn-Al-C steels in terms of the respective critical shear stress for twinning computed in Table 4.4 on the basis of Eq. (4.1). Moreover, the dotted red vertical lines in Fig. 4.12 delineate the SFE boundary for twinning and the mixed occurrence of twinning and  $\epsilon/\alpha'$  martensitic transformation in Fe-Mn-Al-C steels, based on the report of Kim and De Cooman (2016). It was observed in Table 4.4 that the estimated values of  $\tau_c$  for 0Al and 1Al steels are distinctly lower than their respective maximum shear stress values, while they are quite comparable in 3Al steel. This was also supported in Fig. 4.11(a), which revealed that for a

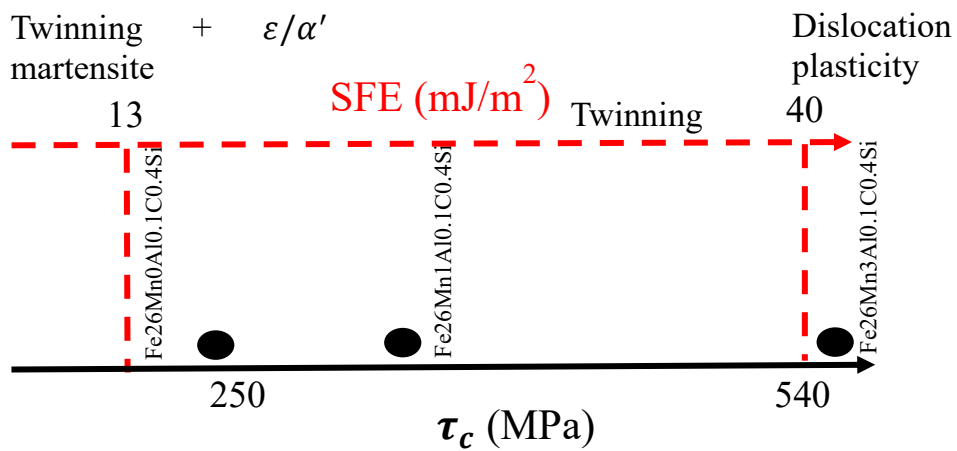


Fig. 4.12: Schematic representation of critical shear stress for twinning based deformation regime. Red dotted vertical lines delineate the SFE dependent deformation regimes proposed by Kim and De Cooman (2016).

relatively low critical shear stress values ( $\sim 250\text{-}350$  MPa) the SFs would diverge on the  $\{111\}$  planes and twinning should be observed according to Eq. (4.1).

If the overlapping of SFs take place on alternate  $\{111\}$  planes,  $\varepsilon$ -martensite is observed, while a twin is observed when those SFs overlap on successive  $\{111\}$  planes (Bouaziz *et al.*, 2011; De Cooman *et al.*, 2018). In other words, the chances of finding  $\varepsilon$ -martensite and/or twinning appears higher in 0Al and 1Al since these two steels have respective  $\tau_c = 246$  and 348 MPa, and they are being significantly lower than the corresponding maximum shear stress values of the steels as: 689 and 736 MPa, respectively (Table 4.4). On the other hand, the occurrence of twinning is not favored in the 3Al steel since its  $\tau_c \sim 561$  MPa is quite comparable to maximum shear stress experienced by the steel  $\sim 613$  MPa (Table 4.4). Additionally, it is reminisced that deformation twinning and Taylor lattice were the respective highlighting aspects of 1Al and 3Al steels' microstructure (Figs. 4.9(c) and (e)) and interestingly, both these features are consequences of planar slip activated by different dislocation activities, while Taylor lattice is generally observed in high SFE steels (Das *et al.*, 2021; Lai *et al.*, 2021).

The presence of numerous twin bundles along Taylor lattice boundaries in Fe-Mn-Al-Si-C steel is observed and that they both collectively contribute to a high strain hardening rate above  $\sim 2$  GPa (Lai *et al.*, 2021). Thus, the 3Al steel in the present study, revealing prominent Taylor lattice without any recognizable deformation twins clearly shows a strain hardening rate lower than  $\sim 2$  GPa (Fig. 5.1(b)). In agreement, Das *et al.* (2021) previously observed that a twin deficient high-Mn steel can hardly surpass a strain hardening rate  $\sim 2$  GPa, while Riaz *et al.* (2021) noted a strain hardening rate above  $\sim 2$  GPa due to simultaneous contributions from Taylor lattice and deformation twinning. Nevertheless, the respective  $\tau_c$  values of the studied steels are indicated in Fig. 4.12 as black circles on the deformation regime map conceived by Kim and De Cooman (2016) and also reveal that the position of  $\tau_c$  for 0Al violate the prediction of SFE based deformation map proposed by Kim and De Cooman (2016), while the other two steels (1Al and 3Al) are in good agreement with their prediction. In hindsight, the present study could indicate that an SFE based critical shear stress of twinning approach seems a better alternative than predicting SFE dependent deformation of high-Mn steels.

## References

- Allain, S., Chateau J. P., Bouaziz, O., Migot, S. & Guelton N. (2004). *Mater.Sci. Eng. A*. **387-389**, 158-162.
- Balogh, L., Ribarik, G. & Ungar, T. (2006) *J. Appl. Phys.* **100**, 023512(1-10).

- Benzing, J.T., Poling, W.A., Pierce, D.T., Bentley, J., Findley, K.O., Raabe, D., Wittig, J.E. (2018) *Mater. Sci. Eng. A* **711**, 78-92.
- Bouaziz, O., Allain, S., Scott, C., Cugy, P., Barbier, D. (2011) *Curr. Opin. Solid. St. M.* **15**, 141-168.
- Byun, T.S. (2003) *Acta Mater.* **51**, 3063-3071.
- Cottrell, A. H. (1953) *Phil. Mag.* **44**, 829-832.
- Das, S.R., Shyamal, S., Shee, S.K., Kömi, J.I., Sahu, P. (2021) *Mater. Charact.* **172**, 110833.
- Das, S.R., Shyamal, S., Sahu, T., Kömi, J.I., Chakraborti, P.C., Porter, D.A., Karjalainen, L.P., Sahu, P. (2021) *Materialia* **15**, 101042.
- Dastur, Y.N., Leslie, W.C. (1981) *Metall. Mater. Trans. A* **12**, 749-759.
- De Cooman, B. C., Estrin, Y., Kim S.K. (2018) *Acta Mater.* **142**, 283-362.
- Dey, S. N., Chatterjee, P. & Sen Gupta, S. P. (2005). *Acta. Mater.* **53**, 4635-4642.
- Diao, H.Y., Feng, R., Dahmen, K.A., Liaw, P.K. (2017) *Curr. Opin. Solid State Mater. Sci.* **21**, 252-266 253.
- Dumay, A., Chateau, J.-P., Allain, S., Migot, S., Bouaziz, O. (2008) *Mater. Sci. Eng. A* **483-484**, 184-187.
- Enzo, S., Fagherazzi, G., Benedetti, A., Polizzi, S. (1988) *J. Appl. Cryst.* **21** 536-542.
- Hamada, A.S., Karjalainen, L.P., Somani, M.C. (2007) *Mater. Sci. Eng. A* **467**, 114-124.
- Hull, D., Bacon, D. J. (2011) *Introduction to Dislocations*, Fifth Edition, Butterworth-Heinemann, Oxford.
- Jeong, J.S., Woo, W., Oh, K.H., Kwon, S.K., Koo, Y.M. (2012) *Acta Mater.* **60**, 2290-2299.
- Jin, J.-E., Lee, Y.-K. (2012) *Acta Mater.* **60**, 1680-1688.
- Kim, J.K., De Cooman, B.C. (2016) *Mater. Sci. Eng. A* **676**, 216-231.
- Kim, J.K., Estrin, Y., De Cooman, B.C. (2018) *Metal. Mater. Trans. A* **49**, 5919-5924.
- Lai, Z.-H., Sun, Y.-H., Lin, Y.-T., Tu, J.-F., Yen, H.-W. (2021) *Acta Mater.* **210** 116814.
- Lee, Y.K., Choi, C. (2000) *Metall. Mater. Trans. A* **31**, 355-360.
- Lutterotti, L. (2006) MAUD, version 2.038; <<http://www.ing.unitn.it/~luttero/maud>>
- Mahato, B., Shee, S.K., Sahu, T., Ghosh Chowdhury, S., Sahu, P., Porter, D.A. & Karjalainen, L.P. (2015) *Acta Mater.* **86**, 69-79.
- Meyers, M. A., Vöhringer, O., Lubarda, V. A. (2001) *Acta mater.* **49**, 4025-4039.

- Naeita, N., Takamura, J. (1974) *Philosophical Magazine*, **29:5**, 1001-1028.
- Olson, G. B. & Cohen, M. (1976) *Metall. Trans. A*, **7**, 1897-1904.
- Peng, X., Zhu, D.-Y., Hu, Z.-M., Wang, M.-J., Liu, L.-L. & Liu, H.-J. (2014) *J. Iron Steel Res. Int.* **21**, 116-120.
- Pierce, D.T., Jimenez, J. A., Berntley, J., Raabe, D., Oskay C. & Witing, J.E. (2014). *Acta Mater.* **68**, 238-253.
- Riaz, T., Das, S.R., Sahu, T., Chakraborti, P.C., Sahu, P. (2021) *Mater. Lett.* **282**, 128691.
- Rietveld, H. M. J. (1969) *Appl Cryst.* **2**, 65-71.
- Saeed-Akbari, A., Imlau, J., Prahl, U. & Bleck, W. (2009) *Metall. Mater. Trans. A*, **40**, 3076-3090.
- Sahu, P., Shee, S.K., Hamada, A.S., Rovatti, L., Sahu, T., Mahato, B., Ghosh Chowdhury, S., Porter, D.A., Karjalainen, L.P. (2012) *Acta Mater.* **60**, 6907-6919.
- Sahu, P., Hamada, A.S., Ghosh, R.N., Karjalainen, L.P. (2007) *Metal. Mater. Trans. A*, **38**, 1991-2000.
- Schramm, R.E. & Reed, R.P. (1975). *Metall. Trans. A*, **6**, 1345-1351.
- Sidor, J.J., Chakravarty, P., Bátorfi, J.G., Nagy, P., Xie, Q., Gubicza, (2021) *J. Metals* **11(10)** 1571.
- Steinmetz, D. R., Japel, T., Wietbrock, B., Eisenlohr, P., Gutierrez-Urrutia, I., Saeed-Akbari, A., Hickel, T., Roters, F., Raabe, D. *Acta mater.* (2013) **61** 494-510 495.
- Takaki, S., Nakatsu, H., Tokunaga, Y. (1993) *Mater. Trans. JIM* **34**, 489-495.
- Talonen, J., Hänninen, H. (2007) *Acta Mater.* **55**, 6108-6118.
- Tian, X., Li, H., Zhang, Y. (2008) *J Mater. Sci.* **43**, 6214-6222.
- Ungár, T. (2003) *Adv. Eng. Mater.* **5(5)**, 323-329.
- Ungar, T., Borbely, A. (1996) *Appl. Phys. Lett.* **69**, 3173-3175.
- Ungár, T., Ott, S., Sanders, P. G., Borbely, A., Weertman, J R. (1998) *Acta Mater.* **46**, 3693-3699.
- Wilkins, M., in Fundamental Aspects of Dislocation Theory, J. A. Simmons, R. de Wit, R. Bullough Eds., Vol. II, Natl Bur. Stand. Publ., Washington, 1970, pp. 1195-1221.
- Warren, B. E. (1969). *X-ray diffraction*, Addison-Wesley, Reading, Mass.
- Wang, W.S., Wan, C.M. (1990) *J. Mater. Sci.* **25**, 1821-1823.
- Zambrano, O.A. (2016) *J. Eng. Mater. Technol.* **138(4)**, 041010.
- Zuidema, B.K., Subramanyam, D.K., Leslie, W.C. (1987) *Metall. Trans. A* **18**, 1629-1639.



# *Chapter 5\**

*Deformation microstructure study  
of Fe-30Mn-3Si-3Al Steel under  
tensile and compressive loading*

\* This chapter is unpublished.





## 5.1 Material processing & the flow stress behavior

### 5.1.1 Material and experimental

The steel utilized in this study has the chemical composition Fe-30Mn-3Si-3Al (all concentrations in wt%) and was manufactured by melting and casting as a 5 Kg ingot in a vacuum induction furnace. The ingot was then homogenized for 4 hours at 1100°C in an Ar environment to eliminate the segregation of various elements, primarily Mn. The homogenized sample was then divided into two pieces and hot rolled in a hot rolling mill to form 3.6 mm and 11 mm thick bands followed by solution treatment at 1100°C for 30 minutes under argon environment and quenched into water to reach room temperature.

A cylindrical sample measuring 8 mm in diameter and 10 mm in length was machined from an 11 mm thick heat-treated band for the axisymmetrical compressive test. The test was carried out on a Gleeble 1500 thermo-mechanical simulator at a constant true strain rate ( $\sim 10^{-3} \text{ s}^{-1}$ ). For tensile test tensile testing specimens with the gauge section of 3.4 mm in thickness, 38 mm in length and 6.25 mm in width was machined from the 3.6 mm thick band and the machined sample was then utilized

for tensile test that was conducted uniaxially at room temperature in a Zwick Z 100 tensile testing machine (Zwick Roell, GmbH). The specimens machined from the thick bands for tensile and compression tests are shown schematically in Fig. 5.1. Tensile tests were performed with a very low strain rate ( $\sim 10^{-3} \text{ s}^{-1}$ ) to prevent the adiabatic heating which might alter the stacking fault energy of the steel. Both tension and

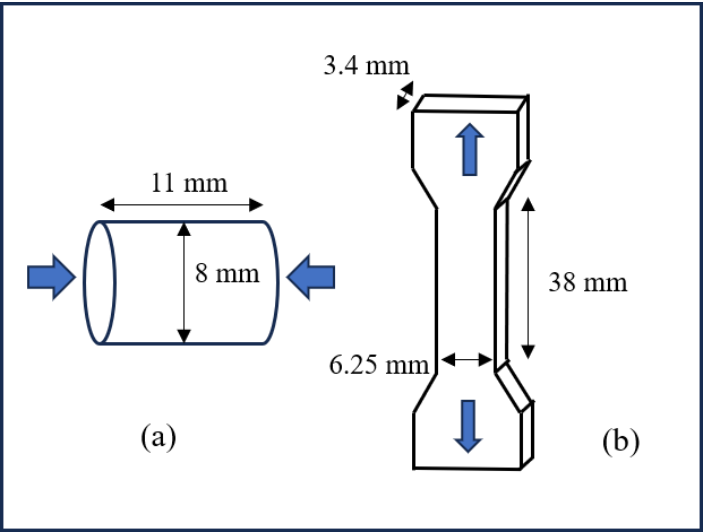


Fig. 5.1: Schematic diagram showing specimens for (a) compression (b) tension test.

compression tests were interrupted at true plastic strains of  $\sim 5\%$ ,  $\sim 40\%$ , and  $\sim 67\%$ , where  $\sim 67\%$  regarded as the highest imposed strain under compression for an even comparison with the fracture strain in the tensile specimen.

X-ray line profile analysis and TEM micrographs were used to investigate the microstructures of the specimens at each interrupted strain. The X-ray line profiles of samples deformed by both compression and tension were obtained using a Bruker D-8 Advanced

powder diffractometer in the angular range  $40^\circ$  to  $100^\circ$  with monochromatic Cu-K $\alpha$  radiation with step size  $0.02^\circ$ . For the observation of deformed microstructure through TEM, disks of size 3 mm were cut from the gauge length of deformed grinded mechanically polished sample of thickness  $\sim 100\text{ }\mu\text{m}$  and the cut sample was then electropolished using a solution of 90% methanol and 10% perchloric acid with Tenupol-5 and finally the electropolished sample was used to observe the microstructures at interrupted strain for the deformed sample through JEOL 2200FS transmission electron microscope.

### 5.1.2 Tensile and compressive behavior

True stress-strain ( $\sigma - \epsilon$ ) response of the studied steel under tension and compression is depicted in Fig. 5.2(a) - corresponding to a yield strength  $\sim 210\text{ MPa}$  under tension, while no clear yield point could be estimated in case of compression test, rather a continuous curve is observed. The specimen under compression could be compressed even beyond a true plastic strain of 100%, and thus the compressive curve is shown only up to the fracture strain of tensile tested specimen ( $\sim 67\%$ ), for better comparison. According to Grässel *et al.* (2000), value of tensile yield strength and the ultimate tensile strength for Fe-30Mn-3Si-3Al 1 steel are respectively  $\sim 250\text{ MPa}$  and  $\sim 615\text{ MPa}$ , hence it is considered to be a low strength steel. Difference in the flow curves of the studied steel during tensile and compressive loading is clearly evident in Fig. 5.2(a) from the onset of straining and that the flow curves coincide at 8% of strain, while the difference becomes more pronounced at higher strains - leading to a significant asymmetry in true stress-strain curves. A smooth transition from elastic to plastic region in true stress-strain curve of tensile tested sample in Fig. 5.2(a) refers to the absence of any dislocation induced Lüders band formation at the very beginning of plastic region. The absence of any serrated flow behavior over the entire regime suggests that no dynamical strain aging (DSA) phenomenon occurred, which is often undesirable in this type of high-Mn steel (De Cooman *et al.*, 2018).

The strain hardening rate ( $d\sigma/d\epsilon$ ) plotted in Fig. 5.2(b) obtained from the derivation of the stress-strain curves in Fig. 5.2(a) reveals an unusual nature of the strain hardening behavior of the steel, which is normally uncommon in this type of steel and that after a rapid initial decrement, steel shows almost no strain hardening rate ( $< 20\text{ MPa}$ ) throughout the tensile and compressive deformation regime. A very high rate of strain hardening ( $\sim 2\text{ GPa}$ ) is observed at the onset of plastic deformation for tensile tested specimen which decreases rapidly and reaches  $\sim 20\text{ MPa}$  just after  $\sim 1\%$  increase of true plastic strain, whereas compressed

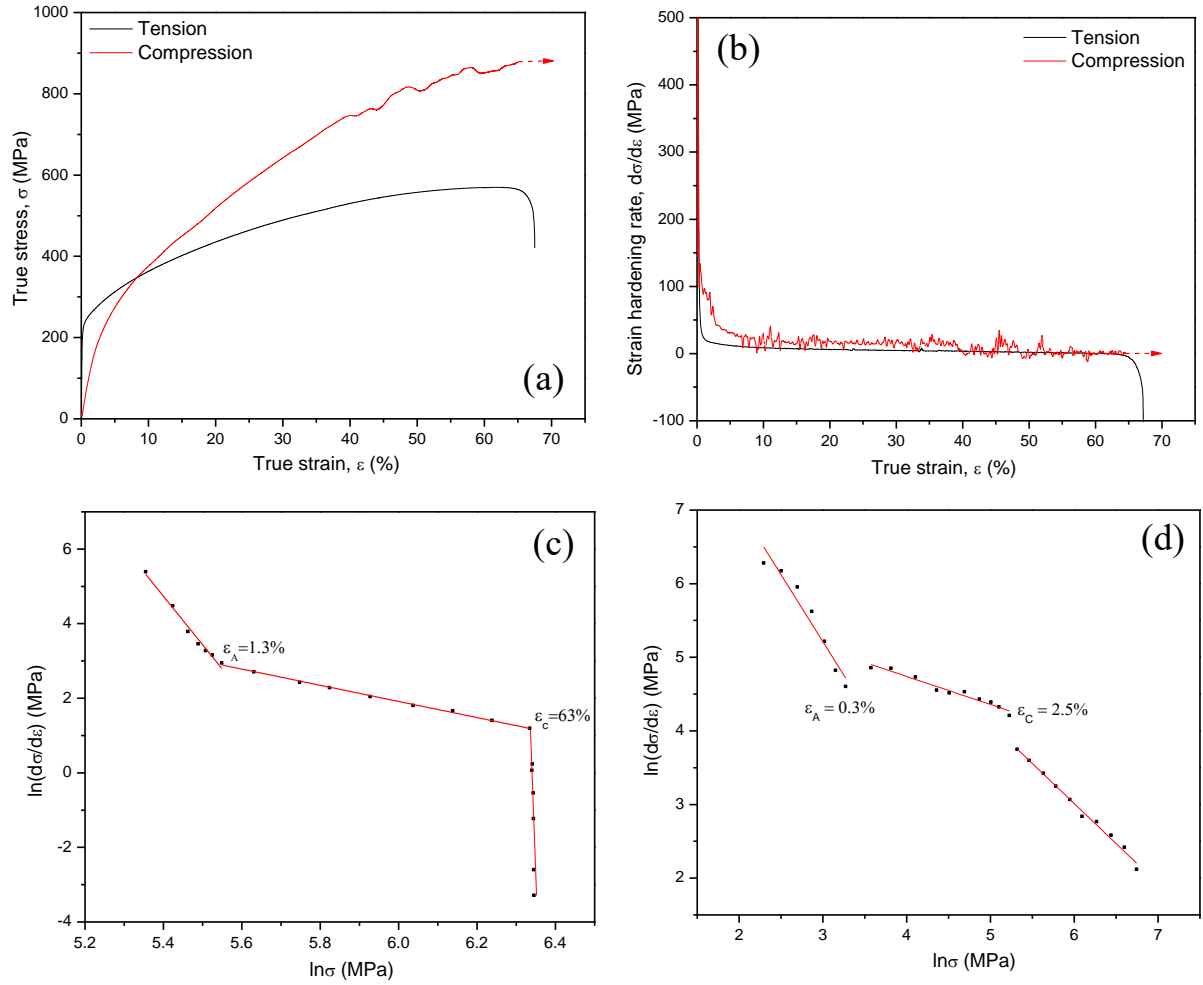


Fig. 5.2: (a) True stress-strain ( $\sigma - \epsilon$ ) (b) strain hardening plot ( $d\sigma/d\epsilon - \epsilon$ ) under tensile and compressive loading.  $\ln(d\sigma/d\epsilon) - \ln\sigma$  plot for modified C-J analysis (c) tension (d) compression.

specimen shows comparatively lower strain hardening rate ( $\sim 500$  MPa) at the initiation of plastic deformation. A substantial difference was also seen in the strain hardening plot, similar to the tensile and compressive response curves: the compression tested sample demonstrated a significantly greater strain hardening rate than the tensile tested sample up to 8% of true strain. Despite the presence of significant asymmetry in Fig. 5.2(a) it is seen that both the tensile and compressive steels follow a nearly symmetric path in their strain hardening rate plots (Fig. 5.2(b)).

The strain hardening behavior of the studied steel under tension compression is further examined in detail using a modified Crussard-Jaoul (C-J) analysis (Jin & Lee, 2009) - based on the Swift equation (Swift, 1952). For both tensile and compressive hardening, the  $\ln(d\sigma/d\epsilon)$  versus  $\ln\sigma$  plot are displayed in Figs. 5.2(c) and 5.2(d), respectively, having a

slope at various stages being:  $(1 - 1/n)$ , where  $n$  is the strain hardening exponent. A three-stage strain hardening is observed here (Figs. 5.2(c) and 5.2(d), where the first stage i.e., the rapid decrement stage in the strain hardening rate being considered stage A, extending to 1.3% strain for tensile hardening, while for compression loading, the stage A extends up to 0.3% of the strain. With a further increase in strain, the tensile strain hardening rate remains almost constant or slightly decreased until 63% strain, and this stage is commonly interpreted as stage C. In compression, the rapid decrement stage (stage A) was followed by another decrement stage that extends up to 2.5% true strain and is somewhat slower than stage A which can be considered as stage C. Finally, another rapid drop in strain hardening rate till fracture due to the initiation of necking is observed during tensile hardening, which is designated stage E, where in compression no such characteristics could be formed and the final stage is practically constant or slightly decreasing. Stage B and stage D do not appear in this steel, most likely due to the slow rate of mechanical twinning (Jin & Lee, 2012). In general, TWIP steels exhibit four- or five-stages strain hardening (De Cooman *et al.*, 2018), while three-stages of strain hardening have also documented (Jin & Lee, 2009; Riaz *et al.*, 2021).

## 5.2 X-ray diffraction studies of the deformation microstructure

In order to characterize deformed metals and alloys, it is crucial to use X-ray line profile analysis (XLPA), which has the enormous potential to reveal microstructural information through the estimation of dislocation density, crystallite size, faulting propensity, and active slip systems. In the next sections of this chapter, the microstructural characteristics of variously deformed microstructures are assessed using the XLPA method.

### 5.2.1 Influence of strain anisotropy on the Williamson-Hall plots

Scatter in a *conventional* W-H plot is a direct consequence of dislocation-induced anisotropic strain broadening, which is a very acceptable phenomenon that is also reassessed here wherein the values of  $\Delta K$  are defined as the FWHM of both tensile and compressive specimens at different strains, which are plotted as a function of  $K$  and shown in Figs. 5.3(a) and 5.3(b), respectively. A significant scatter of FWHM with the diffraction vector  $K$  in the *conventional* W-H plots, as seen in Figs. 5.3(a) and 5.3(b) again confirms the presence of anisotropic strain broadening induced by dislocation. As a result, a notion of W-H plot modification according to Eq. (2.12) is required to comprehend the idea of anisotropic strain broadening caused by dislocation by using the dislocation contrast factor approach (Ungár *et al.*, 1998).

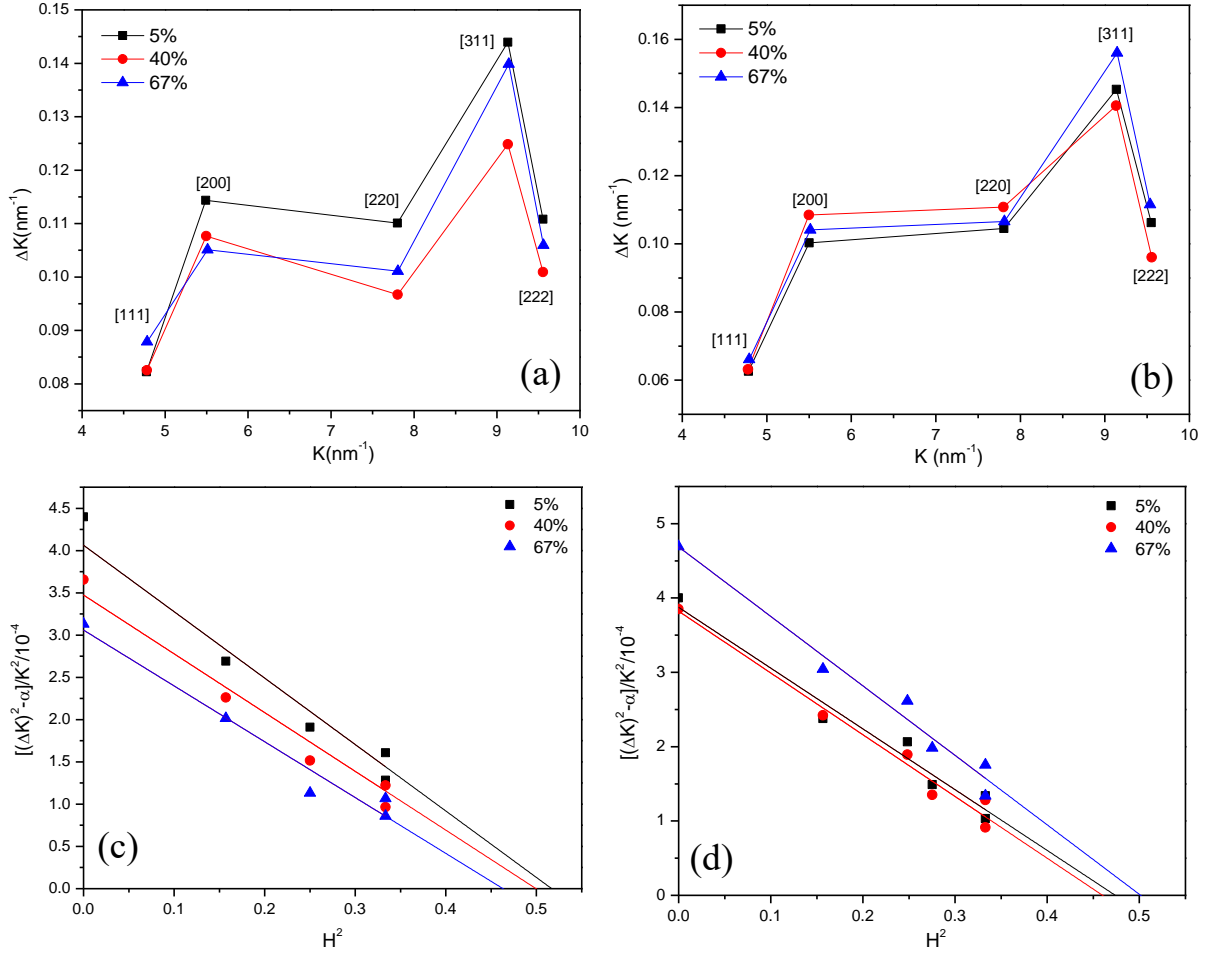


Fig. 5.3: The *conventional* Williamson-Hall plot for (a) tension (b) compression. Linear fitting to the variation of  $[(\Delta K^2) - \alpha]/K^2$  with  $H^2$  according to Eq. (2.16) under (c) tension (d) compression.

We already know that the character of dislocations, as well as their arrangement in the deformation microstructure have a strong influence on the broadening of the diffraction profiles (Sidor *et al.*, 2021) and therefore, it is necessary to determine the dislocation character parameter ( $q$ ), which identifies the nature of dislocations in the austenite microstructure. The  $q$  parameter for the steel loaded through tension and compression is directly estimated at all interrupted strains from the linear fitting plot of Eq. (2.16) presented in Figs. 5.3(c) and 5.3(d) respectively, without any prior assumption about equal presence of  $\frac{a}{2}\langle 110 \rangle$  edge and screw dislocations in the microstructure. The estimated values of  $q$  at each terminal strain of both the tensile and compressive strains are also viewed in Table 5.1. The corresponding  $q$  values of the tensile and compressive samples may be used to determine the population of  $\frac{a}{2}\langle 110 \rangle$  edge and screw dislocations in the microstructure. Then,  $q$  values were further utilized to estimate the average value of contrast factors  $\bar{C}_{hkl}$  according to Eq. (2.14) and also shown in Table 5.1.

For tensile samples, it is seen that,  $\bar{C}_{111}$  decreases gradually with increasing strain, implying a diminishing tendency for dislocation-induced strain anisotropy with increased strain. However, for compressive samples it decreases initially, and then increases as the strain is increased.

**Table 5.1:** Microstructural parameters obtained from X-ray line profile analysis.

True strain	Tension/compression	Lattice parameter (Å)	Contrast factor, $C_{111}$	$q$ parameter	Dislocation density ( $\rho$ ) ( $\text{m}^{-2}$ ) ( $10^{15}$ )	Dislocation outer cut-off radius ( $R_e$ ) nm	Dislocation arrangement parameter ( $M$ )	Stacking fault probability ( $P_{sf}$ ) ( $10^{-3}$ )	Twinning fault probability ( $P_{tw}$ ) ( $10^{-3}$ )	Stacking fault energy ( $\gamma$ ) $\text{mJm}^{-2}$
5%	Tension	0.36262	0.093	1.93	4.6	53.7	3.64	3.3	0.46	43.3
	compression	0.36295	0.078	2.12	2.54	72.8	3.63	2.5	4.1	26.1
40%	Tension	0.36268	0.088	2	3.9	46.9	2.93	3.1	3.7	36.2
	compression	0.36271	0.073	2.17	4.72	50.24	3.45	2.28	3.9	43.6
67%	Tension	0.36261	0.074	2.16	3.7	45.7	2.78	0.85	5.27	89
	compression	0.36268	0.088	2	5.75	45.4	3.44	2.3	7.6	40.8

Significantly smoother curves are obtained when the same FWHM of each Bragg reflection of differently deformed specimens are plotted against  $K^2\bar{C}_{hkl}$  according to Eq. (2.12) and presented in Figs. 5.4(a) and 5.4(b) for tensile tested and compressive sample, respectively. It is evident from the close examination of the normal and *modified* W-H plots for both tensile (Figs. 5.3(a) & 5.4(a)) and compressive sample (Figs. 5.3(b), 5.4(b)) clearly shows that inclusion of dislocation-induced anisotropic strain broadening in XLPAs analyses significantly improves the ability to reproduce the diffraction profiles of the deformed steel specimens. A close comparison of Figs. 5.4(a) and 5.4(b) would nevertheless allow one to draw the

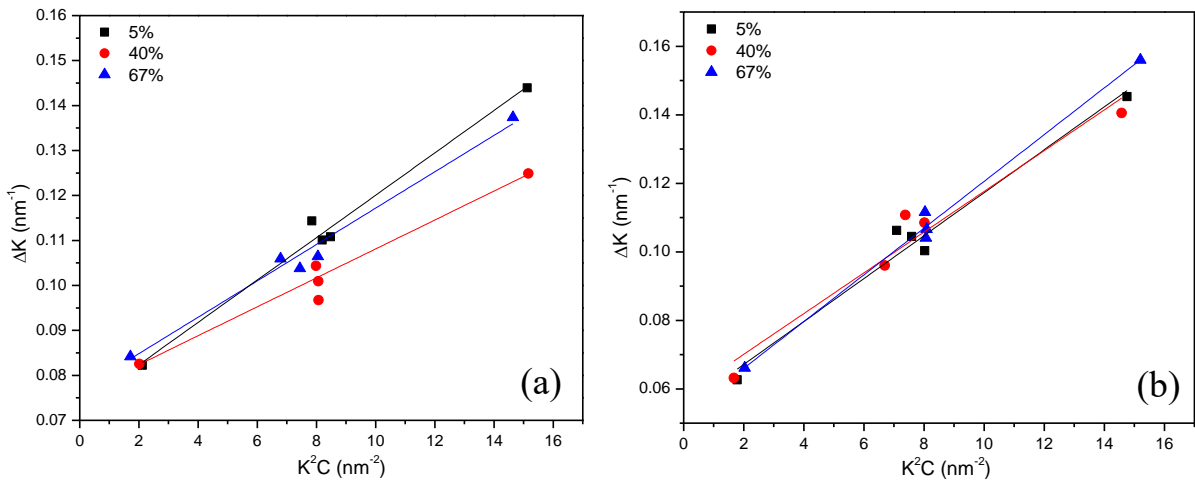


**Fig. 5.4:** The *modified* Williamson-Hall plot under (a) tensile & (b) compressive loading.

conclusion that, notwithstanding some scatter in the FWHMs of the tensile and compressive specimens on *modified* Williamson-Hall plots, the improvement over the corresponding Williamson-Hall plot (Figs. 5.3(a) and 5.3(b)) is quite significant, implicating more reliable microstructural parameters are extracted from the analysis. Although some scatter is observed in Figs. 5.4(a) and 5.4(b), corresponding to fracture strain. It is quite possible that some complex dislocation substructures develop or rearrange in the microstructure at large strain, which is why even the dislocation contrast factor approach fails to model them accurately.

### 5.2.2 Conventional and modified Warren-Averbach analysis

The Fourier coefficients of each Bragg reflection are derived using the Fourier transformation of the experimental intensity distributions, and only the real component of the Fourier

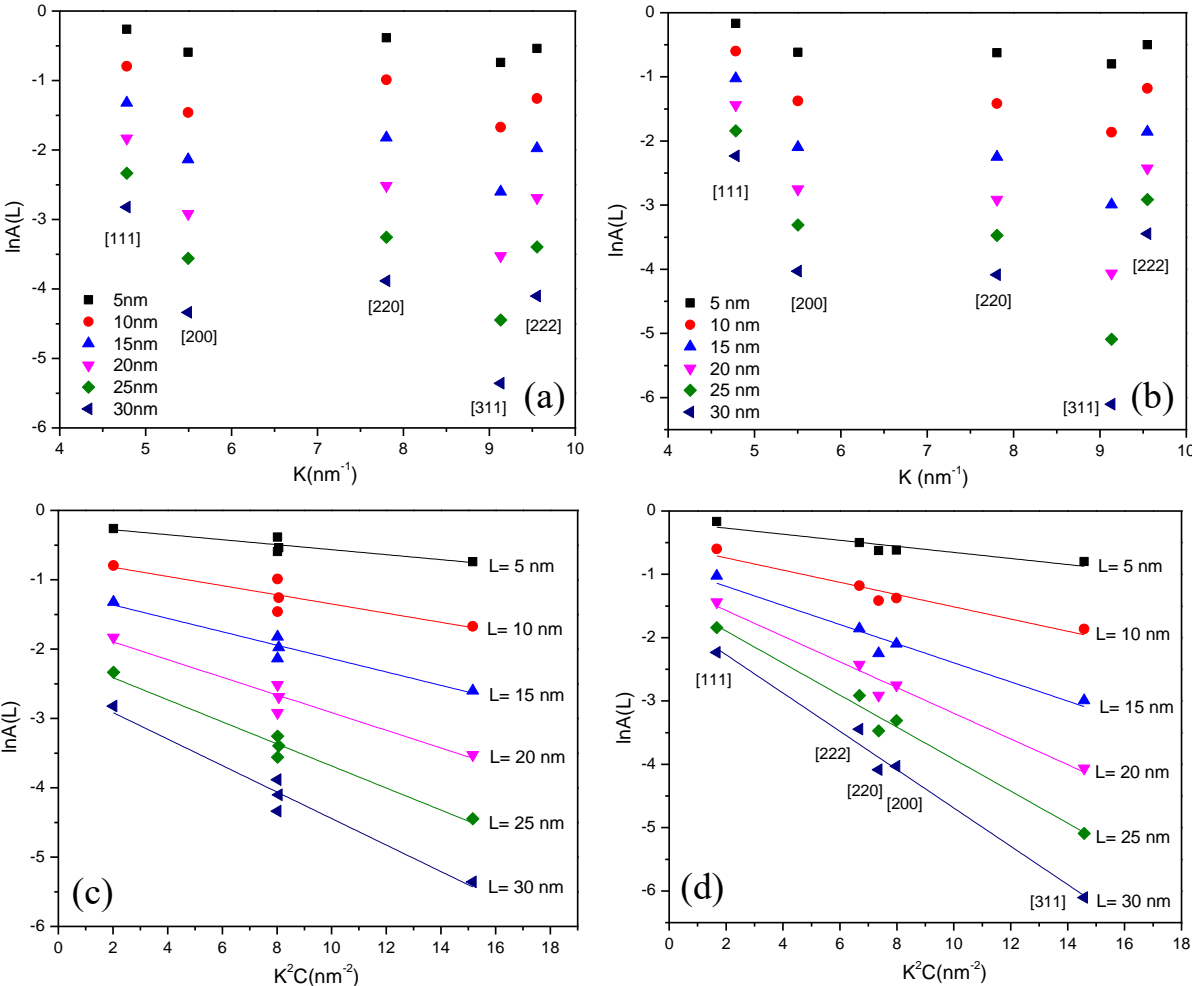


Fig. 5.5: Variation of logarithmic Fourier coefficient,  $\ln A(L)$ , of ~40% of strain at different  $L$  values according to *conventional* Warren-Averbach plot under (a) tensile (b) compressive loading. The *modified* Warren-Averbach plot of (a) and (b) are presented in (c) and (d), respectively.

coefficients,  $A(L)$ , are scaled with  $K^2$  and presented in Figs. 5.5(a) and 5.5(b) for  $\sim 40\%$  strained tensile and compressive specimens respectively. As shown in Figs. 5.5(a) and 5.5(b), both the *conventional* W-A plots reveal significant scatter in their  $\ln A(L)$  vs  $K^2$  plots for different  $L$  values similar to *conventional* W-H plots (Figs. 5.3(a) and 5.3(b)). In contrast, comparatively smoother curves are obtained in Figs. 5.5(c) and 5.5(d), respectively, when the same Fourier coefficients are plotted against  $K^2 \bar{C}$  according to the *modified* W-A equation (Eq. (2.19), where  $\bar{C}$  corresponds to the  $\bar{C}_{hkl}$  which is related to  $\bar{C}_{h00}$  and  $q$  through Eq. (2.14). A comparison between *conventional* W-A plot (Figs. 5.5(a) and 5.5(b)) and *modified* W-A plot (Figs. 5.5(c) and 5.5(d)) highlights the significance of dislocation-induced anisotropic strain broadening in  $\sim 40\%$  strained tensile and compressive steel. It is also evident from Figs. 5.5(c) and 5.5(d) that a linear relationship is maintained in  $\ln A(L)$  vs  $K^2 \bar{C}$  plot for all values of  $L$  until the first four Bragg reflections; therefore, the slope of the linear region is further utilized to estimate the dislocation density and dislocation outer cut-off radius.

### 5.2.3 Evolution of dislocation density and its characteristics during tension and compression

To calculate the dislocation density and dislocation outer cut-off radius of differently deformed tensile and compressive specimen, slopes obtained from the linear portion of the *modified* W-A plot (Figs. 5.5(c) and 5.5(d)) are plotted against  $\ln(L)$  (in Figs. 5.6(a) and 5.6(b) respectively) and fitted in accordance with Eq. (2.20). The Gradient and ordinate intercept of the linear fittings plot were used to determine the dislocation density and dislocation outer cut-off radii

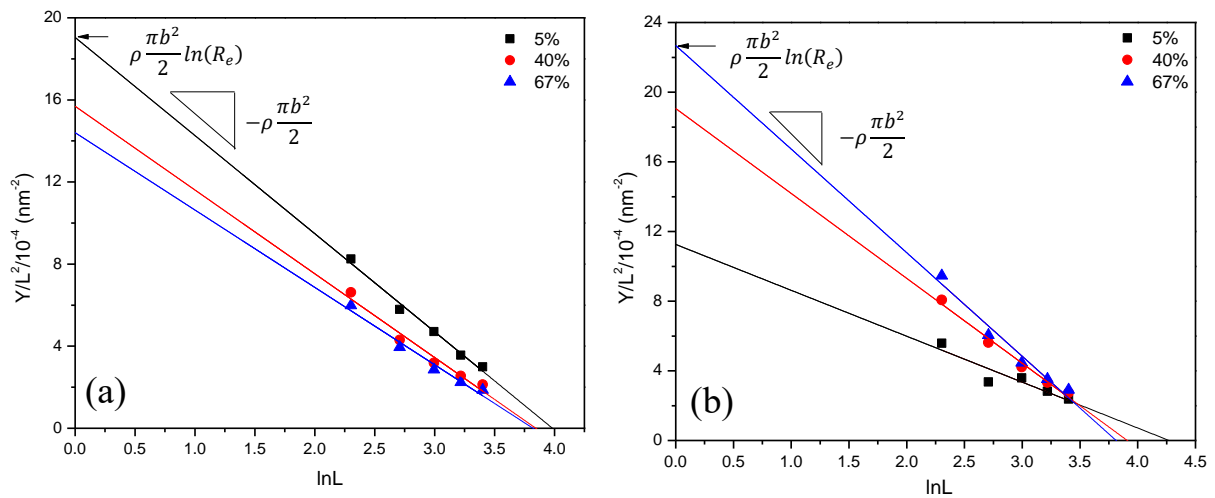


Fig. 5.6: Linear fitting to the variation of  $Y(L)/L^2$  with  $\ln(L)$  according to Eq. (2.20) for: (a) tensile (b) compressive sample.



of the deformed specimens shown in Figs. 5.6(a) and 5.6(b) for tensile and compressed sample respectively. The character of dislocations in the deformed specimen, represented by the parameter  $q$ , which are determined from the linear fits of Eq. (2.16) indicates whether the dislocation is edge or screw type or has a mixed character are shown in Table 5.1. Additionally, the variation of dislocation density, dislocation character ( $q$ ) and dislocation outer cut-off radius ( $R_e$ ) at various strains for both tensile and compressive specimens is also illustrated in Fig. 5.7 demonstrating the relationship of dislocation density and dislocation outer cut-off radius with its character.

It is seen from Table 5.1 that  $q$  value for the current steel deformed through tension was estimated to be:  $\sim 1.94$  at  $\sim 5\%$  of true strain indicating a mixed character of dislocation, which increased and reached  $\sim 2.16$  at fracture strain. A rising  $q$  value implicates that the population of the screw character of  $\left(\frac{a}{2}\right)\langle 110 \rangle$  dislocations is rising with imposed strain. On the other hand while focusing on the dislocation character of the steel deformed by compression, it is seen that estimated value for  $q$  parameter is  $\sim 2.12$  at  $\sim 5\%$  compression that remains almost constant until  $\sim 40\%$  strain, thereafter dropping to  $\sim 2$  at  $\sim 67\%$  of compressive strain. Therefore, an opposite trend was noticed in the case of compression; the population of screw characters of dislocation remained constant or decreased with compression. In the present dissertation,  $q$  values for pure edge and screw dislocation in the austenite microstructure are assumed to be 1.71 and 2.46, as adopted in the literature (Shintani & Murata, 2011). The decrease in screw type dislocation population under compressive loading contrasts with recent findings for austenitic and/or ferritic steels, wherein the values were seen to rise monotonically with increasing deformation (Mahato *et al.*, 2015; Simm *et al.*, 2016).

The apparent implication of the continuously rising  $q$  value in Table 5.1 and Fig. 5.7(a) is that the population of screw dislocations in the microstructure of tensile-deformed steel rises with increasing tensile strain. Dislocations can quickly alter their slip planes by cross-slipping in a microstructure with a high density of screw dislocations (Hull & Bacon, 2011). Thus, cross-slip would be preferred according to the governance of screw character of dislocations in tensile deformed steel, and a reduction in dislocation density should be anticipated owing to dynamic recovery occurring at high strains (Kim *et al.*, 2018). This type of circumstance is frequently seen in the microstructure of a high SFE alloy, and will be covered in more detail below.

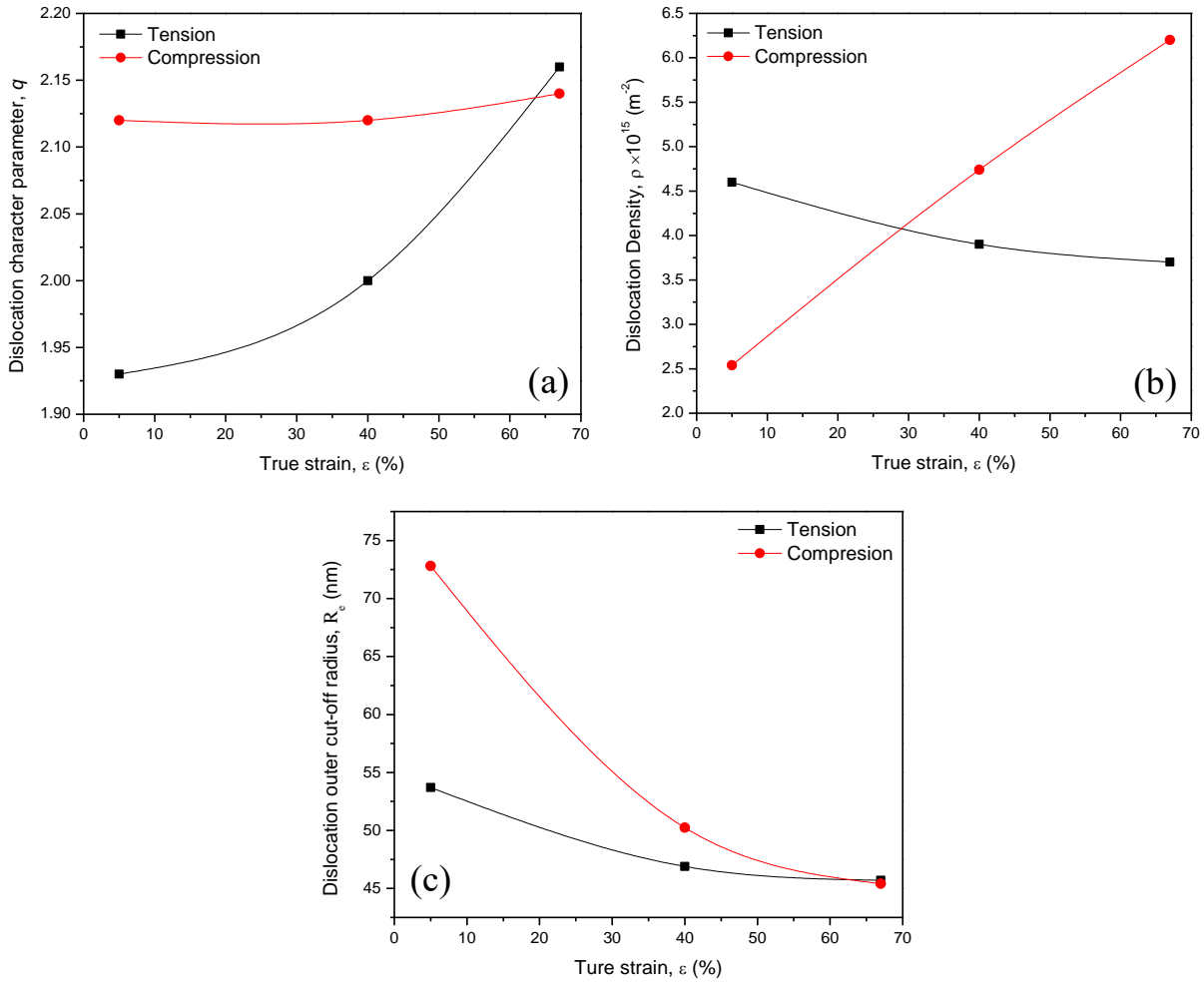


Fig. 5.7: Variation of (a) dislocation character parameter (b) dislocation density and (c) dislocation outer cut-off radius with true strain under tension and compression.

Measured values of dislocation densities for tensile-tested and compressive specimens at various interrupted strain were presented in Table 5.1, and their variation with true plastic strain was also subsequently viewed in Fig. 5.7(b). The figure shows that as a result of deformation, dislocation density drops when the sample is deformed under tension, but the reverse tendency is seen when the sample is deformed under compression. For instance the dislocation density value of tensile-deformed sample is ( $\sim 4.6 \times 10^{15} \text{ m}^{-2}$ ) at  $\sim 5\%$  strain, which decreases and reaches ( $\sim 3.3 \times 10^{15} \text{ m}^{-2}$ ) at failure strain, whereas the dislocation density in the sample deformed by compression is initially low ( $\sim 2.54 \times 10^{15} \text{ m}^{-2}$ ) at  $\sim 5\%$  strain, thereafter increasing rapidly up to  $\sim 40\%$  strain and attaining a highest value ( $\sim 6.2 \times 10^{15} \text{ m}^{-2}$ ) at  $\sim 67\%$  strain. Reduction in dislocation density in the case of tensile deformed sample is attributed to dynamic recovery of dislocation that occurs through cross-slip of screw character dislocations: as already discussed in the previous paragraph. In contrast,

no such cross-slip or dynamic recovery could be expected in compressed specimens due to the lower population of screw-type dislocations. As a result, dislocation storage capacity of the matrix is increased, resulting in a high dislocation density at high strains.

Estimated values of  $R_e$  of deformed specimens at each specified true strain are presented at Table 5.1 and also plotted in Fig. 5.7(c). As shown in Fig. 5.7(c),  $R_e$  value for tensile specimen at ~5% of true strain is ~54 nm which decreases moderately with strain and remains almost constant (remains between ~46-~47 nm for a variation of strain ~40% to ~67%). In compressive loading the corresponding  $R_e$  value is ~73 nm which is comparatively higher than that in the tensile specimens (~54 nm) at the initial stage of deformation. It also decreased further with straining and reached ~45 nm at ~67% of compression.  $R_e$  value at initial strain implicates a weaker interaction among the dislocation at deformed microstructure in compressive specimens at the beginning of plastic deformation compared to the tensile loading. According to Sahu *et al.* (2012),  $R_e$  values for steel microstructures typically steadily decline with increasing stresses, mostly because strongly correlated dislocation substructures such as tangles and cells start to develop at high strains. The variation of  $R_e$  in Fig. 5.7(c) suggests that the dislocation interaction in the deformed sample was initially weak, but that with the application of plastic strain, this interaction becomes stronger, leading to the formation of strongly correlated dislocation substructures like dislocation tangles and dislocation cells. The drop in  $R_e$  may also be explained by the assumption that the strain fields of the individual dislocations screen each other, and thereby, lowering the overall distortion in the lattice and a consequent reduction in the outer cut-off radius ( $R_e$ ). However, strong screening can also occur when the dislocations arrange into dipoles and/or low angle grain boundaries (Gubicza, 2014). Implementation of this postulate is discussed in the next section and also further examined through TEM studies.

Wilkens (1970) further claims that focusing just on the dislocation density would not provide an accurate understanding of the behaviour of dislocations in a microstructure comprising dislocation substructures. As a result, he introduced the dimensionless parameter ( $R_e\sqrt{\rho}$ ), also known as the Wilkens parameter, whose value is directly proportional to the correlation degree of dislocations. The dislocations are strongly associated if the Wilkens parameter is near to unity; otherwise, they can be thought of as being randomly distributed (Wilkens, 1970). Table 5.1 shows the computed value for the dislocation arrangement parameter  $M$  using the predicted  $\rho$  and  $R_e$  from XLPA, demonstrating a weak dipole interaction

in the initial stage of deformation ( $\sim 5\%$  of true strain) for both tensile tested and compressed specimens. However, as more plastic strain is exerted,  $M$  value declines, indicating that the dipole-forming dislocation interactions gets stronger. A closer look at the Wilkens parameter value in Table 5.1 revealed a strong correlation of dislocation at high strain in the case of tensile-tested specimen compared to compressed specimen, which is explained in the following in terms of dislocation density. It is well known that at high stresses, when newer dislocations are created in the microstructure, the dislocation densities would rise and the dipole feature will become more pronounced (Ungár & Ribarik, 2017) and they become more correlated. It is also known that strong correlation between dislocations aids in the formation of cell structure in high SFE materials. In the present case, strong dipole interaction in tensile specimens should be conducive to form strongly correlated dislocation substructures, i.e., dislocation cells and dislocation tangles where in the dislocation are annihilated with the opposite burgers vector, resulting in a decrease in dislocation density. In contrast, relatively weak dipole interaction in compressive specimens would prevent the formation of such dislocation substructures, leading to an increase in dislocation density.

#### 5.2.4 Evolution of fault density during tension and compression

In deformed microstructures stacking fault density could be estimated in a very significant way through XLPD by using two well-known approaches namely, Balogh *et al.* (2006) and Warren (1969). Both techniques incorporate specific characteristics of a diffraction profile, most notably peak shift, peak broadening, and peak asymmetry, which are significantly influenced by the planar fault of deformed materials. The Warren (1969) method is concerned with the

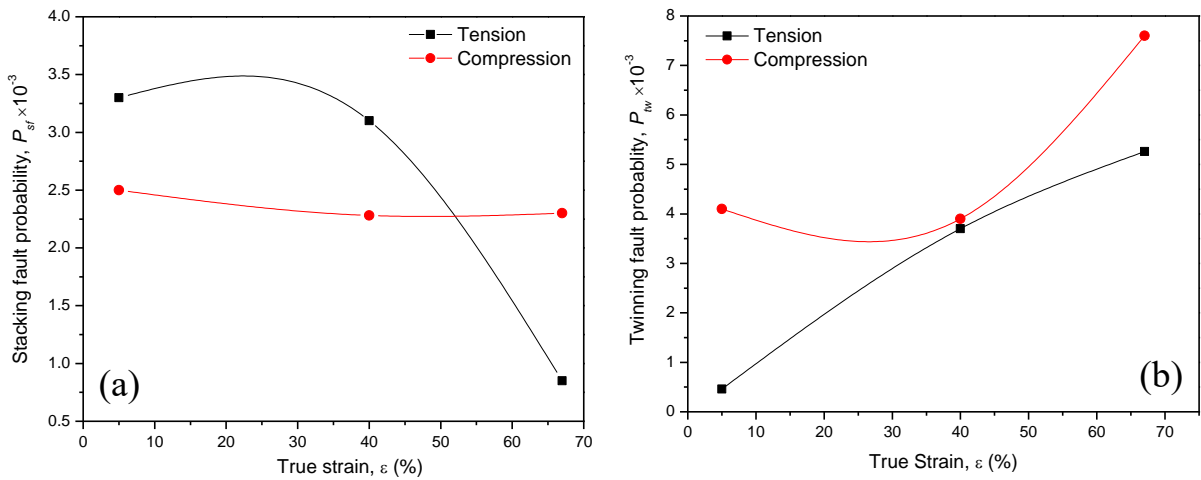


Fig. 5.8: Variation of (a) stacking fault probability (b) twinning fault probability with true strain under tension and compression.

appearance of asymmetry in a diffraction profile owing to the existence of deformation twins in the microstructure, whereas the peak shift is exclusively attributed to stacking faults. As a result, according to the Warren's prescribed technique, peak shift analysis and the peak asymmetry of (200) Bragg reflections were used to calculate the stacking fault probability,  $P_{sf}$ , which represents the fraction of slip planes affected by stacking faults, and the twin fault probability,  $P_{tw}$ , which represents the twin density with the austenite microstructure of the deformed specimen, respectively. For the investigated steels, the relevant peak shifts of the (111) and (200) Bragg reflections were calculated in relation to the respective peak locations of the annealed specimens. Estimated values of stacking fault probability ( $P_{sf}$ ) and twinning fault probability ( $P_{tw}$ ) for both tensile tested and compressed specimens at different stage of deformation was presented in Table 5.1 and also viewed graphically in Figs. 5.8(a) and 5.8(b) respectively. As seen in Fig. 5.8(a),  $P_{sf}$  in the deformed austenite for tensile tested steel was initially high ( $\sim 3.3 \times 10^{-3}$ ), remaining almost constant ( $\sim 3.1 \times 10^{-3}$ ) until intermediate strain ( $\sim 40\%$ ) representing no newer stacking faults were sufficiently formed at this stage. However, with further increment of strain, the stacking fault probability decreased and attained lowest value ( $\sim 0.85 \times 10^{-3}$ ) at failure strain. Such a finding in deformed high-Mn steel is unusual since stacking fault density is expected to increase at high strain, and those stacking faults can then overlap to produce a twin (Mahato *et al.*, 2015). However, in the present steel the newly created stacking faults at high tensile strain rearrange with the preexisting SFs to form a twin. However,  $P_{sf}$  in compressed specimen as shown in Fig. 5.8(a) does not vary significantly and remains almost constant signifying that freshly formed SFs at high strain are interpreted as twins created on successive (111) planes. Further, Fig. 5.8(b) revealed an increasing twinning fault probability with increasing both types of deformation, although the individual increasing pattern are not identical. Fig. 5.8(b) is largely represented by a lower value of  $P_{tw}$  under tension in comparison to the compressed microstructure at early stage of deformation implicating a lower abundance of twinning, i.e. a predominating dislocation plasticity. However, the  $P_{tw}$  values for tension and compression are nearly comparable at  $\sim 40\%$  strain.

### 5.2.5 Stacking fault energy analysis

The SFE of austenite was further calculated for its association with the deformation microstructure utilizing the different dislocation characteristics thus determined using Eq. (2.20) and reported in Table 5.1. The first model to predict the SFE in austenitic steels using

X-ray diffraction was developed by Schramm and Reed (1975), and it was later improved by Dey *et al.* (2005) after accounting for the effect of dislocation-stacking fault interactions (Schramm and Reed, 1975; Mahato *et al.*, 2015). Then, using the estimated values for the different dislocation-related characteristics in Table 5.1, the SFE ( $\gamma$ ) of the steels under consideration was calculated using the Eq. (2.26) (Dey *et al.*, 2005). The SFE values of the steels thus estimated using Eq. (2.26) are shown in Table 5.1. It is seen that the SFE for tensile tested specimen is  $\sim 43 \text{ mJm}^{-2}$  at  $\sim 5\%$  strain, which is somewhat higher than the usual SFE range recommended for the occurrence of twins or stacking faults; rather, a predominance of dislocation plasticity should be expected within this range of SFE (Allain *et al.*, 2004). Multiple slip systems could also be activated at this range of SFE, which could lead to the formation of various dislocation substructures like mutually intersecting dislocations, dislocation pinning, sessile Lomer-Cottrell (LC) lock formation, and Taylor lattice type dislocation substructure at low strain. An overview of these microstructures is presented in the following section. Das *et al.* (2021) found a similar type microstructure in their Fe-Mn-Al-C alloy during the early stage of deformation, with a corresponding SFE  $\sim 60 \text{ mJm}^{-2}$ . At high strain, SFE of this steel was raised to  $\sim 89 \text{ mJm}^{-2}$ , which favored the wavy glide over planar slip resulting in the formation of dislocation cell/wall in the deformation microstructure. In the present case, however, the SFE in case of compression didn't rise with straining; instead, it remained almost constant and was sufficiently lower than that of the tensile sample. At this strain twinning is seen in practically all of the grains and twinning bundles are now observed to develop. Deformation microstructures obtained from the XLPA are further investigated through the TEM & EBSD in the following.

### 5.3 TEM & EBSD investigations on deformation microstructures

The microstructures at different stages of deformation and their possible influence on the stress-strain plots of Fig. 5.2(a) were investigated using TEM and presented in Fig. 5.9. The bright field (BF) micrographs Figs. 5.9(a) and 5.9(b) represent the deformation microstructure of the tensile and compressed specimens, respectively at  $\sim 5\%$  of true strain, wherein, Fig. 5.9(a) depicts a microstructure containing a Taylor lattice like dislocation arrangement accompanied by sessile Lomer-Cottrell (LC) lock. A LC lock is formed by intersection of two perfect dislocations on two different set of  $\{111\}$  planes, while a presence of dislocation tangle in Fig. 5.9(a) appears to be a consequence of activation of dislocation plasticity in most of the grains. On the other hand, no such proliferation of dislocation plasticity could be noted for the

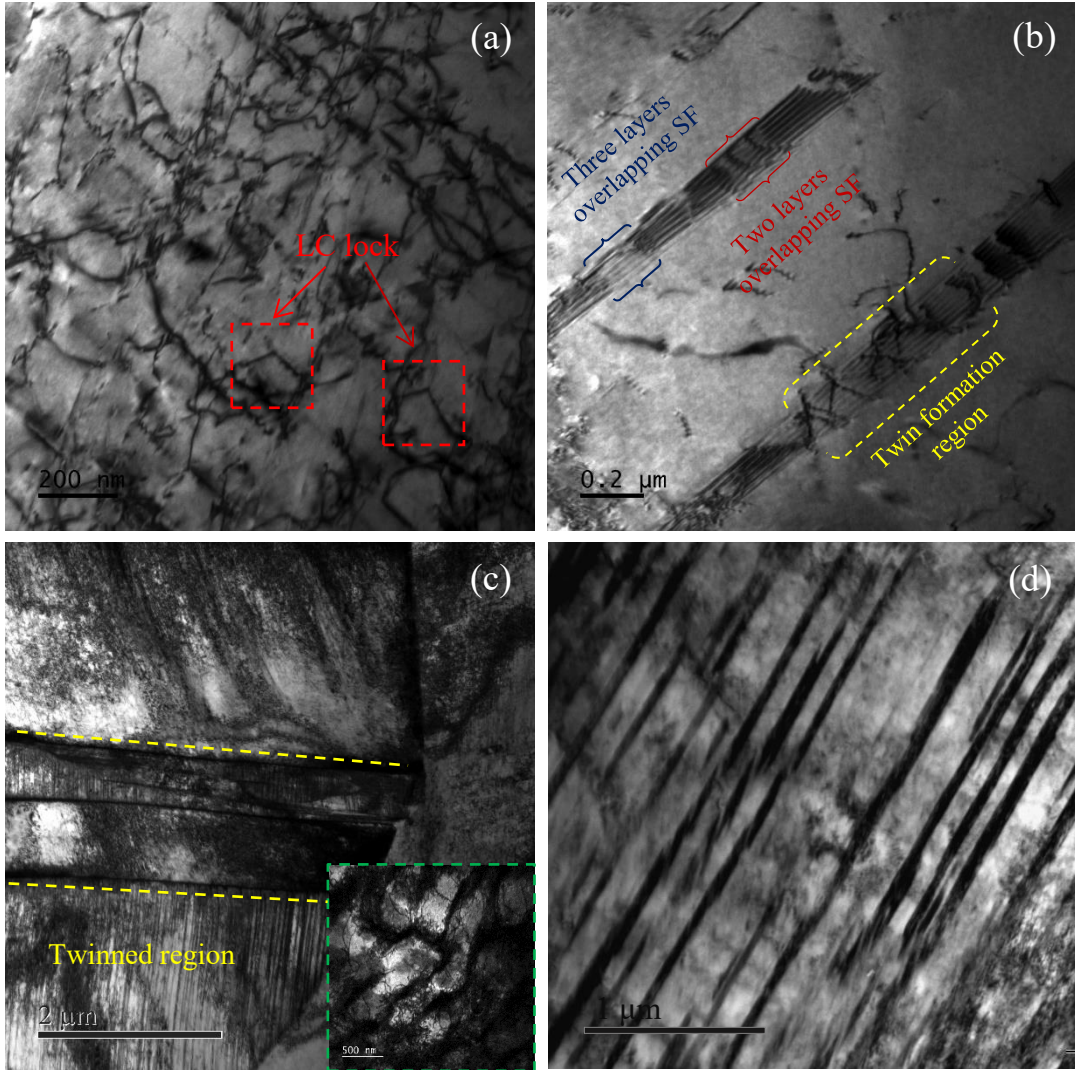


Fig. 5.9: BF TEM micrographs at: (a) ~5% tensile loading (b) ~5% compressive loading showing different overlapping of SFs (c) Tensile fracture strain (~ 67%) where dislocation wall/cell formation was shown in inset (d) twin bundle at ~67% compression.

compressed specimen, rather overlapping of stacking faults (SFs) were clearly observed in Fig. 5.9(b), which is known to be associated with the nucleation of deformation twins. The region of SF overlapping is delineated in Fig. 5.9(b) using different shades and the region of dark contrast is due to the overlap of SFs on two consecutive  $\{111\}$  planes, while the null contrast therein corresponds to SFs overlapping on three successive  $\{111\}$  planes (Carter & Williams, 2016).

It is clear from Fig. 5.9(a) that the early deformation under tension was dominated by dislocation slip and sessile LC locks and such locks provide an efficient obstacle for the dislocation glide (Yan & Lin, 2019) - resulting in higher yield strength (Fig. 5.2(a)), while for



compression the early strain accommodation primarily occurs through the nucleation of twinning. Similar yield asymmetry at ~2% strain was also reported by Tong *et al.* (2015) in extruded Mg-Zn-Ca alloy and they also observed the prevalence of dislocation slip in tension, while the deformation twins dominated the compression.

At higher strains, the tensile microstructures were controlled by deformation twinning and concomitant dislocation plasticity, while deformation twinning alone was the prevalent deformation mode in case of compression. This situation is exemplified in Figs. 5.9(c) and 5.9(d) corresponding to ~ 67% true strain, wherein, differently delineated grains reveal the simultaneous grain dependent deformation activity, and the inset shows a grain with dislocation cell and highly dense dislocation wall (Fig. 5.9(c)). In contrary, Fig. 5.9(d) reveals a prominent twin bundle in the compressed specimen deformed to similar strain (~67%) and this predominance of twinning is most likely contributing to the comparatively high strain hardening rate during compression than in tension (Fig. 5.2(b)).

Thus, the observed asymmetry in Fig. 5.2 results from different deformation mechanisms activating under tension and compression, namely, dislocation slip and low energy dislocation substructures like Taylor lattice are activated under tension, while formation of twinning at low strain was observed in compression, and dislocation slip was relatively less

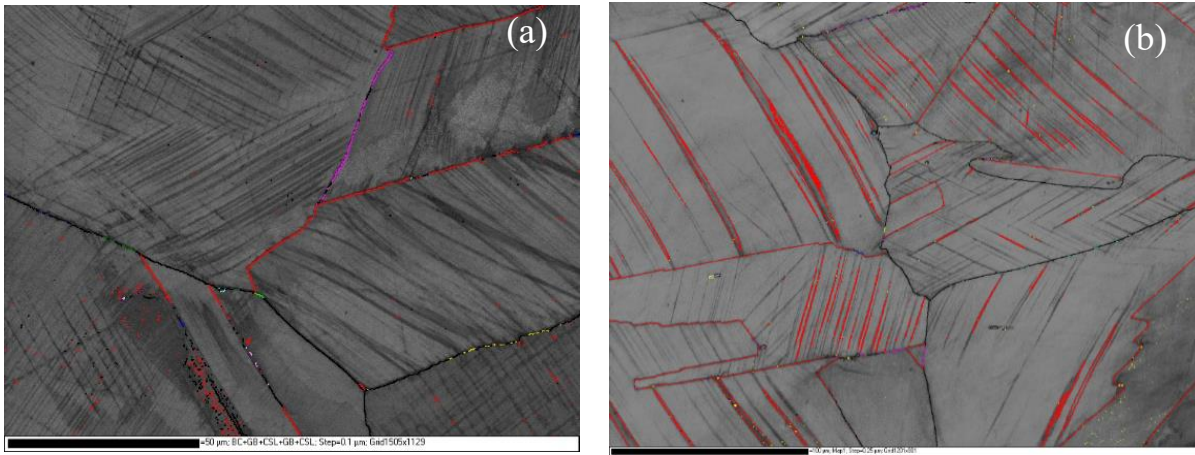


Fig. 5.10: EBSD map at ~40% true strain for (a) tensile tested sample (b) compressed sample.

pronounced in this deformation. This is also manifested through the EBSD microstructures presented in Fig. 5.10, corresponding to ~ 40% true strain, and it is readily seen that the propensities of twins represented by  $\Sigma 3$  boundaries (represented by the red lines) are



significantly lower in Fig. 5.10(a) - representing the tensile condition, as compared to Fig. 5.10(b) - representing the compressed condition.

## References

- Allain, S., Chateau J. P., Bouaziz, O., Migot, S. & Guelton N. (2004). *Mater.Sci. Eng. A*. **387-389**, 158-162.
- Balogh, L., Ribarik, G. & Ungar, T. (2006) *J. Appl. Phys.* **100**, 023512(1-10).
- Carter, B.C., Williams, D.B. Transmission electron microscopy: Diffraction, Imaging, and Spectrometry (Springer International Publishing Switzerland, 2016).
- Das, S.R., Shyamal, S., Shee, S.K., Kömi, J.I., Sahu P. (2021) *Mater. Charact.* **172** 110833
- De Cooman, B. C., Estrin, Y. & Kim, S. K., (2018) *Acta Mater.* **142**, 283-362.
- Dey, S. N., Chatterjee, P. & Sen Gupta, S. P. (2005). *Acta. Mater.* **53**, 4635-4642.
- Grässel, O., Krüger L., Frommeyer, G., Meyer, L.W. (2000) *Int. J. Plast.* **16**, 1391-1409.
- Gubicza, J., X-Ray Line Profile Analysis in Materials Science, IGI Global, Hershey, 2014.
- Hull, D., Bacon, D. J. (2011) Introduction to Dislocations, Fifth Edition, Butterworth-Heinemann, Oxford.
- Jin, J. E., Lee, Y.-K., (2009) *Mater. Sci. Eng. A*, **527**, 157–161.
- Jin, J. E., Lee, Y.-K., (2012) *Acta Mater.* **60**, 1680-1688.
- Kim, J.K., Estrin, Y., De Cooman, B.C. (2018) *Metal. Mater. Trans. A* **49**, 5919-5924.
- Mahato, B., Shee, S.K., Sahu, T., Ghosh Chowdhury, S., Sahu, P., Porter, D.A. & Karjalainen, L.P. (2015) *Acta Mater.* **86**, 69-79.
- Riaz, T., Das, S.R., Sahu, T., Chakraborti, P.C., Sahu, P., (2021) *Mater. Lett.* **282** 128691.
- Sahu, P., Shee, S.K., Hamada, A.S., Rovatti, L., Sahu, T., Mahato, B., Ghosh Chowdhury, S., Porter, D.A., Karjalainen, L.P. (2012) *Acta Mater.* **60**, 6907-6919.
- Schramm, R.E. & Reed, R.P. (1975). *Metall. Trans. A*. **6**, 1345-1351.
- Shintani, T., Murata, Y. (2011) *Acta Mater.* **59**, 4314-4322.
- Sidor, J.J., Chakravarty, P., Bátorfi, J.G., Nagy, P., Xie, Q., Gubicza, (2021) *J. Metals* **11(10)** 1571.
- Simm, T.H., Withers, P.J., Quinta da Fonseca, J. (2016) *Mater. Design* **111**, 331-343.
- Swift, H. W. (1952) *J Mech Phys Sol*, 1:1.

- Tong, L.B., Zheng, M.Y., Kamado, S., Zhang, D.P., Meng, J., Cheng, L.R., Zhang, H.J. (2015) *J. Magnes. Alloy.* **3**, 302-308.
- Ungár, T., Ribarik, G. (2017) *IOP Conf. Ser. Mater. Sci. Eng.* **194**, 1-8.
- Ungár, T., Ott, S., Sanders, P. G., Borbely, A., Weertman, J R. (1998) *Acta Mater.* **46**, 3693-3699.
- Warren, B. E. (1969). *X-ray diffraction*, Addison-Wesley, Reading, Mass.
- Yan, Z., Lin, Y. (2019) *Mater. Sci. Eng. A* **747**, 177-184.

# *Chapter 6*

## *Summary and Conclusions*



## 6.1 General conclusion

In this thesis the deformation microstructure and the corresponding hardening behavior of some coarse-grain high-Mn steels were studied using XRD and TEM. The quasi-static tensile deformation of Fe-25Mn-2Al-0.1C and Fe-25Mn-xAl-0.1C-0.4Si ( $x=0, 1, 3$ ) (all in wt.%) steels were carried out until failure with a strain rate of  $10^{-4} \text{ s}^{-1}$ , while both tensile and compressive test were performed to study the deformation behavior of Fe-30Mn-3Si-3Al steel. XRD data acquisition of the differently strained specimens is carried out to determine the structural and microstructural information. EBSD observations were performed using a high-resolution field emission scanning electron microscope, while TEM investigations were carried out to observe the deformation microstructure and identify the active deformation mechanisms. Based on the results the following conclusions can be drawn:

- In 2Al steel, three stages of strain hardening are seen, with substantial slip activities at the onset of deformation promoting Taylor lattice and stair-rod dislocations and the coexistence of dislocation cells and fine twin bundles in the microstructure at failure strain. Due to the cross-slip-induced recovery of dislocations, the strain hardening gradually reduced with increasing strain.
- Despite the fact that strain hardening was a synergistic effect of deformation twins and dislocation substructure, the contribution of dislocations in 2Al steel seems to overwhelm the contribution of twinning.
- Al alloying increased the yield strength of the steels, wherein, low yield strength  $\sim 232$  MPa was observed for 0Al steel which increased to  $\sim 516$  MPa for 3Al steel. Strain hardening rate was seen to decreased with Al concentration and early failure occurs in 0Al steel due to its comparatively higher strain hardening rate ( $\sim 3$  GPa), while the 1Al steel revealed the best strength-ductility combination with maximum elongation  $\sim 54\%$  at maximum ultimate tensile strength  $\sim 1.47$  GPa.
- Dislocation densities of  $\sim 10^{15} \text{ m}^{-2}$  were observed for the studied tensile strained steels. However, their magnitudes and the correlation among the dislocations existing in the microstructures gradually decreased with the increasing the Al content that could be attributed to the enhanced prevalence of dynamic recovery in the instance of increasing stacking fault energy due to increased Al alloying.
- The steels revealed a stacking fault probability of  $\sim 10^{-3}$ . The highest stacking fault probability value was observed for 0Al steel and it decreased linearly with the Al

addition. Likewise, the effective stacking fault energy of the studied steels also increased with Al content, the increment being  $\sim 7.85 \text{ mJm}^{-2} / \text{wt.}\% \text{ Al}$ .

- The deformation mechanisms and strain hardening rate were strongly influenced by the Al alloying. Deformation induced  $\varepsilon$ -martensite was only found in the strained microstructure of 0Al steel. However, deformation twinning and dislocation substructures without twinning were prevalent for 1Al and 3Al steels, respectively.  $\varepsilon$ -martensite formation in 0Al steel is greatly influenced by the lower value of SFE  $\sim 18.1 \text{ mJ/m}^2$  and larger grain size ( $\sim 41 \mu\text{m}$ ) and the austenite in such circumstances is subjected to extra shear stress and thereby leading to a higher observed strain hardening.
- The incidence of  $\varepsilon$ -martensite and/or twinning were found to be directly related to the equilibrium width of the overlapping stacking faults. The stacking fault energy based critical shear stress of twinning approach is a better alternative to predict the deformation behavior of high-Mn steels than that based on the former approach alone.
- A complete asymmetry in the mechanical behavior of 3Si-3Al steel is exhibited under tensile and compressive loading. A clear yield point with yield strength  $\sim 210 \text{ MPa}$  is detected under tension, whereas no visible yield point but rather a continuous curve is observed under compression. Despite the presence of significant asymmetry both the tensile and compressive steels follow a nearly symmetric path in their strain hardening behavior.
- Dislocation density is seen to drop when the sample is deformed under tension, but the reverse tendency is seen when the sample is deformed under compression, which is attributed to the dynamic recovery of dislocation in tension arising from the cross-slip of screw-type dislocations, whereas no such cross-slip or dynamic recovery is seen in compressed specimens due to the lower population of screw-type dislocations resulting in high dislocation density at high strain.
- The deformation mechanism in a compressed sample was seen to be fully controlled by the deformation twinning; though twinning was seen in the microstructure of a tensile deformed sample at higher strain, dislocation slip is the dominant factor here. Due to formation of sessile LC locks and dislocation tangles, the tensile flow curve initially leads the compression curve, but with the initiation of twinning in the compressed specimen, the result is reversed, and the compressive flow curve as well as the hardening curve exceed the tensile-deformed one.

## **6.2 Scope for future work**

In continuation of the present studies on the deformation behavior of various high-Mn steels with & without Al alloying, it is imperative that the following aspects should be planned as future activity.

1. The role of Si on the deformation microstructures of high-Mn steel requires further investigation in detail.
2. To investigate the tension/compression asymmetry of Fe-30Mn-3Si-3Al steel on the basis of crystallographic texture analysis.





## Publications

### Journal Publications

Materials Letters 282 (2021) 128691



Contents lists available at ScienceDirect

Materials Letters

journal homepage: [www.elsevier.com/locate/mlblue](http://www.elsevier.com/locate/mlblue)



#### Dislocation substructures in tensile deformed Fe–Mn–Al–C steel

T. Riaz<sup>a</sup>, S.R. Das<sup>a</sup>, T. Sahu<sup>b</sup>, P.C. Chakraborti<sup>c</sup>, P. Sahu<sup>a,\*</sup>

<sup>a</sup> Department of Physics, Jadavpur University, Kolkata 700 032, India

<sup>b</sup> Department of Physics, S.A. Jaipuria College, Kolkata 700 005, India

<sup>c</sup> Department of Metallurgical and Material Engineering, Jadavpur University, Kolkata 700 032, India



Materials Characterization 196 (2023) 112567



Contents lists available at ScienceDirect

Materials Characterization

journal homepage: [www.elsevier.com/locate/matchar](http://www.elsevier.com/locate/matchar)



#### X-ray line profile analysis on the deformation microstructure of Al-bearing high-Mn steels

T. Riaz<sup>a</sup>, S. Shyamal<sup>a</sup>, S.K. Shee<sup>b</sup>, L.P. Karjalainen<sup>c</sup>, P. Sahu<sup>a,\*</sup>

<sup>a</sup> Department of Physics, Jadavpur University, Kolkata 700 032, India


<sup>b</sup> Department of Physics, Midnapore College, Midnapore 721 101, West Bengal, India

<sup>c</sup> Centre for Advanced Steels Research, University of Oulu, FIN-90014, Finland



TECHNICAL ARTICLE

# Influence of Al Variation on the Mechanical Properties and Critical Shear Stress of Twinning in Fe-Mn-Al-C Steels

T. Riaz, S.R. Das, and P. Sahu 

Submitted: 3 April 2022 / Revised: 10 May 2022 / Accepted: 27 July 2022 / Published online: 29 August 2022

Materials Letters 300 (2021) 130216



Contents lists available at [ScienceDirect](https://www.sciencedirect.com)

Materials Letters

journal homepage: [www.elsevier.com/locate/matlet](http://www.elsevier.com/locate/matlet)



A quantitative assessment on the contribution of various dislocation substructures to flow stress in a fine-grain high-Mn steel

S.R. Das <sup>a</sup>, T. Riaz <sup>a</sup>, S. Shyamal <sup>a</sup>, P.C. Chakraborti <sup>b</sup>, P. Sahu <sup>a,\*</sup>

<sup>a</sup> Department of Physics, Jadavpur University, Kolkata 700 032, India

<sup>b</sup> Department of Metallurgical and Material Engineering, Jadavpur University, Kolkata 700 032, India